



**UNIVERSITEIT VAN PRETORIA
UNIVERSITY OF PRETORIA
YUNIBESITHI YA PRETORIA**

Denkleiers • Leading Minds • Dikgopolo tša Dihlalefi

**THE RELATIONSHIP OF WELD METAL HARDNESS, RESIDUAL STRESS AND
SUSCEPTIBILITY TO STRESS-CORROSION CRACKING IN A HYDROGEN
SULPHIDE ENVIRONMENT IN A 516 GR 70 CARBON STEEL SHIELDED
METAL-ARC WELDED JOINTS**

by

Deon Johan De Beer

Submitted in partial fulfilment of the requirements for the degree
Master of Engineering (Metallurgical Engineering)

In the

Department of Materials Science and Metallurgical Engineering

Faculty of Engineering, Built Environment and Information Technology

UNIVERSITY OF PRETORIA

September 2017

Supervisor: Prof. P.G.H. Pistorius

ABSTRACT

In the petrochemical industry, carbon steels exposed to H₂S environments may be susceptible to stress-corrosion cracking. A tensile residual stress and high hardness increases the risk of cracking in H₂S environments. NACE SP 0472 limits weld metal hardness to 210 HV₁₀ (200 HB) and heat-affected zone hardness to 250 HV₁₀ to prevent stress-corrosion cracking of carbon steel welds in H₂S. The hardness is controlled by the weld thermal cycle or by a post-weld heat treatment. In this project, the effect of hardness on the susceptibility to stress-corrosion cracking was investigated by increasing electrode strength systematically and measuring residual stress in the weld metal in the as-welded state. Samples were manufactured from SA 516 Gr 70, a carbon steel used extensively in the petrochemical industry. Heavily clamped plates were welded to minimise distortion and to maximise residual stress. The weld metal hardness was increased by using E6013, E7018-1, E8018-B2 and E9018-B3 electrodes without a post-weld heat treatment. Mechanical tests included all-weld and transverse tensile tests, impact strength and hardness testing. As the nominal strength of the weld metal increased, the all-weld tensile strength increased from 512 to 829 MPa, while the yield strength increased from 443 to 659 MPa. The average weld metal hardness increased from 177 to 317 HV₁₀. The transverse tensile strength was between 511-517 MPa, while the yield strength (in the transverse direction) was between 360 and 382 MPa. Residual stresses of the welded joint were measured by neutron diffraction in the through-thickness, longitudinal and transverse direction. The Von Mises theorem evaluated the principle residual stress. Results indicate that the residual stress in the weld metal may be up to 99% of the yield strength. For stress-corrosion cracking, the samples were submerged in the standard TM0177-2005 test solution for 30 days. The only sample to crack was the E9018, with an average weld metal hardness of 317 HV₁₀. The study results were consistent with the NACE SP0472 specification and earlier publications.

Keywords: Stress-corrosion cracking (SCC), Residual stress, Von Mises theorem, Mechanical properties, H₂S

ACKNOWLEDGEMENTS

I would like to thank the following people for what they have contributed to this dissertation. Without them, it would have been impossible:

Prof. M. du Toit (co-supervisor): Thank you for your guidance, development of this dissertation and all the opportunities you created for learning. I greatly appreciate it.

Prof. P.G.H. Pistorius (supervisor): Thank you for all the guidance, time and advice for this dissertation.

Nuclear Energy Corporation of Southern Africa (NECSA): I would like to acknowledge and thank Dr Andrew Venter and his team for their contribution to this project. They dedicated an immense quantity of time and research to this project. Their contribution included the measurement and calculation of residual stress.

Macsteel VRN: Macsteel VRN provided 250 kg (sample plates) of SA 516 Gr 70 pressure vessel steel.

Yellotec: I would like to thank Tjaart Broodryk and his team at Yellotec who lent me a thermal camera and provided me training in the software.

Afrox: I would like to thank Afrox for their support on the project. All the filler metal used for the weld metal was supplied by them.

SAIW (Southern African Institute of Welding): I would like to thank Sean Blake, Dennis, Frans and Willie at the SAIW. They arranged for the welding of all the sample plates.

MINTEK: I would like to thank Melanie Smith and Jaco Jonck for their contribution to the corrosion work.

Deon Slabbert (Sasol Synfuels) - I would like to thank him for all his guidance in the corrosion work and connecting with Mintek.

ESKOM: I would like to thank Jacques Calitz with his team for his advice in the field of mechanical testing.

TABLE OF ABBREVIATIONS

The following is a list of definitions, acronyms and abbreviations used.

AC: aligned second phase

Ac1: The temperature at which austenite forms on heating

Ac3: In hypo-eutectoid steel, the temperature at which transformation of ferrite into austenite is completed upon heating

AF: Acicular ferrite

BCC: body-centred cubic

BF: Blocky ferrite

BM: Base metal (welded material)

CE: Carbon equivalent

CLR: Crack Length Ratio

CSR: Crack Sensitivity Ratio

CTR: Crack Thickness Ratio

DHD: Deep hole-drilling

FCAW: Flux Cored Arc Welding

FCC: face-centred cubic

FEA: Finite-Element Analysis. A numerical technique for solving boundary value problems

FEM: Finite-Element Modelling

FL: fusion line

GF: Grain boundary ferrite

GMAW: Gas Metal-Arc Welding

GTAW: Gas Tungsten Arc Welding

HAZ: Heat-affected zone (the BM adjacent to the WM).

HD: hydrogen content

HI: heat input, usually measured in kJ/mm

HIC: hydrogen-induced cracking.

MAC: Martensite, austenite and carbides

MMA: Manual Metal-Arc

NACE: National Association of Corrosion Engineers (USA)

ND: Neutron diffraction

NDT: Non-destructive testing

P-1: material: carbon steel material according to ASME IX

PQR: Procedure Qualification Record. Documents the various parameters for a weld, including the test(s) performed to approve the welding procedure.

PWHT: post-weld heat treatment

SAIW: Southern African Institute of Welding

SAW: Submerged Arc Weld

SCC: Stress-corrosion cracking. A phenomenon that occurs in the presence of a stress in a corrosive environment. It results in failure or cracking well below the design stress of the welded metal

SEM: Scanning Electron Microscopy

SMAW: Shielded Metal-Arc Welding

SSRT: Slow-strain-rate testing

TS: tensile strength

WF: Widmanstätten ferrite

WM: The weld metal used to join the BM

WPS: Welding Procedure Specification. The procedure that guides the manufacturing of welds

XRD: X-ray diffraction

YS: Yield strength

TABLE OF CONTENTS

ABSTRACT	i
ACKNOWLEDGEMENTS	ii
TABLE OF ABBREVIATIONS	iv
TABLE OF CONTENTS	vi
LIST OF FIGURES.....	xi
LIST OF TABLES	xviii
1 INTRODUCTION	1
1.1 Project background	1
1.2 Welding process used.....	2
1.3 Outline of this study.....	2
1.4 Research aims	2
1.5 Research assumptions and limitations.....	3
2 LITERATURE REVIEW	4
2.1 Introduction	4
2.2 Welding metallurgy.....	4
2.2.1 Base metal used in the study.....	4
2.2.2 Microstructure of the base metal	4
2.2.3 Mechanical properties of the base metal	6
2.2.4 The effect of the weld thermal cycle on the formation of microstructures in the weld metal and metallurgical zones in weld.....	7
2.2.5 The effect of heat input on hardness and width of weld.....	10
2.2.6 Calculation of the minimum preheat temperature to avoid hydrogen cracking 12	
2.2.7 The effect of post-weld heat treatment effect on the hardness	15
2.2.8 Conclusions from the literature on the effect of hardness on the weld metal and heat-affected zone	17
2.3 Residual stresses.....	18
2.3.1 Residual stress measurement techniques	19

2.3.2	Detailed discussion of the neutron diffraction measurement technique	22
2.3.3	The influence of heat input and preheat temperature on residual stress	24
2.3.4	Earlier work on the effect of post-weld heat treatment on residual stress	27
2.4	The use of the Von Mises criterion to evaluate residual stress	31
2.4.1	Introduction	31
2.4.2	Maximum distortion energy theory (Von Mises theorem)	32
2.4.3	Relationship between residual stress and Von Mises theorem	33
2.4.4	Summary of conclusions from studies on residual stress in welds	33
2.5	Stress-corrosion cracking and Hydrogen-Induced Cracking	34
2.5.1	Introduction	34
2.5.2	Corrosive environment for test work according to NACE TM1077-2005	35
2.5.3	Hardness limits to prevent cracking in H ₂ S	35
2.6	Test designs and aims	38
2.6.1	Tensile testing	38
2.6.2	Impact toughness	39
2.6.3	Hardness testing	39
2.6.4	Selection of a corrosion test for this study	40
2.6.5	Evaluation of cracks in the base metal and weld metal	42
3	EXPERIMENTAL EQUIPMENT AND METHODS	44
3.1	Sample planning	44
3.2	Welding electrodes used in this study	44
3.3	Equipment and measuring techniques	46
3.4	Sample manufacturing and weld setup	48
3.4.1	Preparation for welding	48
3.4.2	Fixing of clamps	48
3.4.3	Welding power supply	49
3.4.4	Run-on and off tabs	49

3.4.5	Heat input	50
3.4.6	Post-weld heat treatment.....	56
3.5	Characterisation of welded joints	57
3.5.1	Tensile testing	57
3.5.2	Impact testing	58
3.5.3	Hardness testing.....	58
3.5.4	Metallography	59
3.5.5	d-zero and neutron diffraction measurements	59
3.5.6	Testing for stress-corrosion cracking	61
4	RESULTS	64
4.1	Tensile testing	64
4.2	Impact testing.....	65
4.3	Hardness testing	66
4.4	Residual stress.....	72
4.5	Microstructures.....	80
4.6	Stress-corrosion cracking test.....	88
4.6.1	Evaluation of base metal cracking observed in samples	88
4.6.2	Weld metal cracking observed in the E9018 sample	92
5	DISCUSSION	96
5.1	Tensile testing	96
5.1.1	Transverse tensile strength	96
5.1.2	All-weld tensile strength.....	97
5.1.3	Summary of observations on tensile test results	98
5.2	Impact testing.....	98
5.2.1	Weld metal toughness	98
5.2.2	Heat-affected zone toughness	99
5.2.3	The effect of post-weld heat treatment on the impact strength of the E7018-1 welded joint.....	99

5.3	Hardness of the heat-affected zone and weld metal	100
5.3.1	Weld metal hardness in the E6013, E7018, E8018 and E9018 electrodes 100	
5.3.2	Heat-affected zone hardness of the E6013, E7018, E8018 and E9018101	
5.3.3	Comparison of the E7018 and E7018-PWHT weld metal and heat-affected zone's hardness.....	102
5.3.4	Summary of hardness observations	103
5.3.5	Tensile strength and hardness	104
5.3.6	The relationship between toughness and hardness	106
5.4	Residual stress.....	108
5.4.1	Summary of observations on the residual stress	109
5.4.2	Von Mises Stress in weld metal.....	110
5.4.3	Effect of a post-weld heat treatment on weld residual stress.....	114
5.4.4	Calculation of the minimum expected residual stress in the weld metal as a function of the preheat temperature.....	115
5.4.5	Summary on the interpretation of residual stress measurements.....	118
5.5	Metallography.....	119
5.6	Susceptibility to cracking.....	119
5.6.1	Base metal cracking	119
5.6.2	Weld metal cracking	120
6	CONCLUSIONS	122
6.1	Tensile test.....	122
6.2	Impact testing.....	122
6.3	Hardness of weld metal and heat-affected zone	122
6.4	Residual stresses.....	123
6.5	Stress-corrosion cracking.....	123
6.6	Summary.....	124
7	LIMITATIONS AND SHORTCOMINGS.....	125

7.1	Samples	125
7.2	Process	125
7.3	Heat input.....	125
7.4	Residual stress.....	126
7.5	Stress-corrosion cracking.....	126
8	PROPOSED FUTURE WORK.....	127
	REFERENCES.....	128
	Appendix A.....	134
	Appendix B.....	135
	Appendix C.....	136

LIST OF FIGURES

Figure 1: Iron carbon phase diagram [10]. The black line represents the carbon content of SA 516 Gr 70	5
Figure 2: The as-rolled microstructure of the BM (SA 516 Gr 70), comprising ferrite (light bands) and pearlite islands (dark bands), magnified 500x	6
Figure 3: Influence of carbon on mechanical properties. The carbon content of the low-carbon steel in this dissertation is indicated by the red line [11].....	7
Figure 4: The result of the thermal cycle can be seen, where various zones exist, such as the HAZ and BM. The recrystallisation is caused by a high temperature during welding in the HAZ. Adapted and edited from [12].....	8
Figure 5: A typical continues cooling transformation diagram describing the austenite transformation in WM upon cooling [16].....	9
Figure 6: Hardness profiles for HIs of 0.8, 1.2 and 1.6 in kJ/mm. A higher HI results in a lower hardness in the WM (between 0 and 2 mm from the weld centreline) [19]	11
Figure 7: The predicted maximum heat-affected zone hardness (HV_{10}) for carbon steels as a function of calculated cooling time Δt_{8-5} . As the cooling time is increased, there is a reduction in hardness [20], [21].....	12
Figure 8: An example of the calculated CE value and the scale selected. The calculated CE value of 0.36 was the closest to 0.38 when using a rutile or cellulose electrode only, applying scale A.....	13
Figure 9: The hydrogen scale and equivalent were applied. For the specific HI and thickness, a preheat temperature of 75°C was selected [24]	14
Figure 10: Expected residual stresses in three directions: Longitudinal (σ_x), transverse (σ_y) and normal components (σ_z) [32]	19
Figure 11: General residual stress patterns expected over the welded plates, a) the longitudinal stress σ_x , and b) the transverse stress σ_y [31].....	19
Figure 12: Different measuring techniques for residual stress [33]	20
Figure 13: Comparison of the two techniques: XRD (A) and ND (B). The penetration is significantly higher for ND [38]	22

Figure 14: Waves diffracted off a crystalline surface. As the spacing increases, the diffraction angle will decrease(θ). The dark line is the $d^0_{(hkl)}$ value and the shift in peaks is used in calculating the change in elastic strain [38].....	23
Figure 15: Schematic representation of the calculated effect of various HIs on the size and area of residual stress in the longitudinal direction. It can be observed that a lower HI results in a smaller stress area [41].....	24
Figure 16: Calculated residual stress at a) the inner surface that is in tensile while at b), the outer surface is in compression. A preheating temperature of 50°C and 200°C was used in the calculation of the residual stress [45].....	26
Figure 17: The calculated effect of varying PWHT time and temperature on the residual stress for P-91 creep resistant steel [49].....	28
Figure 18: The result of various PWHTs on residual stresses. As the PWHT temperature was increased, the tensile residual stress decreased [50]	29
Figure 19: The in situ residual stress measurement of the WM for the hoop, axial and radial stress. The measurement was performed in the WM at approximately 2.5 mm from the outer surface [51]	30
Figure 20: The residual Von Mises Stress calculated for the hoop, axial and radial component as the PWHT was applied. It was compared with the yield strength of pipes and plates [51].....	31
Figure 21: Representation of factors influencing SCC.....	34
Figure 22: Illustration of a stress vs strain diagram. Various properties obtained from the tensile test can be established as well: tensile strength and yield strength [61]	38
Figure 23: Crack lengths in specimens and measurement values [67]	42
Figure 24: The setup of thermal couples along the thermal camera at measuring points SP01 and SP02. SP01 was close to the B-Type thermal couple, while SP02 was close to the K-type thermal couple. The clean ground areas emissivity was 0.55 and the oxidised part was 0.85.....	47
Figure 25: The left-hand side with four clamps and the right-hand side with two clamps and tack welds. The dark lines indicate where the plate was tack welded to a 32 mm thick base plate.....	49

Figure 26: The regions where arc-blow occurred during welding. The problem was solved by adding run-on and off plates. The arc-blow compromised the integrity of the first and last 50 mm on each of the welds.....	50
Figure 27: The run-on and off plate with dimension 60x16x40 mm.....	50
Figure 28: Single-V prep with weld sequence used for the manufacturing of the welds	51
Figure 29: The E6013 HI A vs HI B in kJ/mm for each weld deposit	52
Figure 30: The E7018 HI A vs HI B in kJ/mm for each weld deposit	53
Figure 31: The E8018 HI A vs HI B in kJ/mm for each weld deposit	54
Figure 32: HI[A] vs HI[B] in kJ/mm for each weld deposit; it deviated from the ideal line	55
Figure 33: The HI, as calculated using Method A and Method B in kJ/mm for each weld deposit on series E6013, E7018, E8018 and E9018 with the error of each data series	55
Figure 34: The plate with the edge trimmed. The sample was cut before the PWHT was performed. The final dimensions was 300x290x16 mm	57
Figure 35: Tensile specimen dimensions used in test [72].....	57
Figure 36: Orientation of Charpy impact strength specimen machined from each sample plate. The vertical line denotes the notch	58
Figure 37: Indentations at the top, middle and bottom of the weld. The transverse indent spacing was 0.5 mm.....	59
Figure 38: The d-zero reference slices, with dimensions 100x3x16 mm was taken at the end of the plate where the residual stress was negligible. This was for each sample series to calculate an accurate d-zero value.....	60
Figure 39: The residual strain measurements at various depths of 2.1, 5.2, 8.31, 11.45 and 14.52 mm. The dimensions of the gauge volume are 3x3x3 mm	61
Figure 40: The sample plates were submerged in NACE TM 0177 solution with no cutting to the plates.....	62
Figure 41: A cross section AA that indicates where the sectioning was made of the samples in the middle of the plate after it was exposed to the test solution. The largest	

stress is in the middle of the sample on AA; this is the specimen inspected. The dimensions of the sample are 16x100x20 mm	63
Figure 42: Transverse hardness was HV ₁₀ of the E6013 welded sample of the WM, HAZ and BM. It is represented for the top, middle and bottom of the weld	67
Figure 43: Transverse hardness was HV ₁₀ of the E7018 welded sample of the WM, HAZ and BM.....	67
Figure 44: Transverse hardness was HV ₁₀ of the E8018 welded sample of the WM, HAZ and BM.....	68
Figure 45: Transverse hardness was HV ₁₀ of E9018 welded sample of the WM, HAZ and BM.....	68
Figure 46: Sample comparison of the top hardness HV ₁₀ for the various test samples. There is high hardness in the HAZ of the E6013 electrode. This exceeds the limit of 250 HV ₁₀ in the HAZ. In the WM, a constant hardness increase can be observed	69
Figure 47: Sample comparison of middle hardness HV ₁₀ . The increase in hardness can be illustrated for each welding electrode	69
Figure 48: Sample comparison of the bottom hardness HV ₁₀ . The increase in hardness is indicated for each welding electrode	70
Figure 49: The top hardness HV ₁₀ in the weld sample E7018 before the PWHT. This is compared with the E7018-PWHT after a heat treatment at 600°C for two hours	70
Figure 50: Centre hardness HV ₁₀ comparison of the E7018 and E7018-PWHT in the BM, HAZ and WM. The PWHT was at 600°C for two hours. A slight decrease in hardness can be observed	71
Figure 51: The bottom hardness comparison in HV ₁₀ for the E7018 and E7018-PWHT sample in the BM, HAZ and WM. The greatest hardness reduction occurs in the HAZ.....	71
Figure 52: The normal, longitudinal and transverse stress distribution for the E7018 electrode without a PWHT. The stress levels are measured at separate depths in the welded samples	74
Figure 53: The normal, longitudinal and transverse distribution for the E7018-PWHT. The stress levels is measured at separate depths in the welded samples after the PWHTs were completed.....	75

Figure 54: The normal, longitudinal and transverse distribution for the E8018 electrode. The stress levels are measured at separate depths in the welded samples	77
Figure 55: The normal, longitudinal and transverse distribution for the E9018. The stress levels are measured at separate depths in the welded samples	79
Figure 56: E6013 heat-affected zone, grain coarsened ferrite with AC and WF can be observed. HI is at 0.5 kJ/mm. The sample was taken at 50x magnification	80
Figure 57: E7018 heat-affected zone, a grain refined and grain coarsened HAZ can be observed. HI was at 0.7 kJ/mm. The sample was taken at 50x magnification.....	81
Figure 58: E8018 HAZ, grain coarsened HAZ with AC. High HI was at 1.0 kJ/mm. The sample was taken at 50x magnification.....	82
Figure 59: The E7018-PWHT HAZ predominantly comprised of equiaxed ferrite-carbide. Sample underwent a PWHT at 600 ⁰ C for two hours. The sample was taken at 50x magnification	83
Figure 60: The E6013 WM had large quantities of GF with some BF and WF. Grains are much larger compared to other samples. The sample was taken at 50x magnification	84
Figure 61: The E7018 WM comprised AF, GF, ferrite and aligned MAC. The sample was taken at 50x magnification.....	85
Figure 62: The E8018 WM, AF and ferrite with aligned MAC is shown. The sample was taken at 50x magnification.....	86
Figure 63: The E9018 WM, comprised entirely of bainite (B). The sample was taken at 50x magnification	87
Figure 64: The E7018-PWHT WM comprising of large ferrite grains and AF. The sample was taken at 50x magnification	88
Figure 65: Schematic transverse section on AA indicating the rolling direction and cracks in the BM	89
Figure 66: Polished and measured micrograph of the E6013 electrode sample showing HIC cracks at the BM	90
Figure 67: Typical cracks observed at 500x magnification. This image was taken from sample E6013. The crack is a magnification of the red square in Figure 66	90
Figure 68: Polished and measured micrograph of the E7018 showing HIC cracks in the BM. The dimensions were 18.858x1.611 mm	90

Figure 69: Polished and measured micrographs of sample E8018 showing cracks in the BM.....	91
Figure 70: Polished and measured micrograph of the E9018, showing HIC cracks in the BM of 2.365x19.294 mm	91
Figure 71: Polished and measured micrograph of the E9018 electrode sample showing HIC (stepwise cracking) cracks at the BM of length 7.416x3.745 mm	92
Figure 72: SCC in the E9018 WM; the left-hand side is the polished micrograph, and on the right is the etched microstructure. The crack originated from the outer surface into the centre of the weld	93
Figure 73: The branch-like SCC cracking of the E9018 WM. There were severe cracks in the centre of the welded member	93
Figure 74: A SEM analysis was conducted in the crack to ensure that the crack was not progressing through the presence of a non-metallic inclusion such as slag. Spectrum 1 comprises un-corroded WM and Spectrum 2 and 3 are within the corroded condition	94
Figure 75: WM analysis in Spectrum 1 was from unaffected WM	94
Figure 76: In Spectrum 2, a significant decrease can be observed in Cr and Fe and an increase in oxygen content.....	95
Figure 77: In Spectrum 3, a significant decrease is observed in Cr and Fe, and also an increase in oxygen and carbon for the E9018 consumable.....	95
Figure 78: Slag inclusion in the WM that resulted in the failure of the E6013 sample, causing lower tensile strength	96
Figure 79: The WM yield strength and tensile strength of the E6013, E7018, E8018 and E9018 welded samples	98
Figure 80: Average hardness after the last run (capping) in the HAZ, compared with the average HI.....	102
Figure 81: The actual tensile strength was measured and compared to the tensile strength as a function of hardness at the failure position, according to BS7910:2013. These were performed for transverse and all-weld samples. The E6013 coupon's value deviated owing to a defect	106
Figure 82: Impact toughness of the WM compared to the hardness of the WM.....	107

Figure 83: Average impact strength in the HAZ was compared with the average hardness in the HAZ	108
Figure 84: The coordinate system used for the measurement of residual stress. The axis is at intercept (0, 0, 0) in the normal, longitudinal and transverse directions	109
Figure 85: The E7018 resultant residual stress calculated at varied depths below the top surface. The maximum stress does not exceed the yield strength of the WM.....	112
Figure 86: The E8018 welded sample's resultant residual stress calculated at depths 2.1, 5.2, 8.31, 11.45 and 14.52 mm	112
Figure 87: The E9018 welded samples' resultant residual stress calculated at depths 2.1, 5.2, 8.31, 11.45 and 14.52 mm.	113
Figure 88: Maximum resulting residual stress at separate depths in the WM, compared to the all-weld residual stress of the E7018 welded coupon and compared to the E7018-PWHT coupon.....	115
Figure 89: The estimated effect of an increase in preheat temperature on the minimum expected yield strength. The residual stress is close to the yield strength. As the temperature increases, there is a decrease in the minimum yield strength, therefore a decrease in residual stress.....	118
Figure 90: A) The E7018 pearlite and ferrite content at 1000x magnification. B) The E7018-PWHT sample, where spheroidising of the perlite is evident	119
Figure 91: Data from the E7018, E8018, and E9018 coupons compared to the results of Kotecki and Howden [29]. The E9018 sample cracked severely. The results were converted to Brinell. The hardness limit, according to the NACE SP0472 of 200 HB, is illustrated by A. The highest WM hardness that did not crack, determined during current study, is illustrated by B.....	121

LIST OF TABLES

Table 1: The composition limits for SA 516 Gr 70 according to the ASME boiler and pressure vessel code and actual chemical composition as determined by two laboratories (SGS Metlab Report 15-0835 A)	4
Table 2: Specified mechanical properties according to ASTM SA 516 gr 70 (ASME Section IIC-2011)	7
Table 3: Chemical composition of WM, BM and mechanical properties for study on the influence of hardness on stress-corrosion cracking by Paradowskaa and Price [19]	10
Table 4: Welding parameters used in a study to evaluate the influence of hardness on stress-corrosion cracking. As the HI increases, the cooling time increases [19]	10
Table 5: The CE and CET with their respective preheat temperatures, calculated for a HI 0.5 kJ/mm, 16 mm thick and a hydrogen content of 10 ml/100g	15
Table 6: The reduction in Brinell hardness after two PWHTs [29]	17
Table 7: Effect of preheat temperatures on the estimated longitudinal residual stress [43]	25
Table 8: Published results on the effect of preheat temperature on the final transverse and longitudinal residual stress	27
Table 9: The chemical composition of the base and WM used by Chen <i>et al.</i> [51] ..	29
Table 10: Reported yield strength, tensile strength and maximum measured residual stress.....	31
Table 11: Welding parameters used in the study by Kotecki and Howden with the SAW wire composition in Table 10. The HI was varied to produce differing hardness values in H ₂ S [29].....	36
Table 12: Chemical compositions of the wires used for the study [29].....	36
Table 13: Cracking observed owing to the hardness in submerged arc welds in H ₂ S. The hardness variation was obtained by welding with a change in voltage. It was observed that all the welds cracked above 225 HB [29]. No post-weld heat treatment was performed	37
Table 14: Number of tests to determine mechanical properties, residual stress and stress-corrosion cracking in specific locations	44

Table 15: The specified tensile strength and yield strength of the welding electrodes (ASME Section 2C 2013) and AWS 5.5	46
Table 16: The actual chemical analysis of the E7018, E8018 and E9018 WM	46
Table 17: Data verification between the thermal camera and the thermal couples ..	48
Table 18: The HI calculated for the E6013 by Methods A and B. In the table, electrodes size, amps and travel speed are included	51
Table 19: The HI calculated for the E7018 by Methods A and B. In the table, electrodes size, amps and travel speed are included	52
Table 20: The HI for the E8018 by Methods A and B. In the table, the electrode size, amps and welding speed are provided	53
Table 21: The HI for the E9018 by Methods A and B. The electrode size, amps and welding speed are provided	54
Table 22: Average HI calculated for each series according to Method A and Method B and the average of the two methods	56
Table 23: Tensile specimen dimensions used in this study [in mm]	57
Table 24: Actual test parameters used in the corrosion test, according to NACE TM0177	61
Table 25: The transverse yield strength, tensile strength and elongation for the various electrodes used and the BM properties (SAIW Report B031 & C046)	64
Table 26: The mechanical properties of the all-weld samples' tensile strength, yield strength and elongation [22]. Only one of each sample was tested	65
Table 27: Impact toughness in the WM and HAZ of the SA 516 Gr 70, E6013, E7018, E7018-PWHT, E8018 and E9018. The test temperature was 18 to 20°C	66
Table 28: Residual stress in MPa, measured at separate depths and positions for the normal, transverse and longitudinal stresses for the E7018 sample in the longitudinal direction. The E7018 electrode yield strength was 503 MPa.....	72
Table 29: Residual stress measured at separate depths and positions for the normal, transverse and longitudinal stress for the E7018-PWHT sample. The E7018 electrode yield strength was 503 MPa	73

Table 30: Residual stress in MPa, measured at separate depths and positions for the normal, transverse and longitudinal stress for the E8018 sample. The E8018 electrode yield strength was 491 MPa	76
Table 31: Residual stress in MPa, measured at separate depths and positions for the normal, transverse and longitudinal stress for the E9018 sample. The E9018 electrode yield strength was 659 MPa	78
Table 32: Length of Hydrogen-Induced Cracking (HIC) cracking lengths in BM. Values in bold indicates that crack ratios were higher than the acceptance criteria.....	89
Table 33: The E9018 minimum (all-weld) specified tensile strength according to AWS 5.5 in the stress relived condition vs the actual yield strength and tensile strength [22].	97
Table 34: The average hardness of the WM for the top, middle and bottom measurements	100
Table 35: Average hardness in the HAZ of the E6013, E7018, E8018 and E9018 electrodes.....	101
Table 36: The average HI used for each sample compared with the average hardness in the HAZ.....	102
Table 37: Hardness of the E7018 and E7018-PWHT in the WM and heat-affected zone	103
Table 38: Hardness reduction of the PWHT sample in the top, middle and bottom runs of the E7018-PWHT sample.....	103
Table 39: The average transverse tensile test hardness was calculated at the region of failure to calculate the expected tensile strength. In most samples, failure occurred in the BM, while the E6013 failed in the WM, owing to a defect.....	104
Table 40: Average hardness in the WM used to calculate the expected tensile strength	105
Table 41: Average impact strength of the WM compared with the average hardness in the WM.....	107
Table 42: Impact toughness in the HAZ compared to the maximum hardness	108
Table 43: The calculated Von Mises residual stress for principal stresses, using the normal, longitudinal and transverse components	111

Table 44: The yield strength of the filler metal, compared with the maximum residual stress measured at each level when the Von Mises failure criteria were applied...	111
Table 45: The yield strength of the all-weld tensile specimens used to compare the maximum yield strength to the magnitude of the Von Mises residual stress in the WM	113
Table 46: The resultant residual stress in MPa, calculated by the Von Mises theorem in the E7018-PWHT coupon	114
Table 47: The resultant residual stress of the E7018, compared to the E7018-PWHT at various depths below the top surface of the weld. The average residual stress is also reported.....	115
Table 48: The expected minimum yield strength (σ_{YS}) at room temperature as a function of temperature, in this case the preheat temperature. The emphasised line represents the preheat temperature where this study occurred	117
Table 49: The actual yield strength compared to the minimum expected yield strength at 75°C (where the preheat temperature was obtained) for various electrodes.....	117
Table 50: Average WM hardnesses from this study was converted to Brinell hardness. This was compared with the results that Kotecki and Howden obtained in their study as in Figure 58 [29]	121

1 INTRODUCTION

1.1 Project background

Stress-corrosion cracking (SCC) occurs in the presence of a stress, a susceptible material and a corrosive environment. The mechanism by which it occurs is not exactly clear [1]. One of the first recorded cases of SCC in South Africa occurred in 1973, resulting in the death of 22 people [2]. Since then, procedures and safety regulations were implemented to ensure reliable operation and the safety of employees.

The PQR (Procedure Qualification Record) and WPS (Welding Procedure Specification) are part of the quality process to ensure the quality of welds and safe operation. If a WPS is qualified properly and followed rigorously during fabrication, a welded joint will likely be successful. Amongst other features, this would mean that the mechanical and physical properties. Ultimate tensile strength (UTS), yield strength (YS), hardness and impact strength, will be acceptable.

In the petrochemical industry, the maximum hardness is specified for welded structures in the hydrogen sulphide service (also known as “sour service”). Failure is often attributed to a high hardness in the weld metal (WM) or in the heat-affected zone (HAZ), owing to fast cooling times. There is a hardness limit specified for the HAZ and for the base metal (BM) by the National Association of Corrosion Engineers (NACE SP0472:2015). The code limits the hardness of the WM to 210 HV₁₀ (specified as 200 HBH in the code) and in the HAZ to 248 HV₁₀. The weld will be acceptable if the hardness is below these values. One or more of the following methods can be used to control the hardness in the weld and HAZ:

- Control of cooling time between 800 °C and 500 °C (Δt_{8-5}).
- Post-weld heat treatment (PWHT).
- Temper bead welding.

Uncertainty remains on the influence of hardness in stress-corrosion cracking and whether code requirements are overly conservative. This led to the following research question: What will the effect be on SCC if WM hardness is increased systematically?

In this study, WM hardness was changed by increasing the electrode strength and SCC of carbon steel welds, investigated regarding the interrelationship of hardness and residual stress.

The stress that contributes to a stress-corrosion failure can be an applied tensile or a residual stress. Residual stresses develop during the thermal cycle of the welding process. The last part of the WM to solidify has the highest tensile residual stress [3], [4]. Residual stress can be present up to the yield strength of the WM [5]–[7].

1.2 Welding process used

The process used in this study was Shielded Metal-Arc Welding (SMAW), also known as Manual Metal-Arc (MMA) welding. This process is widely used in field installation and repair work. It is possible to use SMAW in most environments and the method is suitable for most installations.

1.3 Outline of this study

Excessive hardness may cause SCC in H₂S environments. NACE SP0472:2015 limits the hardness of the WM to 200 BHN (210 HV₁₀). The maximum hardness of the HAZ should not exceed 248 HV₁₀. These limits are regarded as the absolute maximum. The hardness of the HAZ is a function of cooling time determined by the heat input (HI) and the preheating temperature. The hardness of the shielded metal-arc WM is determined by the specified minimum tensile strength of the electrode. In this study, the hardness of the WM was changed systematically by using E6013, E7018, E8018 and E9018 electrodes. Residual stress was measured and was compared to all the weld strengths of the welded samples. The susceptibility to SCC was tested by immersing the samples in H₂S.

1.4 Research aims

The following aims were formulated for investigation:

- Simulate and measure an increase of WM hardness, above the limits specified by NACE SP 0472:2015, and residual stresses and obtain a detailed residual stress mesh.
- Investigate the susceptibility of the welded joint to SCC during immersion testing (to NACE TM1077:2005) as a function of WM hardness and residual stress in the welded joint.

1.5 Research assumptions and limitations

The following assumptions and limitations were identified:

- During welding, plates are clamped to the test bench to resist any possible distortion of plates. The resultant restraint will simulate a typical part welded in industry and cause a high level of residual stresses.
- No regard will be taken of fatigue and weld defects, such as toe concentrations and stresses.
- No regard will be provided to shear forces as a result of the restrained condition.
- Due to time limitations, no other welding process was considered.

2 LITERATURE REVIEW

2.1 Introduction

In order for SCC to occur, a susceptible microstructure, a corrosive environment and a state of stress must be present simultaneously. The stress can be an applied or a residual stress. In this section, the focus is on SCC, welding metallurgy, residual stresses, resulting stress and test methods. The hardness limitation of 210 HV₁₀ [8] in the WM will be evaluated in consort with the parameters affecting SCC in the test solution, composed of 5% NaCl, 0.5 % acetic acid in de-ionised water and saturated with H₂S [9].

2.2 Welding metallurgy

The three main parameters that determine the characteristics of a welded joint is the BM, the WM and the thermal cycle.

2.2.1 Base metal used in the study

The SA 516 Gr 70 used in this project is a P-1 steel [8]. The composition for SA 516 Gr 70 is provided in Table 1. This is a low to medium carbon steel. The carbon content varies between 0.16% and 0.28% C. The BM is the fixed parameter in the design of the welded joint. The WM is selected according to the BM.

Table 1: The composition limits for SA 516 Gr 70 according to the ASME boiler and pressure vessel code and actual chemical composition as determined by two laboratories (SGS Metlab Report 15-0835 A)

Elements %	C	Mn	Si	S	P	Cr	Mo	V	Ni	N	Al	Cu
Basis	0.28 max	0.85-1.20	0.15-0.40	0.025	0.025							
Chemical Analysis 1	0.17	1.01	0.36	0.001	0.011	0.143	0.001	0.001	0.007	0.0078	0.03	0.16
Chemical Analysis 2	0.17	1.02	0.35	0.003	0.010	0.130	0.001	0.001	0.020		0.03	0.16

2.2.2 Microstructure of the base metal

The phases present in carbon steel are body-centred cubic (δ/α -BCC), face-centred cubic (γ -FCC) and cementite (Fe₃C). At the melting point of iron (1 539°C), the crystal lattice is BCC (δ -ferrite). At 1 394°C, delta ferrite transforms to austenite. At 912°C,

austenite transforms to ferrite. Austenite has a high solubility for carbon (up to 2%). Below the Ae1 (Figure 1) line, a complete transformation occurs from γ -FCC to α -BCC. α -BCC has a much lower solubility for carbon (maximum 0.02%).

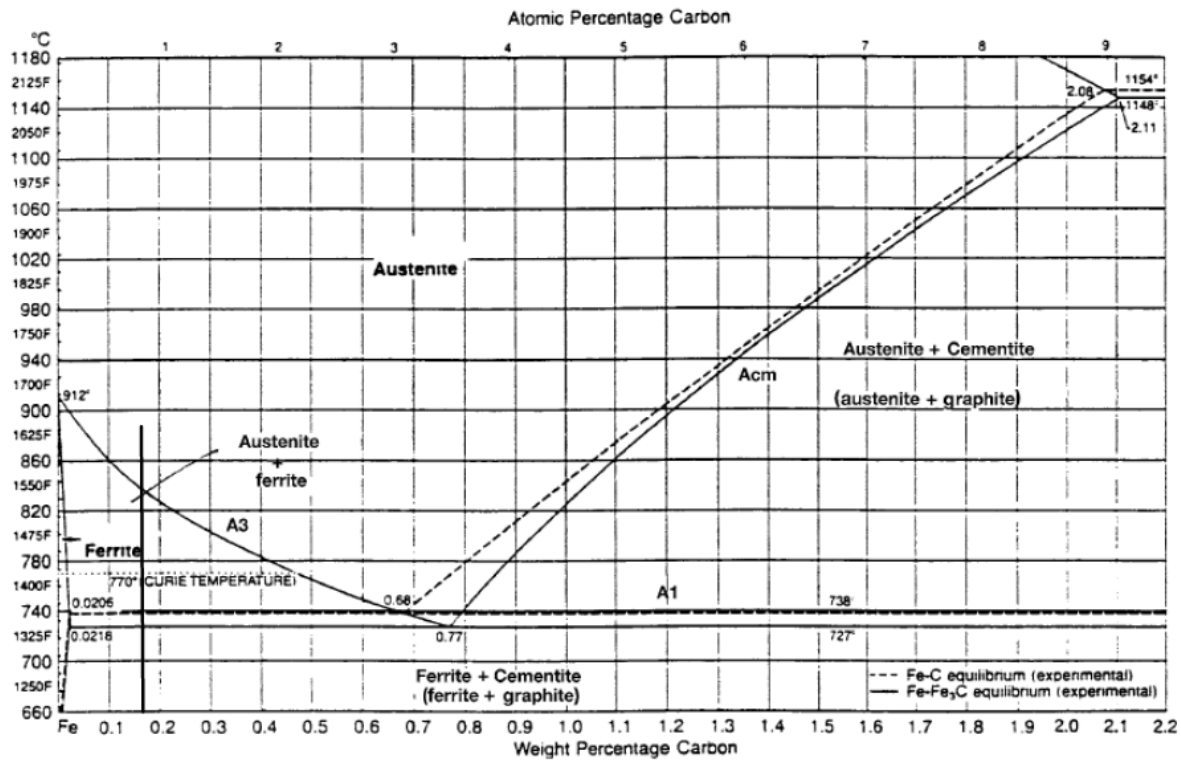


Figure 1: Iron carbon phase diagram [10]. The black line represents the carbon content of SA 516 Gr 70

In Figure 2, the microstructure of the BM is shown. This comprises ferrite and pearlite. Pearlite is a mixture of ferrite and cementite. This microstructure is obtained by hot-rolling, then air-cooling to room temperature.



Figure 2: The as-rolled microstructure of the BM (SA 516 Gr 70), comprising ferrite (light bands) and pearlite islands (dark bands), magnified 500x

2.2.3 Mechanical properties of the base metal

Figure 3 indicates the effect of alloying iron with carbon on the mechanical properties. Alloying with carbon increases the hardness and tensile strength of plain carbon steel. The mechanical properties according to the manufacturer are indicated in Table 2.

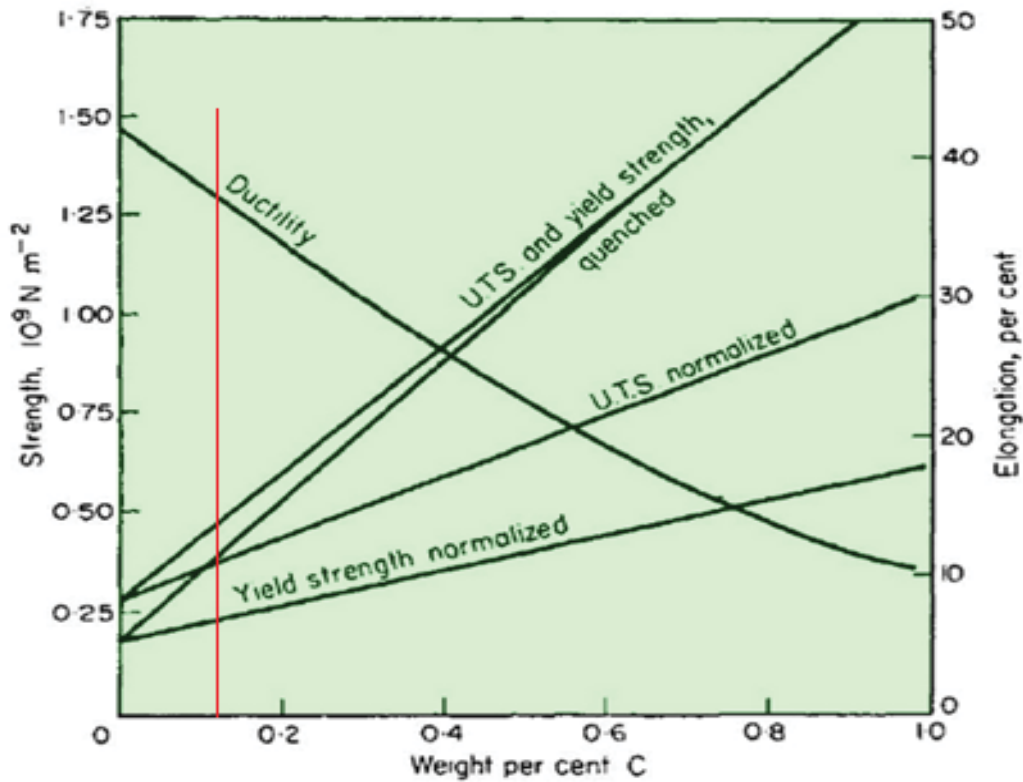


Figure 3: Influence of carbon on mechanical properties. The carbon content of the low-carbon steel in this dissertation is indicated by the red line [11]

Table 2: Specified mechanical properties according to ASTM SA 516 gr 70 (ASME Section IIC-2011)

Tensile Strength (MPa)	Yield Strength (MPa)	Minimum elongation (%) In a gauge duration of	
		50 mm	200 mm
485-620	260	21	17

2.2.4 The effect of the weld thermal cycle on the formation of microstructures in the weld metal and metallurgical zones in weld

Expected metallurgical zones after welding, from the weld metal to unaffected base metal

After a material has been welded, it contains various metallurgical zones. The WM and BMs microstructure may both substantially differ, owing to the temperature experienced during the heating cycle, and often owing to various chemical compositions. In Figure 4 from left to right it can be seen: WM, fusion line (FL), HAZ

and BM. The thermal cycle is affected by the HI and preheating temperature. The WM is subjected to the highest temperature since it is closest to the heat source. The FL indicates where the joining melted metal and the un-melted BM join. Next to the FL is the HAZ.

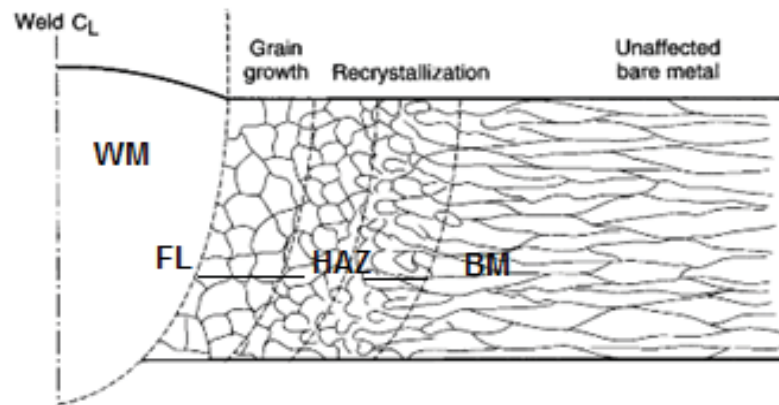


Figure 4: The result of the thermal cycle can be seen, where various zones exist, such as the HAZ and BM. The recrystallisation is caused by a high temperature during welding in the HAZ. Adapted and edited from [12]

Phase transformations in the weld metal

Typical microstructures present in carbon steel WM include primary ferrite (polygonal ferrite), ferrite side-plates (Widmanstätten ferrite (WF)), acicular ferrite (AF) and lath structures, such as martensite and bainite [13]. These structures are affected by the cooling rate as illustrated in Figure 5.

The thermal cycle during welding influences the formation of phases. The main thermal cycle transformations occur between 800°C and 500°C. It is important to control the cooling time between these temperatures when welding carbon steels.

Slow cooling

During slow cooling there is sufficient time for the carbon to diffuse from the carbon rich austenite phase, resulting in the formation of polygonal ferrite or blocky ferrite. Slow cooling is associated with a high preheat temperature and a high HI [14]. The

polygonal ferrite nucleates on austenite grain boundaries just below the A3 temperature.

Medium cooling

When the cooling rate is higher, the ferrite will nucleate first but there is less time for carbon to diffuse from the crystal lattice. Grain boundary ferrite or proeutectoid ferrite subsequently forms.

When the cooling rate is higher, α -ferrite nucleates on austenite grain boundaries, growing inwards and producing aligned ferrite plates. This is known as Widmanstätten ferrite [15]. If the cooling rate is increased, a microstructure known as AF is formed [15].

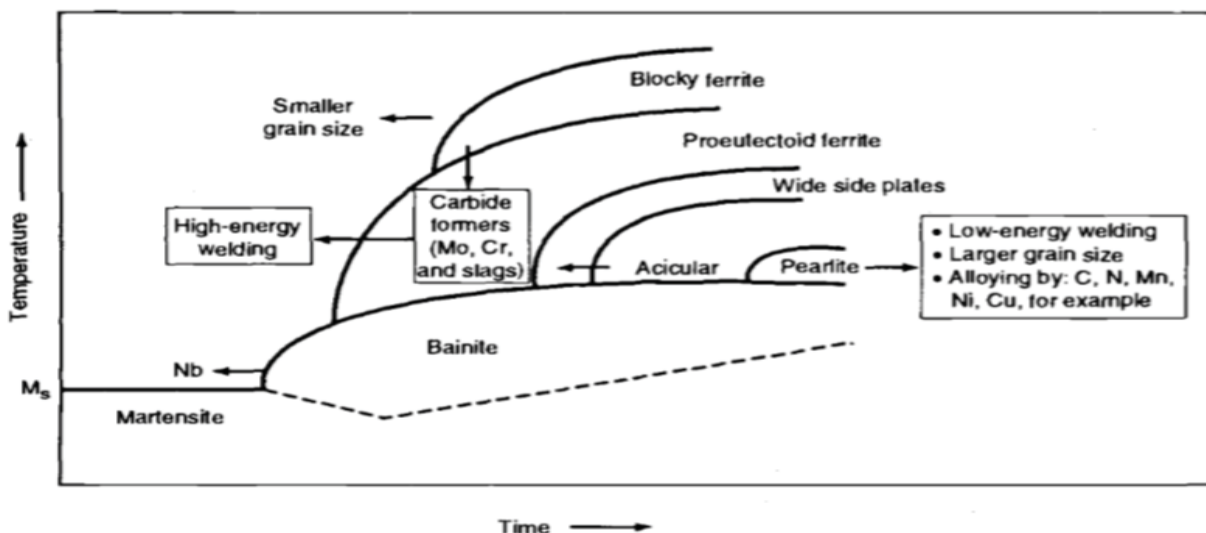


Figure 5: A typical continuous cooling transformation diagram describing the austenite transformation in WM upon cooling [16]

Fast cooling

When the cooling rate is high, there is not sufficient time for carbon to diffuse from the crystal lattice. This results in structures, such as martensite and bainite, are characterised as hard but brittle [17]. The highest hardness can be obtained if a critical cooling time is reached. This will cause a full transformation to martensite [18]. It is not desirable to have such a high hardness in a carbon steel weld since the toughness will be deficient.

Conclusion

The cooling time has a considerable influence on the weld microstructure that is formed. The microstructure present at room temperature will determine the mechanical properties.

2.2.5 The effect of heat input on hardness and width of weld

Paradowskaa and Price investigated the influence of HI on residual stress [19]. As part of the study, AS/NZA 3678:1996 grade 250 was welded, with three varying levels of HI. The manufacturing process for their samples was Flux Cored Arc Welding (FCAW). Table 3 and Table 4 indicate the welding parameters taken from their study. Figure 6 indicates the results obtained by this study. In the results, as the HI increased, the hardness decreased; as the HI increased, the weld size increased in width.

Table 3: Chemical composition of WM, parent metal and mechanical properties for study on the influence of hardness on stress-corrosion cracking by Paradowskaa and Price [19]

Chemical composition of the consumable materials in wt.%											
Composition	C	Mn	Si	S	P	Ni	Cr	Mo	V	Al	
Parent Metal	0.12	0.63	0.13	0.01	0.02	0.02	0.01	0.01	0.01	0.03	
Weld Metal	0.10	1.70	0.68	0.02	0.02	0.02	0.03	0.04	0.04		
Mechanical Properties					YS [MPa]		TS [MPa]		Elongation [%]		
Parent Metal					285		429		38		
Weld Metal					445		550		29		

Table 4: Welding parameters used in a study to evaluate the influence of hardness on stress-corrosion cracking. As the HI increases, the cooling time increases [19]

Parameters used in the experimental work	Sample	Heat input [kJ/mm]	Traverse speed [mm/min]	Electrode diameter [mm]	Current range [V]	Δt_{8-5} [s]
	1	0.8	560	1.6	260-280	5
2	1.2	360	1.6	260-280	12	
3	1.6	280	1.6	260-281	21	

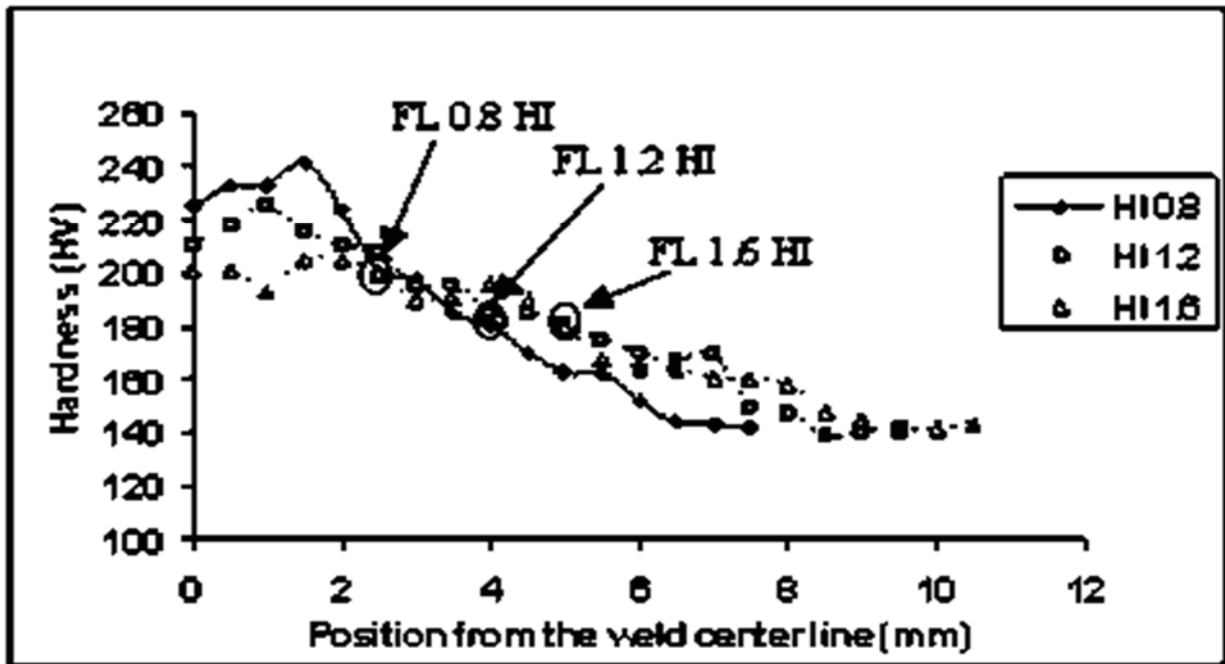


Figure 6: Hardness profiles for HIs of 0.8, 1.2 and 1.6 in kJ/mm. A higher HI results in a lower hardness in the WM (between 0 and 2 mm from the weld centreline) [19]

Hardness prediction by Lorenz [20]

The authors Lorenz and Kasuya investigated two formulas to predict the HAZ hardness as a function of the chemical composition and HI. The formula evaluates the maximum hardness of martensitic and bainite structures in the HAZ. The factors that influence the hardness are the Δt_{8-5} and material composition. The Δt_{8-5} was plotted in Figure 7.

Hardness prediction by Kasuya et al. [21]

The authors [21] determined the maximum hardness of martensite and bainite as a function of cooling time Δt_{8-5} and material composition. This formula was reported to be highly accurate when compared with test data in their study. There were two points with a logarithmic function between the $\Delta t_{8-5 M} : HV_m$ and $\Delta t_{8-5 B} : HV_B$.

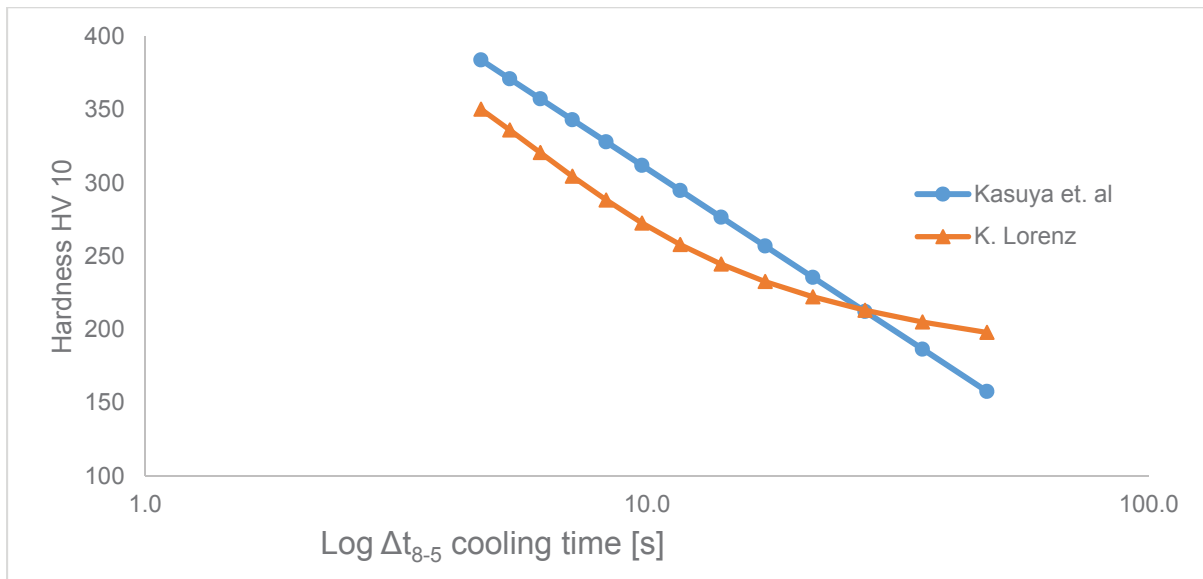


Figure 7: The predicted maximum heat-affected zone hardness (HV₁₀) for carbon steels as a function of calculated cooling time Δt_{8-5} . As the cooling time is increased, there is a reduction in hardness [20], [21]

In both of these equations, as the Δt_{8-5} is increased as a function of preheat time, there is a reduction in maximum HAZ hardness.

2.2.6 Calculation of the minimum preheat temperature to avoid hydrogen cracking

When welding carbon steels, the hardenability and hydrogen content should be considered. With increased hydrogen content and high hardness, the weld may be susceptible to hydrogen cracking. The carbon equivalent (CE) value provides an indication of the hardenability of the steel. A minimum preheat temperature is selected according to the CE, thickness, HI and expected hydrogen content. Hydrogen may be introduced into the weld pool with either consumables, flux, solvents or degreasers. Consumables and fluxes as per code indicates the level of hydrogen content.

Preheating has at least two effects, namely a reduction in the HAZ hardness and secondly, to allow sufficient time for hydrogen to diffuse from the welded joint. A higher preheat temperature increases the cooling time, resulting in a softer transformation product, with a lower risk of cracking.

During the welding process, hydrogen can be introduced in the weld pool by the electrode and coating [22]. Hydrogen can cause weld cracking [23]. A preheat temperature allows for the hydrogen to diffuse from the welded area, reducing the susceptibility for cracking. The CE is calculated through two general codes the CE is. These methods are: Method A and Method B of BS EN 1011-2:2001 (Equation 2). In this study, Method A and Method B were used to establish a minimum preheat temperature for welding SA 516 Gr 70.

$$CE(IIW) = C + \frac{Mn}{6} + \frac{Ni+Cu}{15} + \frac{Cr+Mo+V}{15} = 0.36 \quad (1)$$

$$CET = C + \frac{Mn+Mo}{10} + \frac{Cr+Cu}{20} + \frac{Ni}{40} = 0.28 \quad (2)$$

Method A

When welding with an electrode coating that comprises rutile or cellulose only, **Scale A** may be used (Figure 9). For other electrodes, **Scales B-D** can be used. As an example, the preheat temperature was calculated for a rutile electrode at HI of a 0.5kJ/mm. 0.5 kJ/mm is considered a low HI that will result in a higher preheat temperature to have an acceptable weld. The calculated CE value was 0.36. In Figure 9, the next higher CE, 0.38 was used. A minimum preheat temperature of 75°C was stated using Method A.

Conditions for welding steels with defined carbon equivalents.

Hydrogen scale to be used for a CE not exceeding:

Scale	A	B	C	D	E
CE	0.38	0.41	0.43	0.48	0.50

Figure 8: An example of the calculated CE value and the scale selected. The calculated CE value of 0.36 was the closest to 0.38 when using a rutile or cellulose electrode only, applying scale A

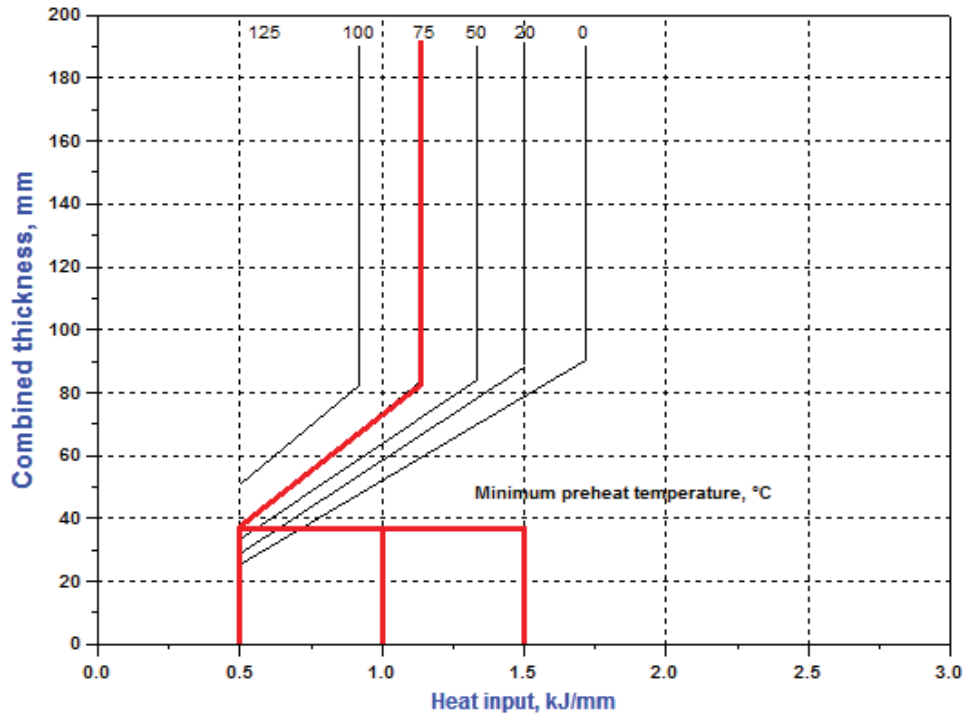


Figure 9: The hydrogen scale and equivalent were applied. For the specific HI and thickness, a preheat temperature of 75°C was selected [24]

Method B

The following calculations evaluate the plate thickness' effect ($h=16$ mm) on the heat dispersion. Increasing temperature will: result in longer cooling time

$$T_{pd} = 160 \tanh\left(\frac{16}{35}\right) - 110^{\circ}\text{C}$$

$$= -42^{\circ}\text{C}$$

The following equation evaluates the contribution of the hydrogen content to the new preheat hydrogen content (HD), as moderately conservative:

$$T_{pHD} = 62 \times HD^{0.35} - 100^{\circ}\text{C}$$

$$= 38^{\circ}\text{C} \text{ (for a HD content at 10 ml/100g)}$$

The HI has a linear effect; as the HI increases the less heat is needed in the welding joint. It is calculated at a conservative minimum of 0.5 kJ/mm:

$$T_{pHI} = (53X CET - 32)x HI - 53x CET + 32$$

$$= 9^{\circ}\text{C}$$

Lastly, the effect of the carbon equivalent (CET) is calculated:

$$T_{pCET} = 750x CET - 150$$

$$= 60^{\circ}\text{C}$$

These results can be added to have the final preheat value for the sample plates:

$$T_p = T_{pHI} + T_{pHD} + T_{pd} + T_{pCET}$$

$$T_p = 65^{\circ}\text{C}$$

In Method A, selecting a conservative HI value dictates that the minimum preheat temperature must be 75°C. If Method B is used for the same conservative approach, the minimum preheat temperature is 65°C. The most conservative preheat temperature was selected as 75°C for the welding of plates. A summary of the CE and CET method is presented in Table 5.

Table 5: The CE and CET with their respective preheat temperatures, calculated for a HI 0.5 kJ/mm, 16 mm thick and a hydrogen content of 10 ml/100g

SA 516 Gr 70	CE (Method A)	CET (Method B)
CE	0.36	0.28
Preheat, °C	75	65

2.2.7 The effect of post-weld heat treatment effect on the hardness

A PWHT may be implemented to modify the mechanical properties (such as hardness or toughness) and to reduce the weld residual stress [25]. The code for the specific industry and environments guided the PWHT application. The NACE SP0472:2015

hardness limit may be achieved by controlling the cooling rate as described in the earlier section, or by a PWHT.

A PWHT tempers any hard phases in the HAZ (NACE's SP0472:2015). The as-welded toughness may be deficient. By applying a PWHT, the toughness is increased by tempering the weld joint. The main parameters to control in a PWHT are the rate of heating, cooling time, final temperature and time at final temperature [26]. A PWHT is conducted by heating to an elevated temperature, below the lower transformation temperature A_{c1} . The A_{c1} temperature is sensitive to the chemical composition of a steel [27]. It is important that re-austenitisation does not occur during a PWHT. Such re-austenitisation may result in the formation of untempered martensite on cooling after the soaking cycle of the PWHT. Carbon steels are usually treated between 600-675°C for one hour per 25 mm of plate thickness [28].

Kotecki and Howden investigated the hardness of Submerged Arc Weld (SAW) joints in wet sulphide service [29]. The BM used in the study was A 516 Gr 70, A515 Gr 70 and A537-A. The as-welded samples were subjected to a PWHT of 621°C (1 150°F) for one hour. A PWHT was also performed at a temperature of 676°C (1 250°F) for one hour to determine the effect of a higher PWHT temperature.

The reduction in hardness in the WM during a PWHT, as reported by Kotecki and Howden (Table 6). They observed that the 621°C PWHT resulted in an average decrease of 12.5 BHN units in the WM and 15 BHN for molybdenum-bearing WM. In the HAZ, the maximum hardness was reduced by 40 HBN. The average BM hardness was reduced by 10 HBN. The increase in temperature in the second PWHT caused no additional decrease of hardness in the WM. The average hardness reduction for all the samples was 15 HBN at 621°C and 18 HBN at 676°C.

Table 6: The reduction in Brinell hardness after two PWHTs [29]

Flux	Wire	As-welded hardness	Hardness after 621°C PWHT	Hardness reduction	Hardness after 676°C PWHT	Hardness reduction
F2	EM12K	172	156	16	156	0
F1	EH14	176	162	14	x	x
F1	EH14	180	160	20	x	x
B2	EM12K	180	159	21	x	x
B2	EM12K	185	165	20	x	x
B1	EL12	185	200	-15	195	5
F2	EH14	190	169	21	x	x
B1	EL12	190	176	14	x	x
F2	EH14	195	172	23	x	x
B2	EM12-Mo	200	178	22	x	x
B2	EM12-Mo	200	185	15	x	x
B1	EM12K	205	195	10	x	x
B1	EM12K	205	190	15	x	x
F1	EH14-Mo	205	195	10	x	x
B1	EM12K	213	205	8	210	-5
B1	EL12	213	213	0	213	0
F1	EH14-Mo	216	190	26	x	x
B1	EM12-Mo	216	205	11	210	-5
B3	EM12K-2	216	200	16	210	-10
B1	EM12K	216	222	-6	222	0
B1	EM12K	234	231	3	231	0
B1	EM12-Mo	240	234	6	231	3
B3	EM12K-2	240	234	6	231	3
B1	EM12K	245	230	15	231	-1
A516-70		154	145	9	145	0
A516-70		217	178	39	172	6
A515-70		145	139	6	137	2
A515-70		210	176	34	161	15

X=not tested

2.2.8 Conclusions from the literature on the effect of hardness on the weld metal and heat-affected zone

The hardness limitation in NACE SP0472:2015 is based on preheat temperature and PWHT control. From the consulted literature, the HI, preheating and PWHT have the most influence on the microstructure and therefore the hardness. Below is a summary of the thermal control methods and the subsequent effects:

- A low HI (fast cooling time) results in a high hardness in the WM and the HAZ.
- An increase in preheat temperature will cause a longer cooling time (Δt_{8-5}). This will cause softer microstructures in the HAZ.

- The PWHT normally occurs at a lower temperature than the A_{c1} temperature to avoid re-austenitisation during PWHT. There is some reduction in hardness after a PWHT with the greatest reduction in the HAZ.

2.3 Residual stresses

During welding, residual stress is formed because of localised plastic deformation induced through thermal gradients. As the thermal gradient is induced, WM expands and contracts in a non-uniform manner. At the heat source, WM contracts during cooling to room temperature or the preheat temperature. As it cools down, WM shrinkage continues in the longitudinal, transverse and normal directions, inducing an internal stress. The elastic thermal strain induced in the WM, if complete restraint is assumed, can be estimated as:

$$\sigma = E\alpha\Delta(T_f - T_i)$$

The part of the welded joint farthest from the weld centreline will be subjected to a lower peak temperature and will cool down to the preheating temperature first [5]. The heat source continues to move, and contraction will increase until a specific part of the weld joint is at room temperature. The thermal stress results in plastic deformation. This results in a tensile residual stress in the WM. The last part to solidify or cool to room temperature has the highest tensile residual stress [3], [30], [31]. (Note that this is only an estimate and not the actual development of the “maximum” tensile stress)

Residual stresses in a welded member have transverse, longitudinal and normal components, as indicated in Figure 10. In Figure 11, a general profile of the residual stress distributions is expected in butt welds. Depending on the thickness and position where the stress is measured, either a plane strain or plane stress condition exist. Close to the surface, the normal stress is negligible and it can therefore be assumed as $\sigma_{z/N}=0$ in the plane stress condition. The highest tensile residual stress will be in the longitudinal direction [32]. The stress in the transverse direction can be reduced by limiting the external constraint on the welded member. Such reduction in constraint is difficult in practice owing to rigid structures. The normal stress is significantly lower

than the stresses in the other directions [32]. It is well known that the magnitude of residual stress is up to the yield strength present in a weld [5]–[7].

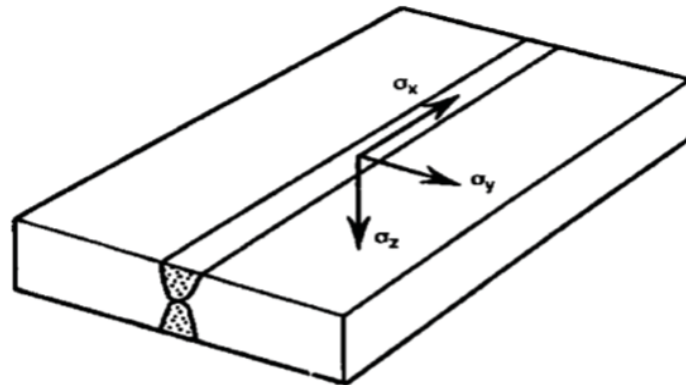


Figure 10: Expected residual stresses in three directions: Longitudinal (σ_x), transverse (σ_y) and normal components (σ_z) [32]

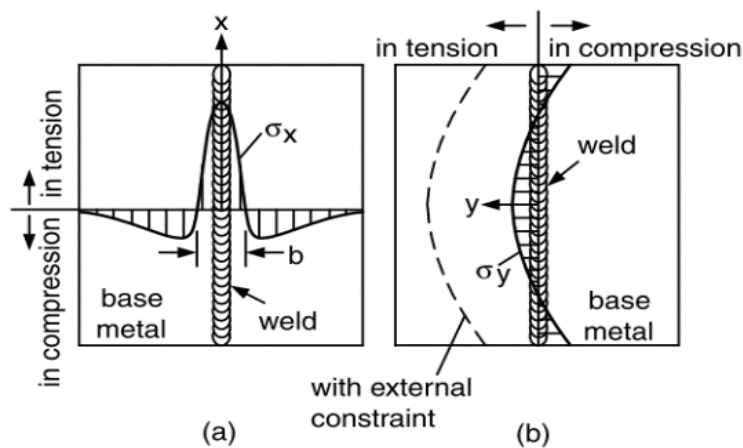


Figure 11: General residual stress patterns expected over the welded plates, a) the longitudinal stress σ_x , and b) the transverse stress σ_y [31]

2.3.1 Residual stress measurement techniques

Stress measurement techniques can be divided into destructive, semi-destructive and non-destructive techniques in Figure 12. In this section, non-destructive methods are discussed briefly in consort with one semi-destructive technique: the deep hole-drilling (DHD) method. This method was used in earlier work; for this reason, it is discussed. The ring core technique is not considered as applicable to the study.

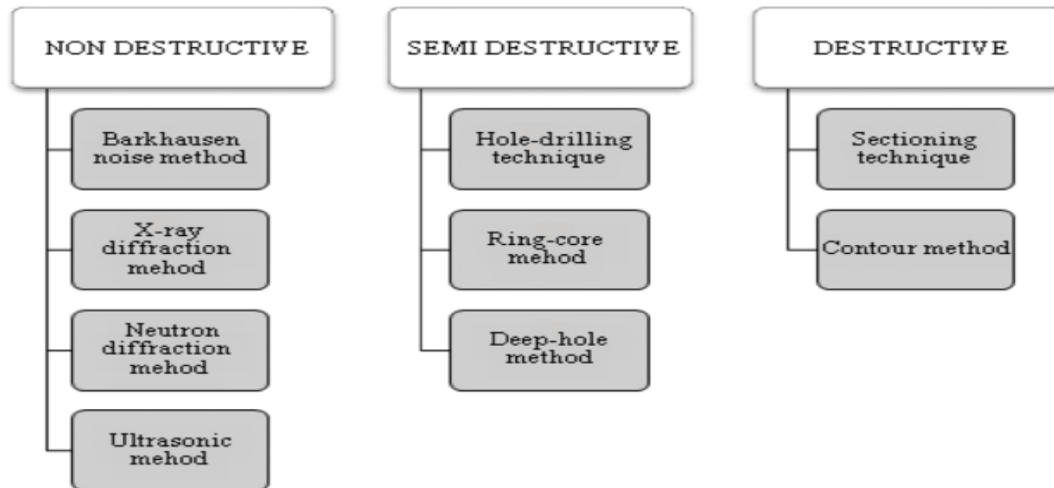


Figure 12: Different measuring techniques for residual stress [33]

Semi-destructive techniques

The DHD method can determine levels of stress in a structure. The principle of this technique is based on stress relaxation. By fixing strain gauges in a rosette around a spot, then carefully drilling into it, the change of strain around the hole can be determined. This change in strain can be related back to the principal stress [34]. This technique is widely applied in industry to measure residual stress on and just below surfaces; the process is a semi-destructive technique. With this technique a depth of 50 μm can be evaluated. It is noteworthy that drilling itself may induce plastic deformation, resulting in the formation of additional residual stresses, however with qualified procedure, the residual stress can be ground out at the surface.

Non-destructive techniques

Barkhausen effect method

Barkhausen noise arises in ferromagnetic steels, gradually magnetised or demagnetised when complete magnetic domains suddenly switch alignment in the varying magnetic field. The method depends on the chemical composition of the steel. It is necessary to use calibrated standards for accurate measurements. The equipment is portable but limited to magnetic materials [35]. Inclusions, defects and crystal

structures produce magnetic jumps, resulting in sound interpreted as stress. This is useful to measure macro stress, or stress over a grain, and sub-microscopic stress over an area [36].

X-ray diffraction

X-Ray diffraction (XRD) is a common practice in measuring residual stresses. The physical basis for XRD measurement of residual stresses is that a material under elastic strain experiences a change in crystal lattice spacing. The stress is thus not directly measurable, but by assuming a linear elastic deformation of the crystal lattice, the residual stress can be calculated. The X-rays are diffracted off the crystal structure. The X-ray wavelengths are $\lambda = 0,1 - 0,2 \text{ nm}$. It was used since the 1960s [37]. The penetration capability is limited to 50 μm below the surface.

Neutron diffraction

As in XRD, the neutron diffraction (ND) technique measures the spacing between crystal planes. Residual stress affects the crystal structure spacing. The change in state of the crystal structure will lead to diffraction at various angles. This relationship measures and records residual stress. The penetration of a neutron is up to 50 mm in carbon steel. This is a significant advantage compared to XRD. The ND process can measure spatial resolution down to $1 \times 1 \times 1 \text{ mm}^3$. This can map out the stresses in a welded member. The accuracy depends on the d-zero value (Section 2.3.2 discusses this in detail). The ND process is a time-consuming technique, as strains have to be measured in three directions for an element [5].

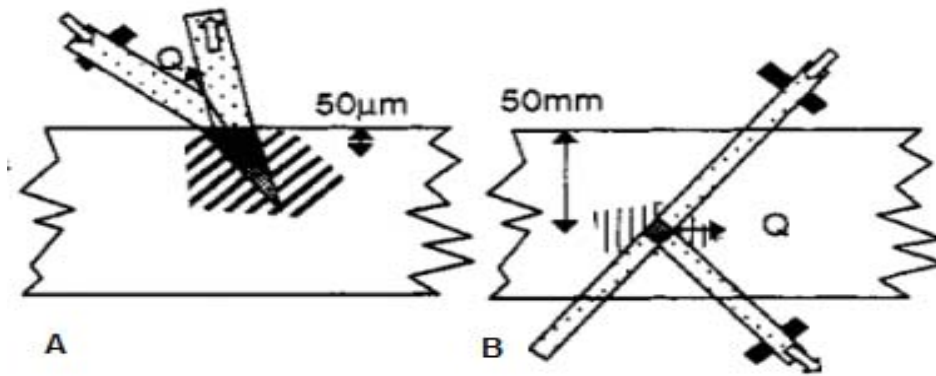


Figure 13: Comparison of the two techniques: XRD (A) and ND (B). The penetration is significantly higher for ND [38]

Summary

The ND process can measure a spatial resolution down to $1 \times 1 \times 1 \text{ mm}^3$ and 50 mm penetration depth, compared to XRD that can only measure the residual stress at the surface of the component. XRD is therefore the preferred choice when conducting a study on surfaces such as SCC. One of the objectives of this study was to measure the magnitude and direction of the residual stress in a particular welded joint as a function of the position in three dimensions. The ND measuring technique was therefore selected.

2.3.2 Detailed discussion of the neutron diffraction measurement technique

A neutron beam penetrates a crystal lattice. The neutrons in the beam have a synchronised wave length. As the neutrons travel through the various planes spacing d_{hkl} , a correction is needed for the wavelength that penetrates the sub-surface or sub-plane d_{hkl} . The neutrons penetrating the through-thickness of the plane takes longer to travel the same distance. The electron also loses energy (linear absorption coefficient) as it penetrates through the lattice. The linear absorption coefficient needs to be taken into consideration to ensure the material and thickness will be penetrated [39]. The neutron beam is diffracted by the crystal structure present in the weld. The result is a diffraction pattern, illustrated in the second image in Figure 14. The diffraction pattern can be calculated using Bragg's law in the equation below. If there is a change in plane spacing d_{hkl} , it results in a change of angular position of the

diffraction peak θ . The following equations and values are used in the basic calculations of diffraction [38].

$$\lambda = 2d_{hkl} \sin \theta$$

Where:

λ = neutron wavelength;

d_{hkl} = distance between the lattice plane spacing for the hkl reflection; and

θ = half-scattering angle as in Figure 14.

The first peak is measured in its stress-free state, and after an adjustment is performed, the difference in peaks is calculated; the elastic strain then equals:

$$\varepsilon_{hkl} = \frac{d_{hkl} - d_{hkl}^0}{d_{hkl}^0}$$

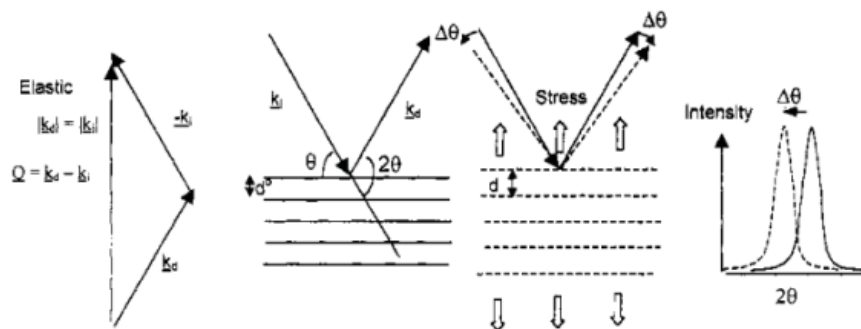


Figure 14: Waves diffracted off a crystalline surface. As the spacing increases, the diffraction angle will decrease(θ). The dark line is the $d^0_{(hkl)}$ value and the shift in peaks is used in calculating the change in elastic strain [38]

A weld is a polycrystalline material, with various metallic phases. Phases, such as ferrite (BCC), austenite (FCC) and cementite (Fe_3C), have a characteristic lattice spacing [40]. The lattice spacing is measured in the unstrained condition and recorded. If the initial strain is known, the stress can be calculated by applying Hooke's law. The changes in the crystal lattice are recorded as diffraction peak positions. The elastic constants are used to calculate the stress.

2.3.3 The influence of heat input and preheat temperature on residual stress

In Figure 15, the schematic effect of a higher HI on residual stress is illustrated. It can be expected that the maximum residual stress will be of the same magnitude. The average stress will be lower for a lower HI because of a smaller area, approaching the yield strength in tension over the WM [41].

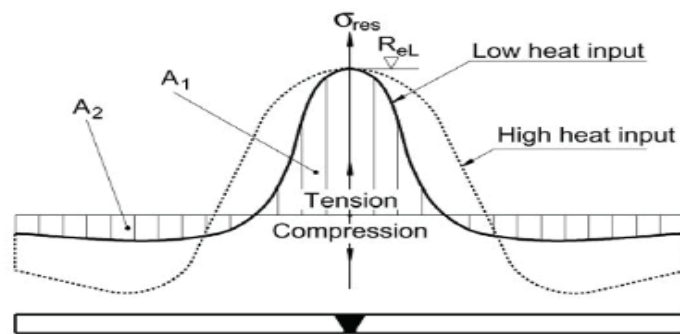


Figure 15: Schematic representation of the calculated effect of various HIs on the size and area of residual stress in the longitudinal direction. It can be observed that a lower HI results in a smaller stress area [41]

Paradowskaa and Price did an experimental investigation on the effect of HI on the residual stress in the WM [19]. The HI was varied from 0,8 to 1,6 kJ/mm by varying the travel speed during Gas Metal Arc Welding (GMAW) from 280 to 560 mm/min. The BM used in the study was AS/ NZS 3678:1996 Gr 250 structural steel.

The authors measured residual stress in the longitudinal and transverse directions. The measuring technique was ND at 1.5 mm below the surface. In the longitudinal direction, the peak stress occurred in the WM, close to the FL, for the three levels of HI used during this study. For the transverse residual stress, the highest peak was close to the FL at a HI of 0.8 kJ/mm. There was a decrease in the stress area in the WM as the HI decreased (Appendix C). The authors concluded that the highest stresses occurred in WM or close to the FL. It was noted that as the HI increases, the area under tension increases in the WM.

Silva *et al.* undertook an investigation to determine the residual stress, microstructure and hardness of thin-walled low-carbon steel pipes using multi-pass welds [42]. The

chosen process was Gas Tungsten Arc Welding (GTAW). The HI was varied between 0,83 – 1,5 kJ/mm by varying the travel speed between 39-83 mm/min, welding current between 98,2 – 150,6 amperes (A) and a voltage of 10,9 – 12,2 volts (V). The BM used in the study was SA 106 Gr. B with a yield strength of 357 MPa and a tensile strength of 512 MPa. A standard ER 70 S3 electrode was used with a yield strength of 420 MPa and a tensile strength of 516 MPa. The axial peak residual stress for high HI (1.0 – 1.5 kJ/mm) was 355 MPa compared to the low HI (0.83 – 1.24) of 250 MPa.

The use of a higher preheating temperature results in a reduction of residual stress, as demonstrated in studies of the influence of thermal properties and preheating on residual stresses in welding [31], [41]. The preheat temperature ranged from 0°C to 250°C and the gas metal-arc welding (GMAW) process was used. The HI was 0.48 kJ/mm with the current at 100 A and a voltage of 30 V, process efficiency of 0.8 (η) and travel speed (v) of 300 mm/min. The BM and WM used in this study was ST 37 with a yield strength of 235 MPa and the tensile strength of 360-510 MPa.

The residual stress was calculated by computational analysis. The calculated residual stress was reduced from 278 MPa to 238 MPa by increasing the preheating temperature from 25°C to 250°C, as illustrated in Table 7. It was determined that up to a 16% reduction can be obtained in residual stress owing to a high preheat temperature of 250°C [43].

The study concluded that as the preheat temperature increases, the longitudinal residual stress decreases in the welded joint. No data on the transverse residual stress was presented. It should be noted that the calculations reported by Armentani *et al.* [43] estimated a longitudinal stress that was higher than the assumed yield strength for all preheating temperatures. The assumed degree of restraint was not reported.

Table 7: Effect of preheat temperatures on the estimated longitudinal residual stress [43]

Preheat [°C]	Peak residual stress [MPa]	Residual stress /Yield Strength
25	278	1.18
75	270	1.15
150	260	1.10
250	238	1.01

In a Finite-Element Modelling (FEM) study, the effect of welding conditions on residual stresses occurring in butt welds was investigated by Teng and Lin [44]. The preheat temperature was simulated from 0°C-400°C. The HI used was 0.308 kJ/mm with a current of 110 A, a voltage of 20 V, an arc efficiency of $\eta= 70\%$ and travel speed of 300 mm/min (v). The yield strength of the material was taken as 110 MPa at room temperature. The residual stress for various preheat temperatures was calculated by ANSYS finite-element analysis and the results report a decrease of 25% in the transverse residual stress, with an increase in temperature from 0°C-400°C. No data on the longitudinal residual stress was presented.

Aalami-Aleagha *et al.* investigated the preheat temperature effect on the thermal cycle and on the residual stress by using a three dimensional finite-element analysis [45]. The HI used for this study was 1.1 kJ/mm with a current of 110 A, a voltage of 20 V and travel speed of 120 mm/min. The simulated results below are for preheat temperatures of 50°C and 200°C. The yield strength of the material tested was 256 MPa at room temperature. They simulated the axial stress for the inner surface and outer surface of a 20-inch (508 mm) diameter pipe. The model was validated by welding a 1-inch (25.4 mm) diameter pipe. Figure 16 indicates the results on the 0° degree position of the pipe.

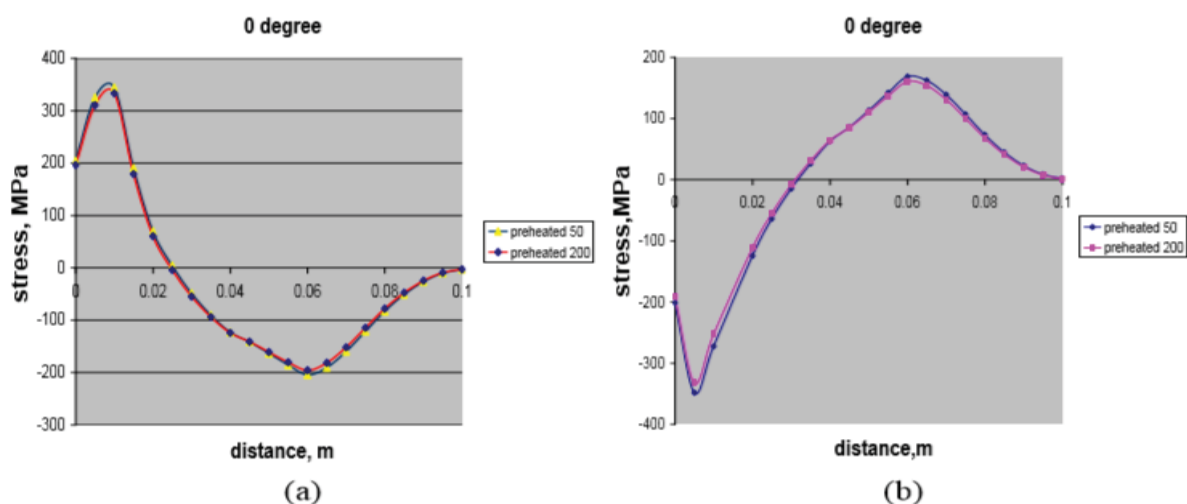


Figure 16: Calculated residual stress at a) the inner surface that is in tensile while at b), the outer surface is in compression. A preheating temperature of 50°C and 200°C was used in the calculation of the residual stress [45]

This study concluded that the residual stress in the axial direction was reduced slightly as the preheat temperature was increased. Comparing the stress states for 50°C and 200°C show a minimal difference. These results agree with earlier findings where the stress decreases, though the earlier findings provided larger changes than this study. In the study, that the measured residual stress exceeded the yield strength by 100 MPa, at about ±10 mm from the inner surface of the tube (wall thickness was about 100 MPa). It should be noted that Figure 18 only indicates the calculated axial component of the residual stress. In a weld, a triaxial Von Mises (equivalent stress) will not be higher than the yield strength (Section 5.4.2).

From Table 8, the calculated tensile residual stress in the transverse and longitudinal direction is reduced by a fairly low quantity (less than 25% of the yield strength), even if the preheating temperature is increased by a substantial quantity (up to 400°C). It is important to note that none of the studies indicated the degree of restraint for the weld joint.

Table 8: Published results on the effect of preheat temperature on the final transverse and longitudinal residual stress

Author	Aalami-Aleagha <i>et al.</i> 2014 [45]	Armentani <i>et al.</i> 2007 [43]	Teng and Lin 1998 [42]
Orientation of residual stress modelled	Transverse	Longitudinal	Transverse
Preheat temperature range °C	50;200	0-250	0-400
Transverse residual stress reduction owing to change in preheat temperature	<5%	16%	<25%

2.3.4 Earlier work on the effect of post-weld heat treatment on residual stress

In the as-welded condition, the residual stress may be equal to the yield strength of the WM at room temperature [5]–[7]. A PWHT will cause a relief of the stress [47].

The effect of a PWHT was evaluated by Dong *et al.* [47]. The effect of a PWHT on the final residual hoop stress in pipeline steels was investigated (the hoop stress will be the equivalent of the longitudinal stress in this case). The actual weld process comprised of welding a pipe with an inner diameter of 180 mm and outer diameter of 290 mm with a circumferential weld. The welding parameters implemented were a

current of 200 A, and a voltage of 25 V. The welding speed and process was not reported. The residual stress was measured through the DHD method, validated with an FEA model. The material used in the study was P91.

Figure 17 indicates, as the PWHT treatment occurs, what the reduction in final residual stress was in the welded section. This comparison was performed 5 mm below the outside surface of the pipe.

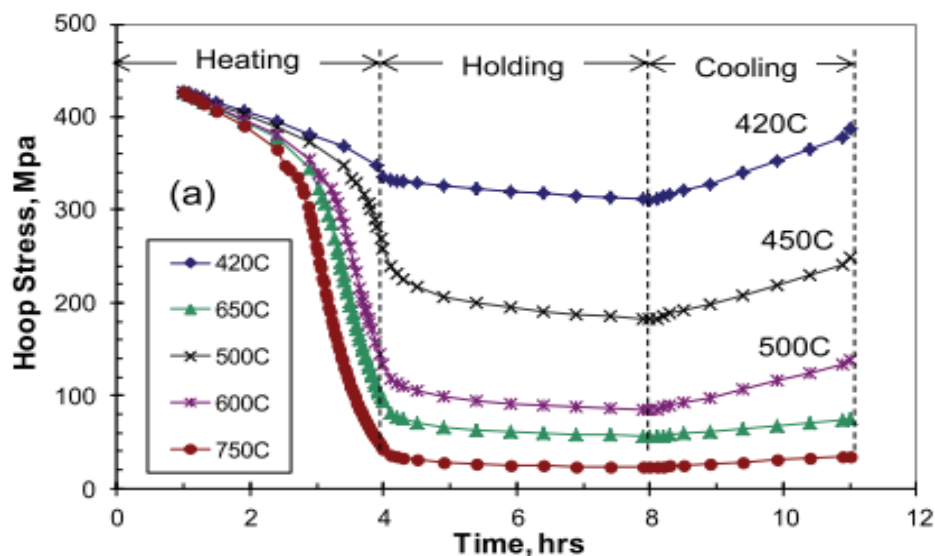


Figure 17: The calculated effect of varying PWHT time and temperature on the residual stress for P-91 creep resistant steel [49]

Olabi and Hashmi investigated the effect of various PWHTs and cooling rates on residual stress [50]. The GMAW process was used to weld AISI 1020. The sample thickness was 10 mm, with a double-V preparation. The stress was measured away from the weld centreline at distances from 15 mm to 80 mm. The DHD technique was employed to measure the residual stress. The results are indicated in Figure 18. A decrease in residual stress occurs with an increase in PWHT temperature.

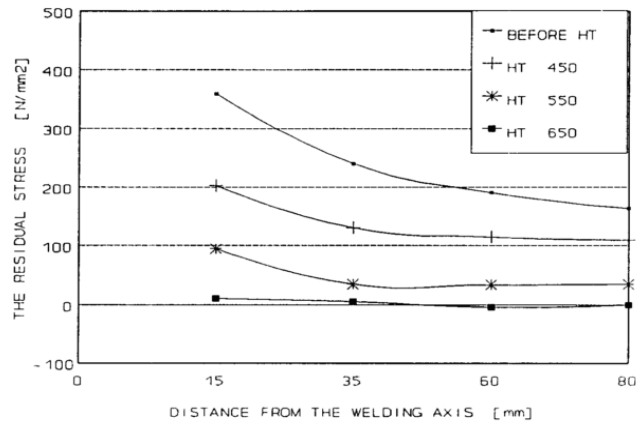


Figure 18: The result of various PWHTs on residual stresses. As the PWHT temperature was increased, the tensile residual stress decreased [50]

In situ, ND measurements determined the residual stress at varying PWHT temperatures [51]. The pipe dimension was 300 mm long, with a wall thickness of 10 mm and an outside diameter of 170 mm. The pipe material was C-Mn, while the filler metal used for the welding was a 2Cr-Mo1 electrode. The chemical composition used for the base and WM is illustrated in Table 9.

The samples were manufactured with full-penetration multi-pass butt welds with a combination of GMAW and MMA welding. There was no data on the preferred HI. The residual stress relaxation was measured during the PWHT at a temperature range of 50°C-650°C. The heat treatment was applied by using electric heating blankets. The residual stress was measured during heat treatment in the WM by the ND method with a gauge volume of 4x4x4 mm.

Table 9: The chemical composition of the base and WM used by Chen *et al.* [51]

Material	C	Si	Mn	P	S	Cr	Mo	V	Ni	Al	Cu	Ti
Weld metal	0.10	0.32	0.80	0.01	0.00	1.98	0.82	0.01	0.03	0.01	0.03	0.01
Base metal	0.25	0.27	0.54	0.02	0.01	0.04	0.01	0.01	0.02	0.02	0.01	0.01

In Figure 19, the residual stress was measured in the WM at approximately 2.5 mm from the top surface in the hoop, radial and axial directions. The hoop stress was the largest of the three components. In Figure 20, the equivalent stress was calculated by the von Mises Stress and compared with the stress in welded joints in tube and plate

products; this will be discussed in detail in Section 2.4. From the results, as the PWHT temperature increased, the residual stress decreases. At 50°C, the resultant residual stress was 250 MPa. This was the only reference where the residual stress was represented in the resultant form. Chen *et al.* did not report the yield strength of the steel [51].

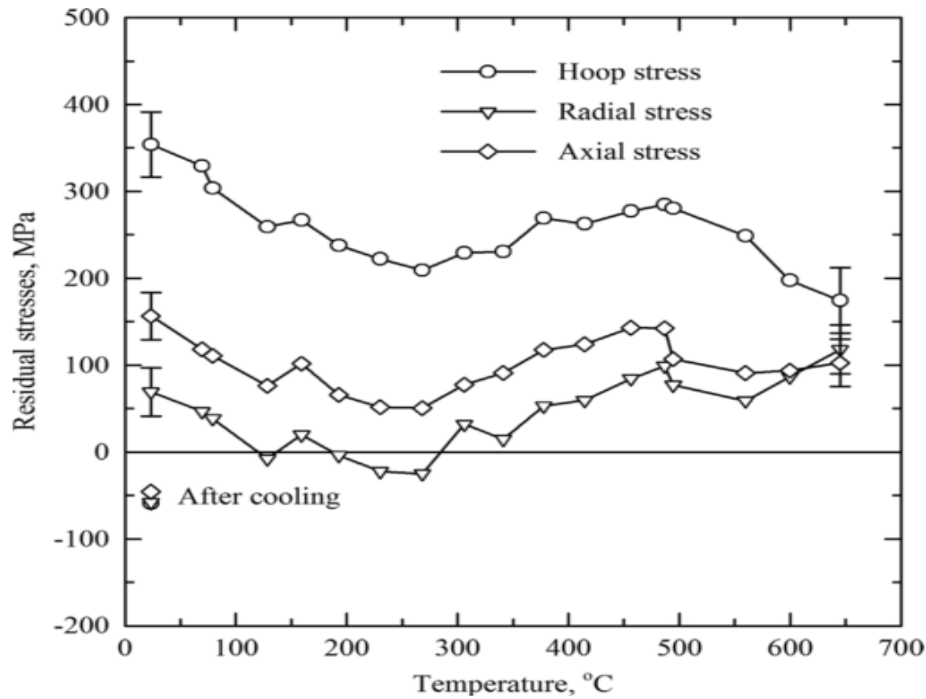


Figure 19: The in situ residual stress measurement of the WM for the hoop, axial and radial stress. The measurement was performed in the WM at approximately 2.5 mm from the outer surface [51]

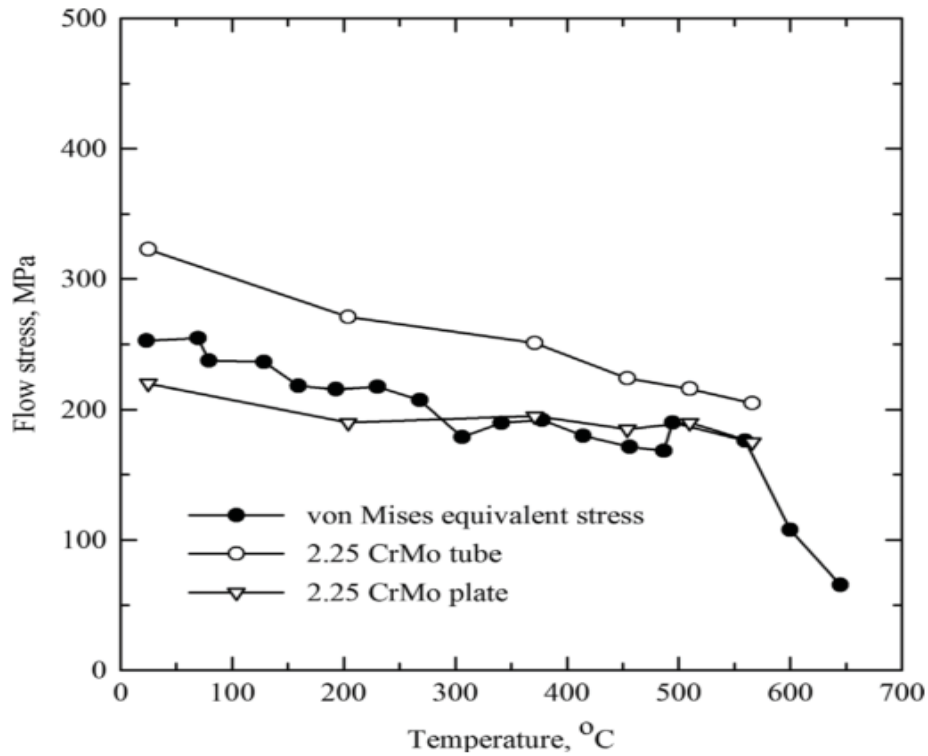


Figure 20: The residual Von Mises Stress calculated for the hoop, axial and radial component as the PWHT was applied. It was compared with the yield strength of pipes and plates [51]

2.4 The use of the Von Mises criterion to evaluate residual stress

2.4.1 Introduction

As stated earlier, residual stresses in the welded joint may be as high as the yield strength of the WM [5]–[7]. Conversely, some researchers reported residual stress values higher than yield strength of the WM or BM [19], [43], [45], [52]–[54] as in Table 10.

Table 10: Reported yield strength, tensile strength and maximum measured residual stress

Authors	Ref.	Yield strength [MPa]	Tensile strength [MPa]	Maximum residual stress [MPa]
Paradowska and Price	[19]	445	550	550
Armentani <i>et al.</i>	[43]	235	360-510	278
Alipooramirabad <i>et al.</i>	[52]	470	Not stated	550
Woo <i>et al.</i>	[53]	430	630	490
Kim <i>et al.</i>	[54]	551	569	720

From the triaxial stress state, a resultant stress can be calculated; a comparison can thus be reached of the magnitude of the stress with the yield strength. The maximum distortion theory criteria (Von Mises yield criterion) can evaluate a triaxial stress state and compare it with design limits [55], [56].

2.4.2 Maximum distortion energy theory (Von Mises theorem)

The maximum distortion theory calculates where yielding starts. It compares the distortion strain energy per unit volume with the yield strength of a specimen in simple tension or compression. It will indicate when plastic flow occurs. This method is known as the Von Mises yield criterion.

If a specimen is placed under a tension σ , then yielding will occur when $\sigma \geq S_{YS}$. The effective stress is known as the Von Mises stress (σ'). It is regarded as the most accurate failure theory [55], [56].

Yielding will occur when $\sigma' \geq S_{YS}$. Since the Von Mises stress for a triaxial stress state is:

$$\sigma' = \left[\frac{(\sigma_1 - \sigma_2)^2 + (\sigma_2 - \sigma_3)^2 + (\sigma_3 - \sigma_1)^2}{2} \right]^{\frac{1}{2}}$$

Then, at yielding:

$$S_{YS} = \left[\frac{(\sigma_1 - \sigma_2)^2 + (\sigma_2 - \sigma_3)^2 + (\sigma_3 - \sigma_1)^2}{2} \right]^{\frac{1}{2}}$$

For the coordinate system of:

$$S_{YS} \geq [\sigma_N^2 + \sigma_L^2 + \sigma_T^2 - (\sigma_N\sigma_L + \sigma_N\sigma_T + \sigma_T\sigma_L)]^{\frac{1}{2}}$$

Where:

σ_L = longitudinal stress

σ_T = transverse stress

σ_N = normal stress

2.4.3 Relationship between residual stress and Von Mises theorem

This study concluded that the residual stress is up to that of YS. With the Von Mises Stress and actual yield strength, the exact relationship can be established.

During this investigation, only one author [51] used the Von Mises' theorem to calculate the Von Mises residual stress for the hoop, axial and radial stress. This was used to evaluate residual stress as a function of PWHT from 23°C to 650°C. The actual yield strength of the material was not reported.

2.4.4 Summary of conclusions from studies on residual stress in welds

- The last part that cools down has the highest tensile stress. This implies that the WM has the highest tensile residual stress. The highest stress in the longitudinal direction occurs in the WM, up to the FL.
- There are residual stresses in the longitudinal, transverse and normal directions in a welded member. This means that at each specific point, there is a triaxial state of stress.
- In some cases, residual stresses higher than the yield strength were reported by, for example, the studies by Armentani *et al.* [43] and Aalami-Aleagha *et al.* [45]. No evaluation of the Von Mises residual stress was measured in WM.
- There are variations of stresses owing to various HIs.
- There is a reduction in residual stress between preheat temperatures from 0-400°C.
- Most of the residual stress results applicable to the present study only deal with longitudinal and transverse stresses in the plane stress condition. The mathematical models do not compare results with actual measured stress from welded samples.
- There was only one source that used the Von Mises Stress to calculate a resultant residual stress, although the actual yield strength of the steel was not reported.

2.5 Stress-corrosion cracking and Hydrogen-Induced Cracking

2.5.1 Introduction

SCC is the combined effect of a tensile stress with a susceptible material in a corrosive environment (Figure 21). SCC is influenced by the following factors: chemical composition, environmental factors, and the state of stress. It is often observed that SCC failures occur well below the design stress and yield strength [57]. The stress required to start SCC can be an applied or a tensile residual stress.

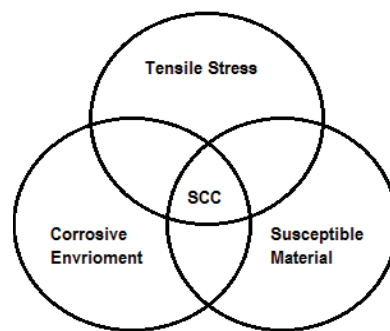
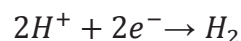


Figure 21: Representation of factors influencing SCC

SCC occurs in three stages of crack development. After the threshold stress intensity $K_{I(SCC)}$ occurs under a constant load, the crack progresses through to stage one. In stage one, crack growth is a function of the stress intensity (K). In Stage 2, crack growth is dependent on the environment and temperature. When subcritical growth occurs, it progresses into Stage 3, in which an unstable fracture occurs. Hydrogen-induced cracking (HIC) occurs when hydrogen atoms diffuse into the metallic lattice in the BM and combines to create the reaction of:



The resulting hydrogen gas molecule creates internal pressure in the crystal lattice and forms cracks as the hydrogen wants to diffuse from the lattice. Typical cracks are fast-growing, transgranular and highly brittle. The transgranular cracks usually has a sharp tip [58].

2.5.2 Corrosive environment for test work according to NACE TM1077-2005

In the petrochemical industry, wet hydrogen sulphide (H_2S) may be present, indicating an extremely harsh environment (“sour service”) with a severely corrosive effect on metals. The industry standard used to prevent in-service environmental cracking of P-1 carbon steel weldments in sour service is NACE SP 0472-2010. SA 516 Gr 70 is a qualified P-1 carbon steel [59]. Hydrogen and stress act together for cracks to propagate. The test environment, according to NACE TM0177-2005, is a solution composed of 5% NaCl and 0.5 % acetic acid in de-ionised water, saturated with H_2S .

2.5.3 Hardness limits to prevent cracking in H_2S

High stresses in the presence of hydrogen or acids can induce hydrogen cracking in a welded joint. The normal regions of attack are hard zones, usually in the HAZ. In 1984 in Illinois, a pressure vessel operating in propane and H_2S ruptured. The operating material was SA516 Gr 70 welded with full-penetration SAWs. The failure was attributable to a repair weld by SMAW, with no pre- or post-heating. The HAZ of the repair weld had a hardness of 45 HRC (450 HV_{10}). No PWHT or preheat temperature was required at that stage for a repair weld [60].

Research was performed on SAW in wet sulphide conditions [29]. The study was conducted on SA516 Gr 70, SA515 Gr 70 and A537-A in 5% NaCl, 0.5% acetic acid in 94.5% de-ionised water and saturated with H_2S [9]. Different hardness values were obtained by varying the welding voltage (Table 11). The focus of the study was on the WM properties [29]. A PWHT was applied at 621°C and 676°C to measure the reduction in hardness after heat treatment. The welding parameters and electrode composition are illustrated in Table 12.

It was observed that when the hardness of the WM was above 236 HV_{10} (225 BHN), all samples cracked in the WM. In the range of 203-225 HV_{10} (194–214 BHN), some cracked with the use of fused flux (F1, F2) at the arc restart. The test was repeated, and it was concluded that arc restarts at borderline hardness does not cause cracking in H_2S saturated solutions. Below 191 BHN (200 HV_{10}), none of the samples cracked. A537-A BM cracked extensively in the HAZ; the results are indicated in Table 13. It

was concluded that deposited hard spots in welded joints using bonded fluxes (B1, B2) resulted in initiation sites for cracking.

Table 11: Welding parameters used in the study by Kotecki and Howden with the SAW wire composition in Table 10. The HI was varied to produce differing hardness values in H₂S [29]

Parameter	Low Voltage(Low heat input)	High voltage (High heat input)
Electrode size	5.6 mm	5.6 mm
Polarity	DCRP	DCRP
Amperage	550±26	550±26
Voltage	33	38
Travel speed [mm/min]	406	406
Interpass temperature [°C]	150±6	150±6
Stick out [mm]	38	38
HI [kJ/mm]	3.1	3.6

Table 12: Chemical compositions of the wires used for the study [29]

Analysis [%]							
Wire designation	Mn	Si	C	Cu	Mo	P	S
EL 12	0.44	0.08	0.09	0.03	...	0.007	0.021
EM 12 K	1	0.25	0.14	0.08	...	0.008	0.023
EM12 Mo	0.88	0	0.1	0.03	0.58	0.011	0.026
EH 14	1.74	0	0.16	0.14	...	0.15	0.025
EH14 Mo	1.98	0	0.13	0.2	0.65	0.011	0.028
EM 12 K 2	1	0.34	0.12	0.04	...	0.018	0.028
EM 12 K 1	0.75	0.25	0.12	0.04	...	0.018	0.028
EH 14-1	1.89	0.02	0.06	0.009	0.017

Table 13: Cracking observed owing to the hardness in submerged arc welds in H₂S. The hardness variation was obtained by welding with a change in voltage. It was observed that all the welds cracked above 225 HB [29]. No post-weld heat treatment was performed

Flux	Wire	Welding condition	Hardness Brinell	Weld cracking/ No cracking
B1	EM12K	High voltage	241	7 weld cracks
B3	EM12K-2	High voltage	238	weld cracks mostly with arc restart
B1	EM12-Mo	High voltage	232	6 weld cracks
F1	EH14-Mo	A5.17-69	226	4 weld cracks next-to-last pass
B1	EM12K	Modified high voltage	225	3 weld cracks
B1	EL12	High Voltage	214	1 weld crack
B1	EM12-Mo	A5.17-69	214	No cracks
B2	EM12-Mo	High voltage	208	No cracks
B1	EM12K	A5.17-69	205	1 weld crack in next-to-last pass
B3	EM12K-2	A5.17-69	205	No cracks
F1	EH14-Mo	High voltage	200	5 weld cracks, all with arc restart
B2	EM12-Mo	A5.17-69	199	No cracks
F2	EH14	A5.17-69	199	No cracks
F2	EH14	High voltage	194	1 weld crack only 16 days exposure
F1	EH14	High voltage	191	No cracks, only 16 days exposure
B2	EM12K	A5.17-69	190	No cracks
F1	EH14	A5.17-69	186	No cracks
B1	EL12	A5.17-69	181	No cracks
B2	EM12K	High voltage	181	No cracks
F2	EM12K	A5.17-69	174	No cracks
B1	EM12K	A5.17-69	209	No cracks, stress relieved
B1	EL12	Modified high voltage	195	No cracks, stress relieved

B1 - Bonded, High metallic Mn and Si
 B2 - Bonded, Low metallic Mn and Si
 B3 - Bonded, High metallic Mn and Si
 F1 - Fused, no metallic Mn and Si
 F2 - Fused, no metallic Mn and Si

In the study by Kotecki and Howden, the focus was on the hardness variation owing to a change in voltage. It was demonstrated that cracking occurred when the WM hardness was above 236 HV₁₀ (225 HB). No residual stress was measured in this study [29].

Summary of NACE SP0472-2010 requirements

NACE SP0472 limits the hardness of the WM and the BM to prevent SCC in H₂S. The hardness is limited to 210 HV₁₀ (200 HBN) for the WM and 248 HV₁₀ for the HAZ. One

of the following thermal methods applies to control the WM and HAZ hardnesses [8].

- Control of cooling time (Δt_{8-5}) between 800°C and 500°C.
- PWHT.
- Temper bead welding.

2.6 Test designs and aims

2.6.1 Tensile testing

Tensile testing is used to measure the strength and ductility of a weld or an all-WM test piece. The mechanical properties determined from a tensile test are tensile strength, yield strength, Young modulus (E), elongation, and reduction in area.

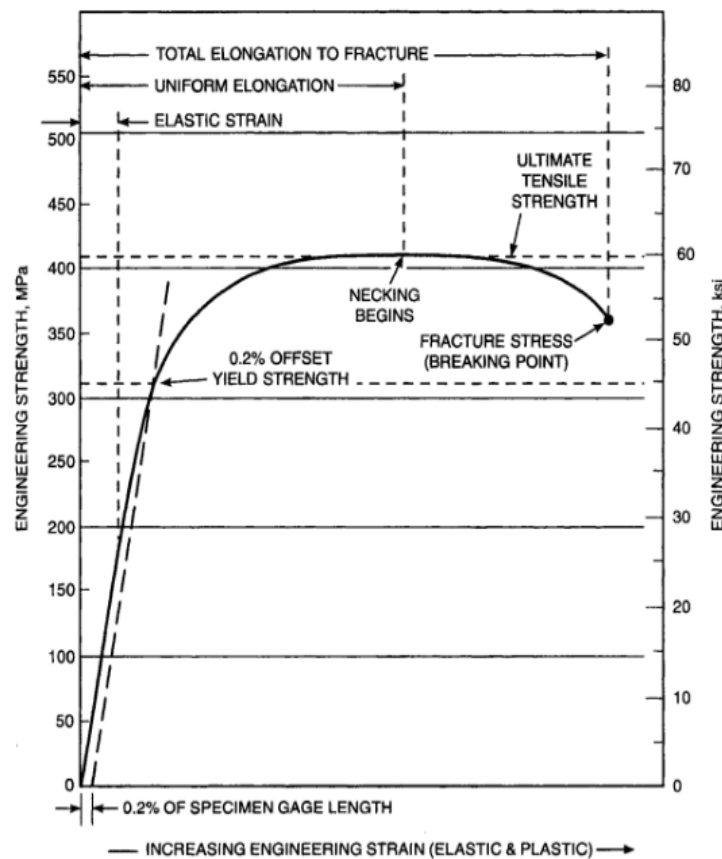


Figure 22: Illustration of a stress vs strain diagram. Various properties obtained from the tensile test can be established as well: tensile strength and yield strength [61]

In this study, transverse and all-weld tensile specimens were used. The transverse tensile test specimens were parallel to the rolling direction and all-weld specimens were perpendicular to the rolling direction [61].

2.6.2 Impact toughness

Impact tests are based on the energy. Samples are subjected to high rates of loading. Impact toughness is qualified at a certain test temperature, since material properties are temperature dependant. This is implemented to show where the ductile to brittle transition occurs [62]. Materials with high CIE have high impact energy, while brittle materials have a low CIE. In this study, the WM and HAZ CIE was tested separately using two full-size specimens, tested at an ambient temperature of 18°C to 20°C.

2.6.3 Hardness testing

Hardness testing is used to measure resistance to deformation. The basis of hardness testing is that a force is applied to a surface for a period of time. The dimension of the indent on the surface of the Brinell and Vickers test, are measured. These two techniques are widely used in the industry for hardness testing. Both these techniques are discussed in this study, since the absolute limits in NACE SP0472:2015 are provided in HBN and HV. Hardness correlates with ultimate tensile strength; as the hardness increases, the tensile strength will increase [63].

Brinell hardness testing

The Brinell hardness test employs a 10 mm ball under a known force to make an indentation on a flat smooth surface. The indentation diameter is measured and converted to hardness. The force is applied for 10 seconds. The standard load for the indentation is 500 kgf (for soft metals) or 3 000 kgf (for steel). The limit of Brinell hardness is 650 HB [64].

Vickers hardness testing

Smith and Sandland introduced the Vickers hardness test in 1925. They used a pyramid-shaped diamond to test the hardness of metals. The pyramid angle is fixed at 136° to give values similar to Brinell testing [64]. The diagonal dimension of the surface indentation is measured. The duration of the test can be changed, but according to NACE SP 0472-2015, it should be 10 seconds.

2.6.4 Selection of a corrosion test for this study

Two testing techniques, slow-strain-rate and immersion testing, were evaluated for testing SCC.

Slow-strain-rate testing

Slow-strain-rate testing SSRT is widely used for SCC [65]. The test is conducted by controlling the strain rate for a test piece. It employs a slow-strain-rate between 10^{-3} to 10^{-6} s^{-1} [66]. The strain rate can be controlled by means of an extensometer (ISO 7539). It is common that specimens do not fail under SSRT [66].

In a study by Beavers and Koch [65], the aim was to determine whether SSRT testing would yield useful data for predicting the SCC susceptibility of metals. The study concluded that it is important for the strain rate to be of the correct order. It was also noted that the strain obtained in a test simulation may differ from the strain induced in a working environment.

Advantages of the SSRT are that test results are quantitative and that the state of corrosion can be evaluated as it progressed in the study. A testing chamber will be necessary to simulate the corrosive environment. Since the surface stress will not be measured, alternative methods exist to perform either environmental assisted cracking or hydrogen embrittlement through step loading, as recommended by ASTM G129 for SSRT and ASTM F1624 for stepwise loading. These test methods also result in the relief of as-welded residual stress. These methods were therefore not given any consideration.

Difficulties with the slow-strain-rate technique related to the current project were that:

- No testing facility could implement SSRT in a corrosive environment.
- When samples are cut in any way, it will cause a relaxation of residual stress. It will be difficult to compare “simulated stress” with the residual stress.

Immersion testing

The welded samples are submerged in one batch in its uncut condition, leaving the residual stress in its welded state. The normal duration is 30 days under NACE TM1077-2005. The dimension of the testing cylinder will limit the number of samples. A disadvantage of the test by submersion is that the result only indicates “cracked” or “not cracked”.

Kotecki and Howden [29] used a similar test to evaluate SCC. In their study, residual stress was not measured. The test samples had no externally applied stress. The acting stress was internal residual stress owing to welding [29].

From the comparison of test designs, the testing by immersion is a better option:

- A similar test design was previously used for measuring the relationship of SCC and hardness [29].
- The as-welded residual stress interactions are of high importance in the test. Sectioning of the welded joint would cause a stress relief. Here, the complete welded sample can be evaluated.
- It is unnecessary to exert any external strain by mechanical testing or hardness testing.

The only disadvantage is that an inspection cannot be performed to establish crack progressions, as the result will either be “cracked” or “not cracked”.

2.6.5 Evaluation of cracks in the base metal and weld metal

Crack evaluation is performed according to NACE TM 0284 "Evaluation of Pipeline and Pressure Vessel Steel for Resistance to Hydrogen-Induced Cracking". Figure 23 indicates the crack evaluation.

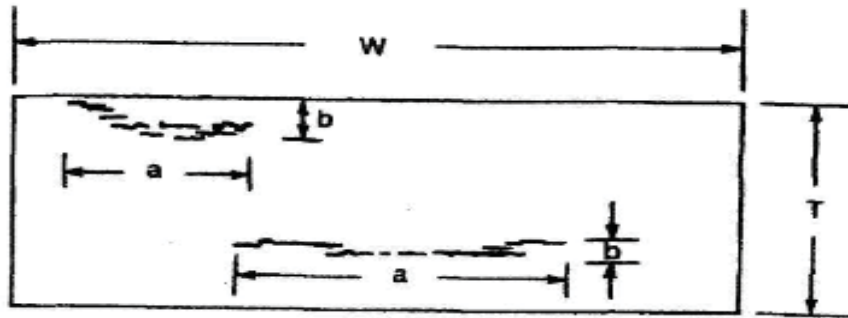


Figure 23: Crack lengths in specimens and measurement values [67]

Crack sensitivity ratio (CSR) (area):

$$CSR = \frac{\sum(a \times b)}{W \times T} \times 100 \%$$

Crack length ratio (CLR) (length):

$$CLR = \frac{\sum a}{W} \times 100 \%$$

Crack thickness ratio (CTR) (thickness):

$$CTR = \frac{\sum b}{W} \times 100 \%$$

Where:

a = crack length

b = crack thickness

W = section width

T = specimen thickness

The maximum acceptance criteria of allowed cracks in samples (as percentages) are stated to be CSR 15%, CLR 5% and CTR 2%.

3 EXPERIMENTAL EQUIPMENT AND METHODS

3.1 Sample planning

The sample was designed to be 300x300x16 mm after welding. This size was selected to obtain a large mesh for the residual stress measurements and to get the maximum number of samples from one plate. The mechanical test and ND measurements were performed on separate test samples to ensure that there was no stress relieving, owing to sectioning prior to the measure of residual stress. The material was used for the test samples in Table 14, manufactured from 40 plates, giving 20 pairs of 300x300x16mm.

Table 14: Number of tests to determine mechanical properties, residual stress and stress-corrosion cracking in specific locations

Test	Sample	E6013	E7018	E7018-PWHT	E8018	E9018	SA 516 Gr 70
Tensile	All-Weld	1	1	x	1	1	x
	Transverse	2	2	2	2	2	2
Impact toughness	Base Metal	x	x	x	X	x	2
	WM	2	2	2	2	2	x
	HAZ	2	2	2	2	2	x
Hardness HV ₁₀	Transverse	1	1	1	1	1	[1]
Residual stress measurements	3-dimensional	[2]	1	1	1	1	x
SCC	Full Sample	1	1	[3]	1	1	x

Note [1]: Hardness of BM was measured throughout the study.

Note [2]: The E6013 sample's residual stress was not measured, owing to the presence of a defect in the WM. A stress concentration in the WM owing to the defect will result in a change to the residual stress.

Note [3]: The E7018-PWHT was not tested for SCC, since there will be a reduction in residual stress and hardness not comparable with the other results.

3.2 Welding electrodes used in this study

As discussed in this study, the WM hardness was increased by increasing the minimum specified tensile strength of the electrode. An increment of 10 ksi was used to create various hardnesses. Standard electrode specifications are in ksi, e.g. E60XX

is a 60 ksi (415 MPa) strength electrode. Below, a short description is provided for each electrode used, while Table 15 provides the specified tensile strength and minimum yield strength of the electrodes. Table 16 indicates actual chemical compositions of electrodes used in the study. All electrodes used in the study conformed to ASME II C.

E6013

E6013 designates an all-purpose rutile-welding electrode. It has a minimum all-weld strength of 60 ksi (414 MPa). The flux contains rutile, cellulose, ferromanganese, potassium silicate as a binder and other siliceous materials. The slag is removed easily after welding. It is characterised as a low-penetrating arc. The impact strength of this rutile electrode is generally deficient [68].

E7018-1

This is an all-position low-hydrogen electrode. It is created with an inorganic covering that contains minimum moisture. It is used for low alloy-steels and carbon-manganese steels. It has an all-weld strength of 70 ksi (482 MPa). This is the standard welding electrode for welding pressure vessel steel and P-1 materials. The electrode covering contains a high percentage of iron powder [68].

E8018-B2

This is a basic-coated all-position low-hydrogen electrode. The nominal composition is 1.25% Cr and 0.5% Mo. This electrode is used where creep resistance is required. The all-weld strength is 80 ksi (552 MPa). The manufacturer specified that the electrode should be subjected to a PWHT at 690°C for one hour (AWS 5.5).

E9018-B3

This is a basic-coated all-position low-hydrogen electrode. It contains an addition of 2.25% Cr and 1% Mo. This electrode is used when creep resistance is required. The

all-weld strength is 90 ksi (621 MPa). It is specified by the manufacturer to be subjected to a PWHT at 690°C for one hour (AWS 5.5).

Table 15: The specified tensile strength and yield strength of the welding electrodes (ASME Section 2C 2013) and AWS 5.5

Electrode	Tensile strength (TS) [MPa]	Minimum yield strength (YS) [MPa]
6013	460-530	400
7018-1	510-570	420
8018-B2	550-650	460
9018-B3	630-720	530

Table 16: The actual chemical analysis of the E7018, E8018 and E9018 WM

Electrode	C	Mn	Si	P	S	Cr	Mo	Ni	Al	Cu	Nb	Ti
E7018	0.17	1.01	0.36	0.01	<0.01	0.13	0.00	0.02	0.03	0.16	<0.001	<0.001
E8018	0.10	0.84	0.43	0.01	0.01	1.02	0.42	0.01	<0.01	0.03	0.01	0.02
E9018	0.09	0.83	0.61	0.01	0.01	2.15	0.76	0.02	<0.01	0.02	0.02	0.02

3.3 Equipment and measuring techniques

Thermal camera and data logger

To verify preheat temperatures measured with the Flir T650 infrared camera, thermocouples were installed. The thermocouples used were of the B and K types. The methodology used to verify temperature were: the thermal camera was set up along thermocouples (2 x B-type, 2 x K-type), the B types were mounted on the boundary ± 2 mm from the V bevel, and the K types were mounted ± 5 mm from the V bevel.

Calibration of the various thermal emissivity on the plate

The emissivity of a steel surface depends on the surface condition. A ground surface has an emissivity of 0.55 to 0.61. For an oxidised surface, the emissivity is in the order of 0.85 [69]. Welded joints typically have a ground part and an oxidised part that cause divergent temperature values for emissivity. If the correct emissivity is not used, the temperature may be measured incorrectly.

The preheat temperature was measured with various temperature readings for the clean ground area and the oxidised metal (75 mm away from the weld area). The emissivity was adjusted for each zone since the temperature was known for the whole sample. After the adjustment, the temperature remained the same for the separate zones. In this project, an emissivity of 0.55 was used for a ground surface and 0.85 for an oxidised surface.

The data logger, a dataTaker DT80, was connected to the PC. This was alongside the thermal camera at points SP01 and SP02 (Figure 24). The sample plate was heated to 75°C for the preheat temperature. The temperature was measured and the results are shown in Table 17. The readings of the thermocouple and thermal camera differ by less than 1.5°C.

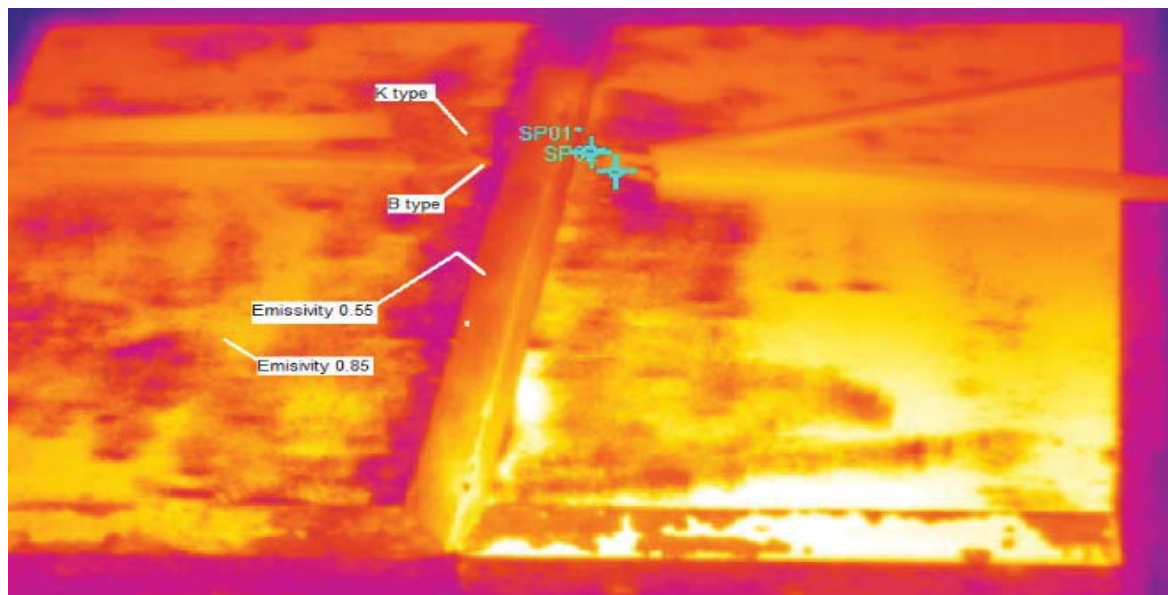


Figure 24: The setup of thermocouples along the thermal camera at measuring points SP01 and SP02. SP01 was close to the B-Type thermocouples, while SP02 was close to the K-type thermocouples. The clean ground areas emissivity was 0.55 and the oxidised part was 0.85

Table 17: Data verification between the thermal camera and the thermal couples

Measuring Technique	Measuring Point	Temperature [°C]	Distance from center [mm]	Emissivity of area (ϵ)
Thermal camera	SP01	74	2	0.55
Thermocouples	B-Type	75	2	[-]
Thermal Camera	SP02	74	5	0.55
Thermocouples	K-Type	75	5	[-]
Preheat Temperature	[-]	75	[-]	[-]

3.4 Sample manufacturing and weld setup

3.4.1 Preparation for welding

Samples were ground with a rough grit of 80 to remove all the rust. This was for a strip of about 75 mm next to the machined weld preparation in the general welding area and the root of plates. The plates were aligned, tacked into position and heated to the preheat temperature. Welding was then performed with the various electrodes.

3.4.2 Fixing of clamps

After some of the first plates were welded with E6013 electrodes, two clamps did not prevent distortion. The next set of E6013 plates were heavily clamped on the one side onto a thick baseplate with dimensions 400x400x32 mm. The right-hand side was tacked on the side in the longitudinal direction. The plates were also tack welded transversally. The plates were completely restricted in the X and Y directions, to ensure that there would be minimum distortion resulting in a maximum residual stress. The thick black lines in Figure 25 indicate tack welds.

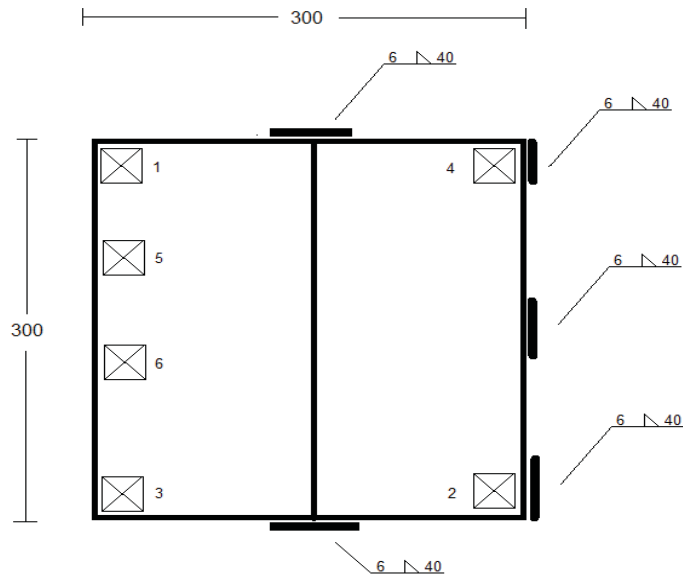


Figure 25: The left-hand side with four clamps and the right-hand side with two clamps and tack welds. The dark lines indicate where the plate was tack welded to a 32 mm thick base plate

After the welding was completed, the left-hand clamps were loosened. Subsequently, a grinder with a cutting disc was used to remove the tack welds. The remaining clamp was then loosened, and the tack welds were removed by grinding.

3.4.3 Welding power supply

The welding was performed with a standard constant-current SMAW welding unit, welding DCEP.

3.4.4 Run-on and off tabs

An initial problem during welding was arc-blow (Figure 26). The solution to this problem was to manufacture and add run-on and off tabs. This ensured that the arc-blow occurred on the run-on tab and by the time the arc got to the sample plate, the arc was stable. Without this measure, the integrity of the welded samples was compromised for the first and last 50 mm. An example of a run-on tab is illustrated in Figure 27.

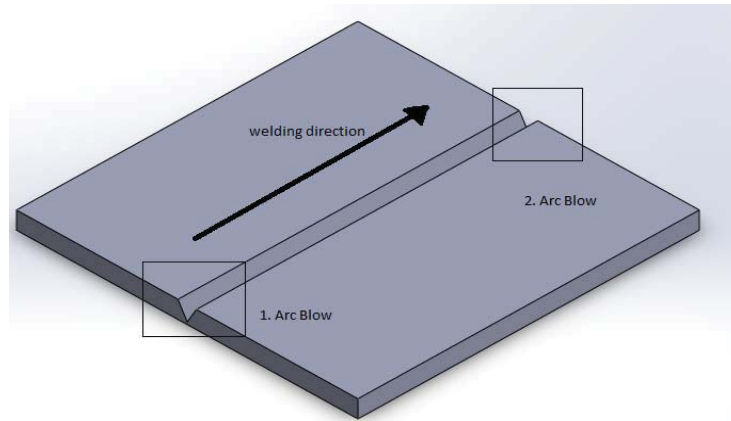


Figure 26: The regions where arc-blow occurred during welding. The problem was solved by adding run-on and off plates. The arc-blow compromised the integrity of the first and last 50 mm on each of the welds

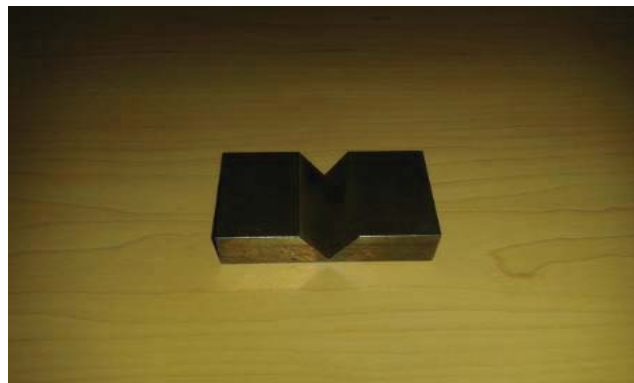


Figure 27: The run-on and off plate with dimension 60x16x40 mm

3.4.5 Heat input

HI values were calculated for the test welds in Table 18 to Table 21. This was using the following two formulas, indicating Method A and Method B (BS EN 1011-1:2000). The HI for Method A and B was plotted in Figure 29 to Figure 32.

Method A:

$$HI = \frac{d^2LF}{ROL}$$

Where:

d = thickness of electrode;

L = consumed length - the stub length;

F = deposition efficiency

ROL = distance welded in mm

The deposition efficiency was <90% for electrodes E6013, E8018 and E9019, thus a factor F=0.0368 was used. The E7018 deposition efficiency was <110%, thus a factor of F=0.0408 was used [24].

The results for Method B is illustrated below:

$$HI = \frac{\eta VI}{v}$$

Where:

η = Efficiency 0.8 [24]

V = Volts

I = Welding Current

v = speed [mm/min]

The complete WPS and pass sequence is illustrated in Appendix A.

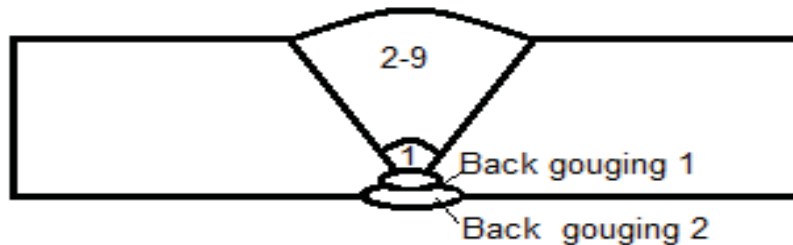


Figure 28: Single-V prep with weld sequence used for the manufacturing of the welds

Table 18: The HI calculated for the E6013 by Methods A and B. In the table, electrodes size, amps and travel speed are included

Weld Side		Weld side 1								Weld side 2	
E6013	Symbol	Run 1	Run 2	Run 3	Run 4	Run 5	Run 6	Run 7	Run 8	Run 1	Run 2
Efficiency	F	0.0368	0.0368	0.0368	0.0368	0.0368	0.0368	0.0368	0.0368	0.0368	0.0368
electrode size	d	2.15	3.2	3.2	3.2	3.2	3.2	3.2	3.2	3.2	3.2
consumed length	L	300	290	300	310	240	305	320	280	290	150
Run out length	ROL	129	191	244	207	162	175	190	230	190	101
Heat Input (method A)	HI[A]	0.40	0.57	0.46	0.56	0.56	0.66	0.63	0.46	0.58	0.56
Volts [MAX]	V	14.0	21.0	21.0	21.0	21.0	21.0	21.0	21.0	21.0	21.0
Volts [MIN]	V	12.0	16.0	16.0	16.0	16.0	16.0	16.0	16.0	16.0	16.0
Amps	A	120	123	126	126	126	126	126	126	126	126
Travel speed	v [mm/min]	230	203	207	198	184	194	175	250	184	276
Heat Input [MAX]	HI_MAX[B]	0.35	0.61	0.61	0.64	0.69	0.65	0.73	0.51	0.69	0.46
Heat Input [MIN]	HI_MIN[B]	0.30	0.47	0.47	0.49	0.53	0.50	0.55	0.39	0.53	0.35
Average	HI[B]	0.33	0.54	0.54	0.57	0.61	0.58	0.64	0.45	0.61	0.41

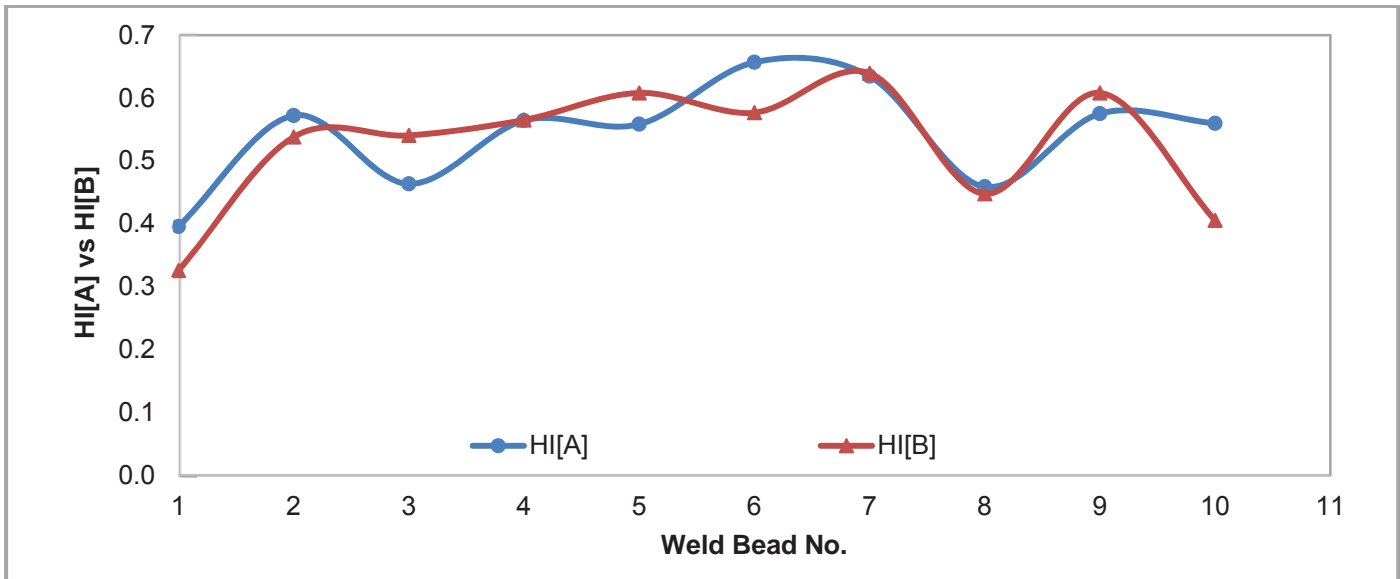


Figure 29: The E6013 HI A vs HI B in kJ/mm for each weld deposit

Table 19: The HI calculated for the E7018 by Methods A and B. In the table, electrodes size, amps and travel speed are included

Weld Side		Weld Side 1								Weld Side 2	
E7018	Symbol	Run 1	Run 2	Run 3	Run 4	Run 5	Run 6	Run 7	Run 1	Run 2	
Efficiency	F	0.048	0.048	0.048	0.048	0.048	0.048	0.048	0.048	0.048	
electrode size	d	3.15	3.15	4	4	4	4	4	3.15	4	
consumed length	L	300	320	300	290	300	290	290	300	320	
Run out length	ROL	150	150	200	213	300	300	250	200	320	
Heat Input	HI[A]	0.95	1.02	1.15	1.05	0.77	0.74	0.89	0.71	0.77	
Volts [MAX]	V	24.0	24.0	23.6	23.6	23.6	23.6	23.6	24.0	23.6	
Volts [MIN]	V	19.8	19.8	19.0	19.0	19.0	19.0	19.0	19.0	21.0	
Amps	A	123	126	165	165	165	165	165	123	165	
Travel speed	v [mm/min]	224	220	304	272	376	408	344	348	360	
Heat Input [MAX]	HI_MAX[B]	0.63	0.66	0.61	0.69	0.50	0.46	0.54	0.41	0.52	
Heat Input [MIN]	HI_MIN[B]	0.5	0.5	0.5	0.6	0.4	0.4	0.4	0.3	0.5	
Average	HI[B]	0.577	0.602	0.555	0.620	0.449	0.413	0.490	0.365	0.491	

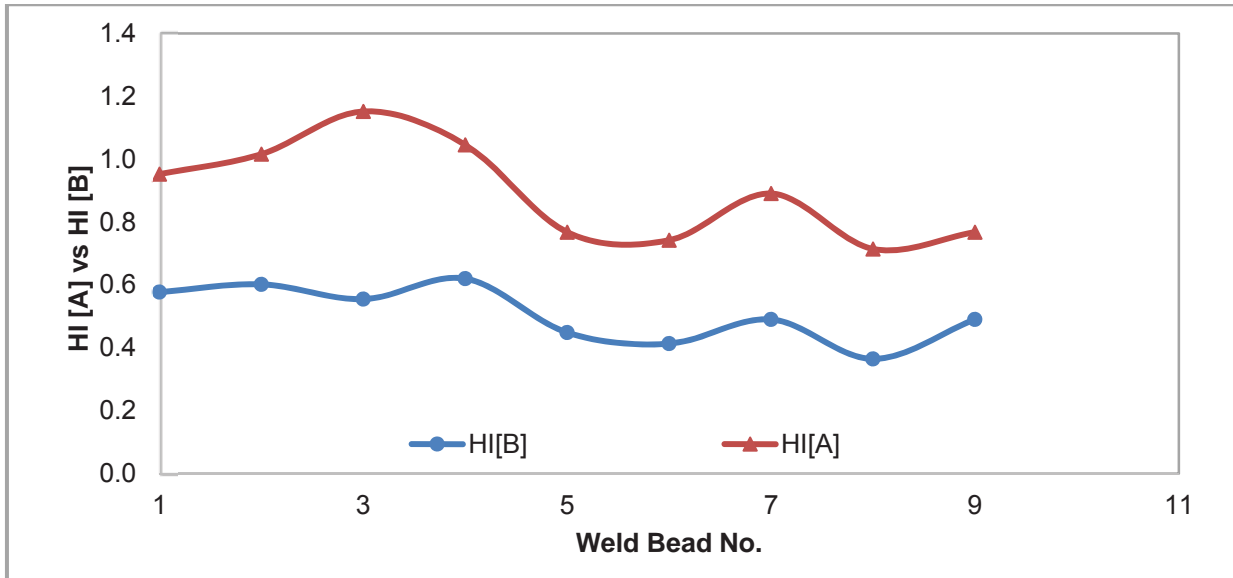


Figure 30: The E7018 HI A vs HI B in kJ/mm for each weld deposit

Table 20: The HI for the E8018 by Methods A and B. In the table, the electrode size, amps and welding speed are provided

Weld Side		Weld side 1						Weld side 2	
E8018	Symbol	Run 1	Run 2	Run 3	Run 4	Run 5	Run 6	Run 1	Run 2
Efficiency	F	0.0368	0.0368	0.0368	0.0368	0.0368	0.0368	0.0368	0.0368
electrode size	d	3.15	4	4	4	4	4	3.15	4
consumed length	L	310	310	320	310	300	300	330	300
Run out length	ROL	112	154	100	230	150	128	300	150
Heat Input (method A)	HI[A]	1.01	1.19	1.88	0.79	1.18	1.38	0.40	1.18
Volts [MAX]	V	24	27	27	27	27	27	24	27
Volts [MIN]	V	19	21	21	21	21	21	19	21
Amps	A	123	160	165	165	165	165	123	165
Travel speed	v [mm/min]	217	216	180	227	220	167	313	220
Heat Input [MAX]	HI_MAX[B]	0.65	0.96	1.19	0.94	0.97	1.28	0.45	0.97
Heat Input [MIN]	HI_MIN[B]	0.52	0.75	0.92	0.73	0.76	1.00	0.36	0.76
Average	HI[B]	0.58	0.85	1.06	0.84	0.86	1.14	0.41	0.86

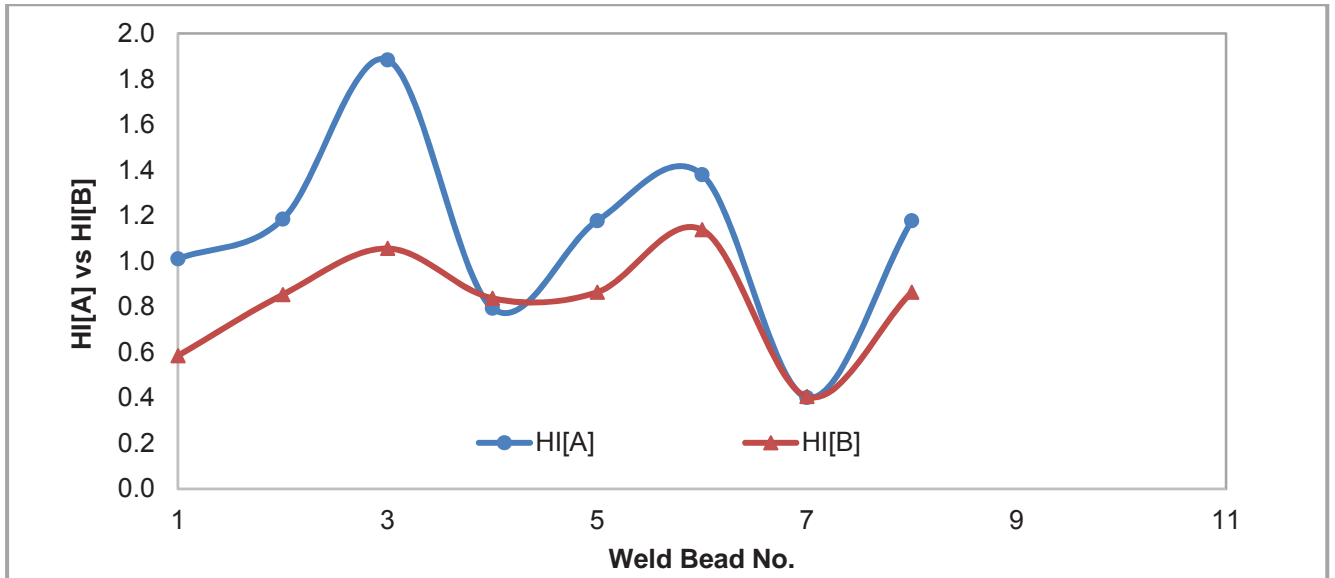


Figure 31: The E8018 HI A vs HI B in kJ/mm for each weld deposit

Table 21: The HI for the E9018 by Methods A and B. The electrode size, amps and welding speed are provided

Weld Side		Weld side 1									Weld side 2	
E9018	Symbol	Run 1	Run 2	Run 3	Run 4	Run 5	Run 6	Run 7	Run 8	Run 9	Run 1	Run 2
Efficiency	F	0.0368	0.0368	0.0368	0.0368	0.0368	0.0368	0.0368	0.0368	0.0368	0.0368	0.0368
electrode size	d	3.15	3.15	4	4	4	4	4	4	4	3.15	4
consumed length	L	300	280	280	300	280	280	280	330	300	320	330
Run out length	ROL	150	130	200	160	290	290	290	320	275	270	170
Heat Input (method A)	HI[A]	0.73	0.79	0.82	1.10	0.57	0.57	0.57	0.61	0.64	0.43	1.14
Volts [MAX]	V	24.0	23.5	23.5	23.5	23.5	23.5	23.5	23.5	23.5	24.0	25.0
Volts [MIN]	V	19.0	21.0	21.0	21.0	21.0	21.0	21.0	21.0	21.0	19.0	21.0
Amps	A	123	126	165	165	165	165	165	165	165	123	165
Travel speed	v [mm/min]	164	210	300	224	420	288	448	384	370	140	300
Heat Input [MAX]	HI_MAX[B]	0.86	0.68	0.62	0.83	0.44	0.65	0.42	0.48	0.50	1.01	0.66
Heat Input [MIN]	HI_MIN[B]	0.68	0.60	0.55	0.74	0.40	0.58	0.37	0.43	0.45	0.80	0.55
Average	HI[B]	0.77	0.64	0.59	0.79	0.42	0.61	0.39	0.46	0.48	0.91	0.61

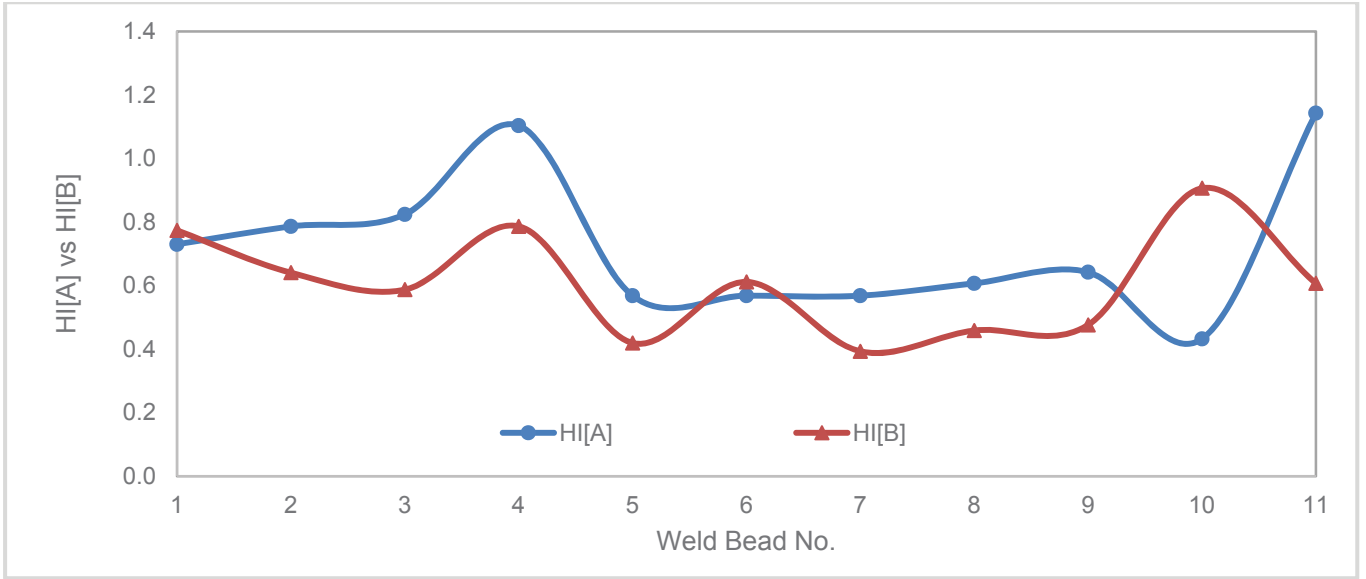


Figure 32: HI[A] vs HI[B] in kJ/mm for each weld deposit; it deviated from the ideal line

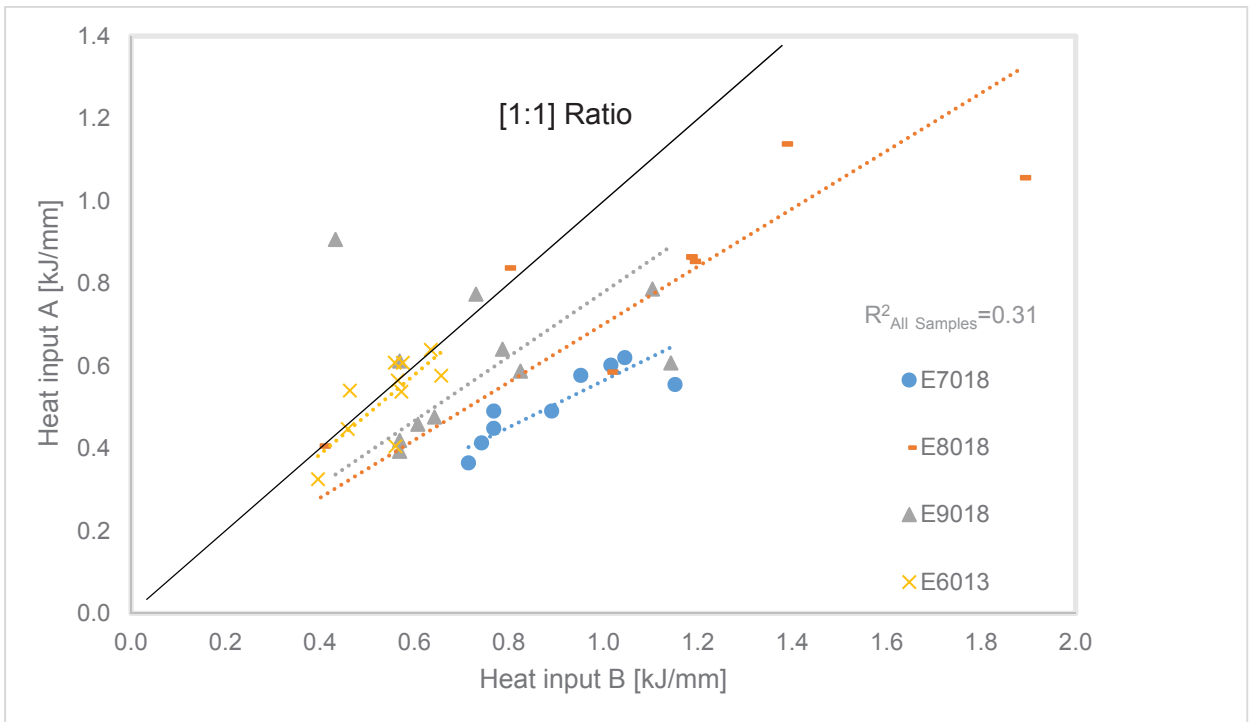


Figure 33: The HI, as calculated using Method A and Method B in kJ/mm for each weld deposit on series E6013, E7018, E8018 and E9018 with the error of each data series

Table 22: Average HI calculated for each series according to Method A and Method B and the average of the two methods

HI	E6013	E7018	E8018	E9018
Average Method A	0.54	0.89	1.13	0.73
Average Method B	0.53	0.51	0.83	0.61
Average of the A and B	0.54	0.70	0.98	0.67

From the recorded HI values, there were large differences between the two methods. It was observed that the E6013 HI was the closest to the one-to-one ratio. Although it was difficult to correlate the other results, it did not influence conclusions from the study, as the HI was not used to predict metallurgical properties or expected results in this dissertation. The effect of the average HI on mechanical properties will be evaluated in Sections 4 and 5.

3.4.6 Post-weld heat treatment

The sample plate E7018-PWHT in its original size was trimmed to fit in the heat-treating furnace. The plate was cut from 300x300x16 mm to 300x290x16 mm (indicated in Figure 34 with a dark line). It seemed reasonable to assume that the removal of material at the side did not affect the residual stresses on the weld joint. The PWHT was at 600°C for two hours to ensure maximum stress relief [70], [71]. Before the sample was heat-treated, a control cycle without a sample was and measured with a thermocouple to ensure the heating and cooling rate and soak temperatures were within specification.

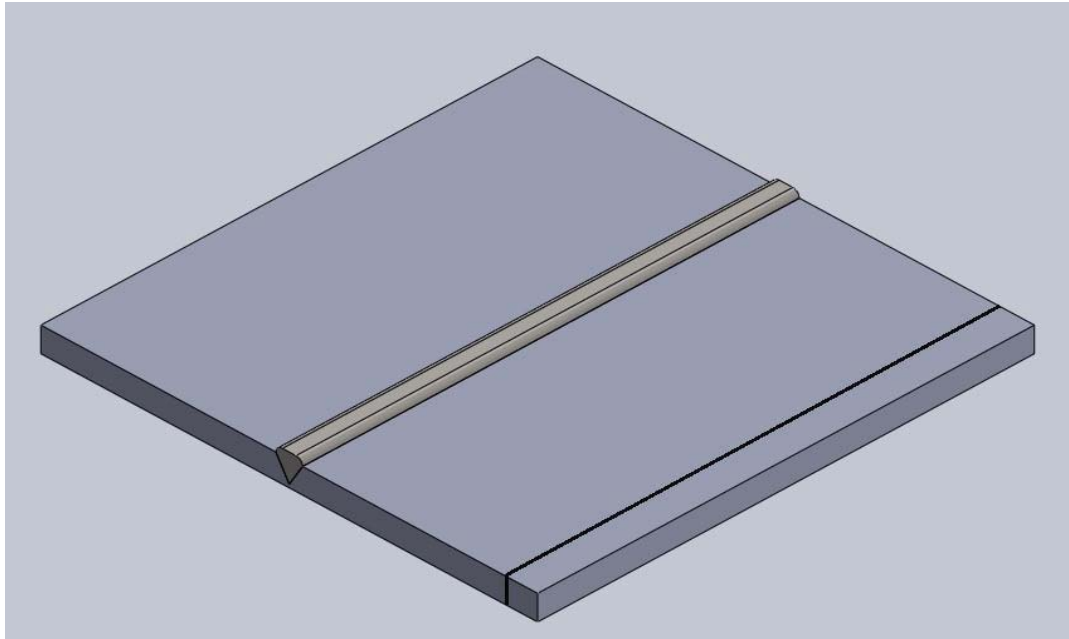


Figure 34: The plate with the edge trimmed. The sample was cut before the PWHT was performed. The final dimensions was 300x290x16 mm

3.5 Characterisation of welded joints

3.5.1 Tensile testing

The tensile test pieces were machined as round specimens to ASTM A370; both were all-weld and transverse-weld test pieces. Specimen sizes are stipulated in Figure 35.

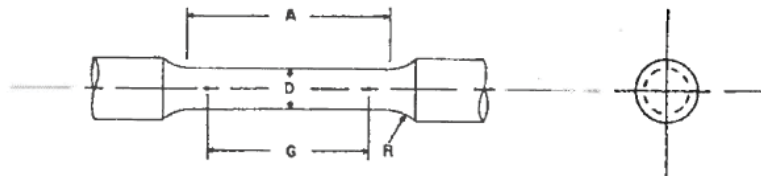


Figure 35: Tensile specimen dimensions used in test [72]

Table 23: Tensile specimen dimensions used in this study [in mm]

Nominal diameter (D)	12.5
Gauge Length (G)	50
Radius, min (R)	10
Length Reduced section(A)	60

3.5.2 Impact testing

Standard Charpy test samples were used. The Charpy test specimens are illustrated in Figure 36. ASTM E23 was used when designing the sample specimens. The dimensions after machining were 55x10x10 mm. The following tests were accomplished:

- Impact testing in the root of the weld (Figure 36).
- Impact testing in the HAZ.

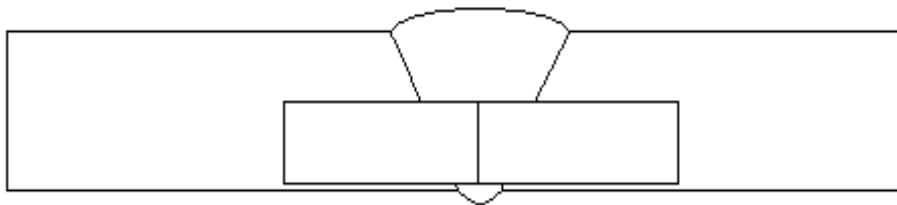


Figure 36: Orientation of Charpy impact strength specimen machined from each sample plate. The vertical line denotes the notch

The samples were cut using a band cooled by cutting fluid. The samples were polished and etched to verify where the root and the HAZs were situated. The impact samples were orientated in the L-T direction as specified in various specifications, as the L-T orientation usually results in the lowest impact strength [73].

3.5.3 Hardness testing

The sections for hardness testing were cut into smaller workable sections. The first cuts were on a fluid-cooled band. The cut sections were 15x300x16mm. The remainder of the cutting was with a water-cooled disc grinder. The samples were then prepared by the method described in Section 3.5.4.

Hardness measuring was with a Vickers Future-tech FV 700e with a 10 kg load. In this study, hardness was measured close to the surface, the middle and the root of the weld. This defined the hardness throughout the whole welding profile according to ISO 15156 [74] (Figure 37).



Figure 37: Indentations at the top, middle and bottom of the weld. The transverse indent spacing was 0.5 mm

3.5.4 Metallography

The original sample plates were cut by a water-cooled band into a workable size of 30x300x16 mm sections transversely across the weld. Metallography was according to standard practices. A 2% Nital solution was manufactured and the sample surface was submerged for 15 seconds.

3.5.5 d-zero and neutron diffraction measurements

As mentioned in Section 2.3.2, it is important that the d-zero value is as close as possible to its stress-free state. There are a few options in creating a d-zero value or as close as possible to the stress-free state, according to ISO/TS 21432:2010 (ISO 21432:2010):

- Using a powder representative of the sample measured.
- Using a stress-free part of the sample where stress was negligible (the start or end of a welded sample) (Far field approach).
- Measuring the lattice parameters at “zero stress”, perpendicular to a stress-free surface.

The first option was not considered for this project since the equipment to obtain the powder or to make a powder was not available. The last two options were combined to measure the d-zero reference discs (Figure 38). The reference disc was cut at the end of the plate where the stress is negligible. The d-zero values were measured at the surface $\sigma_L=0$ where the longitudinal stress was completely relieved. This means that the strain for the ϵ_L is known in the stress-free condition. This known strain can

then be used for the other two directional calculations of the stress. It can be assumed that the stress-free strain parameter will be the same in all three directions.

The reference slice, a part where stress is negligible, was cut and measured according to ISO/TS 21432:2010 by the Southern African Nuclear Energy Corporation (Nesca). The ND measurements were at Nesca's Safari-1 reactor. The gauge volume of 3x3x3 mm was used for the iron $d_{2,1,1}$ crystal lattice.

Calculation of strain ϵ by d-zero condition

The following steps were implemented to calculate the strain as discussed in Section 2.3.2:

- The $d_{2,1,1}$ (d-value) was measured by ND of the entire sample 300x300x16 mm on positions such as Figure 38.
- The d_{hkl} -zero reference slice with dimensions 100x3x16 mm, in its stress relieved condition, was measured by ND. Note that where the sample is taken from, it is known that the stress is negligible.
- The correction was applied to calculate the strain.

The process used in cutting the d-zero value was a water jet cutter. This is a heat-free process, critical for the prevention of the formation of new stresses. This process ensured there was no change in the residual stress state (ISO 21432:2010).

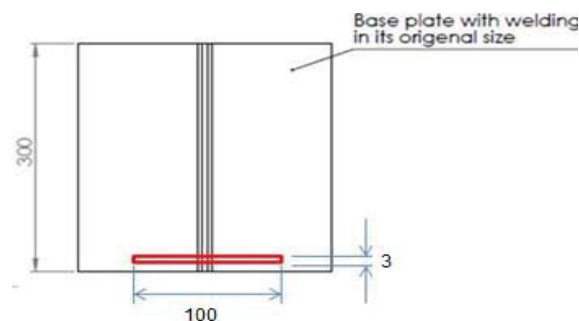


Figure 38: The d-zero reference slices, with dimensions 100x3x16 mm was taken at the end of the plate where the residual stress was negligible. This was for each sample series to calculate an accurate d-zero value

An example of a strain calculation can be established below; this was at a depth of 2.1mm. The weld centreline was 0 mm in the longitudinal direction.

$$\begin{aligned}\varepsilon_{hkl} &= \frac{d_{hkl} - d_{hkl}^0}{d_{hkl}^0} \\ &= \frac{1.180010052 - 1.177525767}{1.177525767} \times 10^{-6} \\ &= 2.11 \times 10^{-3} \\ &= 0.000211 \text{ Microstrain}\end{aligned}$$



Figure 39: The residual strain measurements at various depths of 2.1, 5.2, 8.31, 11.45 and 14.52mm. The dimensions of the gauge volume are 3x3x3 mm

3.5.6 Testing for stress-corrosion cracking

Table 24 indicates the actual measured NACE TM1077-2005 test solution during the SCC testing.

Table 24: Actual test parameters used in the corrosion test, according to NACE TM0177

Total Surface Area	353.65 cm ²
Degreasing Solution	Degreased in trichloroethylene and rinsed with acetone
Volume	10 litres
Temperature	25±3°C
pH	Initial: 2.70 After 1 h H ₂ S saturation: 3.21 After 96 h test period: 3.15
Test period	one hour saturation + 720 hours (30 days)
Inspection interval	1
Gas flow rate	Nitrogen purge: 100 ml/min/ litre for one hour H ₂ S saturation 200 ml/min/ litre of solution for one hour H ₂ S test: positive pressure maintained

The full welded plate with dimensions 300x300x16 mm was submerged into the testing solution (Table 24) with no sectioning (Figure 41). Samples were placed in one batch with a 10 mm spacing on the edges between each plate. The system was purged with nitrogen gas for one hour with a flow rate of 1l/min. Thereafter, the solution was saturated with hydrogen sulphide for one hour with a flow rate of 2l/min.

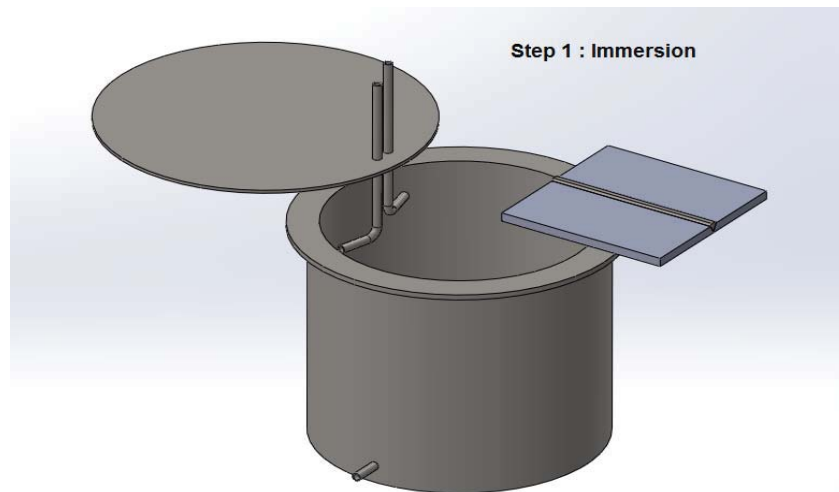


Figure 40: The sample plates were submerged in NACE TM 0177 solution with no cutting to the plates

After 30 days of SCC exposure, the test specimens were sectioned from the centre of the plate by water jet (Step 2 in Figure 41). From the literature discussed of residual stress, the highest stress was in the middle of the plate [4] and it was confirmed with ND stress measurements during this study. It can therefore be assumed that if cracking does not occur in the middle, where the largest stress is present, the sample will be defect-free.

The section was taken transversely across the welded area on section AA. The visual inspection was on the section with magnification of 50x, 100x, 200x and 500x. The minimum requirement of NACE TM 0177 is a visual inspection at 10x magnification to determine if cracking occurred [9]. The rest of the sample was tested with a magnetic particle inspection on the exposed surfaces to prove if SCC initiated on the surface.

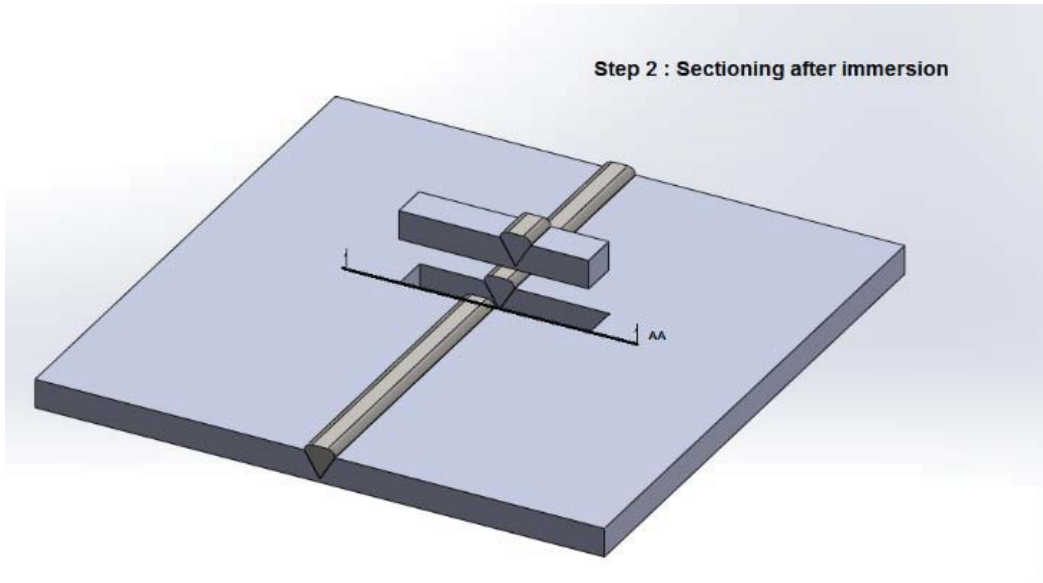


Figure 41: A cross section AA that indicates where the sectioning was made of the samples in the middle of the plate after it was exposed to the test solution. The largest stress is in the middle of the sample on AA; this is the specimen inspected. The dimensions of the sample are 16x100x20 mm

4 RESULTS

4.1 Tensile testing

The tensile strength, yield strength, elongation and failure location of the four separate welding electrodes are reported in Table 25. This included the SA 516 Gr 70 and the E7018-PWHT condition. Appendix B contains stress strain diagrams.

Table 25: The transverse yield strength, tensile strength and elongation for the various electrodes used and the BM properties (SAIW Report B031 & C046)

Sample	Transverse yield strength [MPa]	Transverse tensile strength [MPa]	Elongation [%]	Failure location
SA 516 Gr 70 ¹	350	490	16	BM
SA 516 Gr 70 ¹	350	490	16	BM
E6013	357	501	6	WM(defect) ²
E6013	345	408	7	WM(defect) ²
E7018	360	511	12	BM
E7018	360	511	11	BM
E7018-PWHT	345	495	14	WM
E7018-PWHT	345	499	16	WM
E8018	380	515	12	BM
E8018	382	517	12	BM
E9018	372	516	11	BM
E9018	368	515	12	BM

Note 1: The SA 516 Gr 70 refers to all BM test coupons.

Note 2: WM defect, slag inclusions.

BM - Base Metal

WM - Weld Metal

Observations on the transverse tensile test results

- Both the E6013 samples failed in the WM, with slag inclusion visible on the fracture surfaces.
- The E7018-PWHT failed in the WM.
- For all other samples, failure occurred in the BM and thus the transverse tensile and yield strength was defined by the base material properties.

The mechanical properties of the all-weld specimens of the four separate electrodes is illustrated in Table 26. The all-weld yield and tensile strength are stated, with the

specified minimum tensile strength according to the manufacturer. It can be stated as well that the actual tensile strength exceeds the minimum specified values.

Table 26: The mechanical properties of the all-weld samples' tensile strength, yield strength and elongation [22]. Only one of each sample was tested

Sample	Actual yield strength [MPa]	Actual tensile strength [MPa]	Specified tensile strength[MPa]	Elongation [%]
E6013	443	512	460-530	20.0
E7018	503	587	510-570	26.6
E8018**	491	624	550-650	27.3
E9018**	659	829	630-720	20.4

** No PWHT was performed; the specified tensile strength is in the PWHT condition.

Observations on the all weld tensile test results

- The actual strength of E7018 was outside the specified range.
- The E9018 tensile strength was higher than the specified minimum/maximum tensile strength.
- The E8018 yield strength was slightly lower than the E7018, but the tensile strength was higher.

4.2 Impact testing

The Charpy impact energy for the various WMs and HAZs are reported in Table 27. In the E7018 and E9018 impact strength test, an extra sample was tested if the difference between the lowest and the highest recorded impact strength was over 40 joules. The average for the samples is included. During testing, the ambient temperature was between 18°C and 20°C.

Table 27: Impact toughness in the WM and HAZ of the SA 516 Gr 70, E6013, E7018, E7018-PWHT, E8018 and E9018. The test temperature was 18 to 20°C

	Sample [J]				
	Location	1	2	3	Average [J]
SA 516 Gr 70		217	226	224	222
E6013	WM	47	47	-	47
	HAZ	66	60	-	63
E7018	WM	329	286	356	324
	HAZ	203	263	-	233
E7018- PWHT	WM	250	250	-	250
	HAZ	237	247	-	242
E8018	WM	224	198	-	211
	HAZ	229	200	-	215
E9018	WM	290	88	235	263
	HAZ	326	160	-	243

Observations

- The impact strength of the E6013 WM is extremely low. The minimum according to the manufacturer is 70 J.
- The E6013 HAZ's impact strength is higher than the E6013 WM (WM average impact strength 47 J; HAZ, 63 J).
- The E7018 WM impact strength is superior to others.
- The E7018-PWHT impact strength is lower than the E7018 in the WM (342 J vs 250 J).

4.3 Hardness testing

Figure 42 indicates that the hardness plot with the hardness profile for the top, middle and bottom section of the E6013 weld can be observed. The indents were spaced 0.5 mm apart.

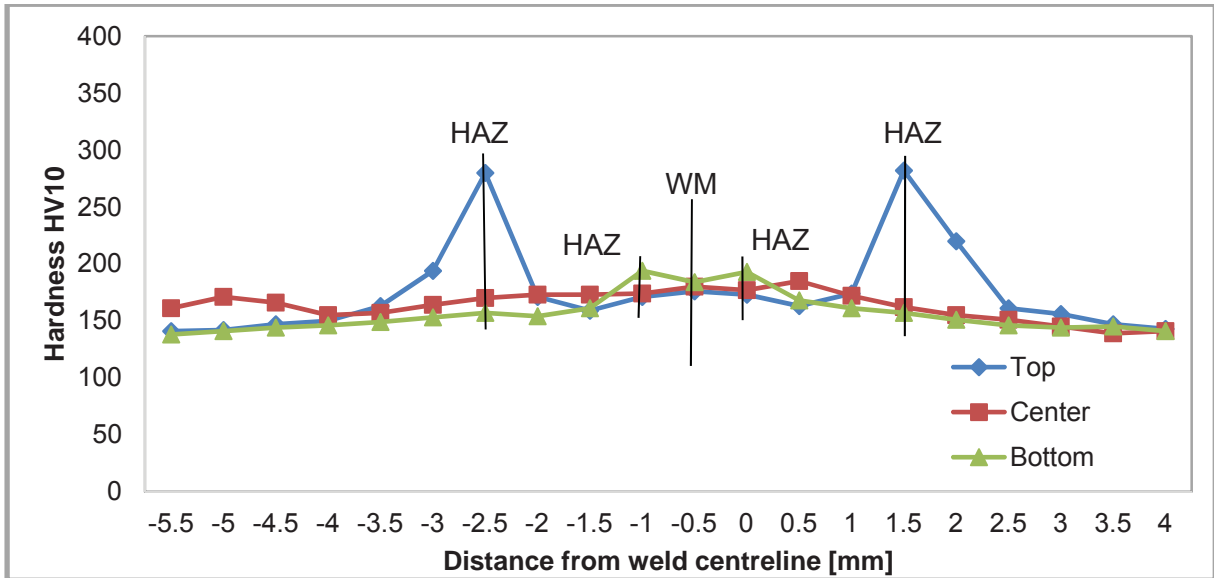


Figure 42: Transverse hardness was HV₁₀ of the E6013 welded sample of the WM, HAZ and BM. It is represented for the top, middle and bottom of the weld

Figure 43 indicates the hardness plot of the top surface, middle and bottom for the welded joint fabricated, using the E7018 electrode.

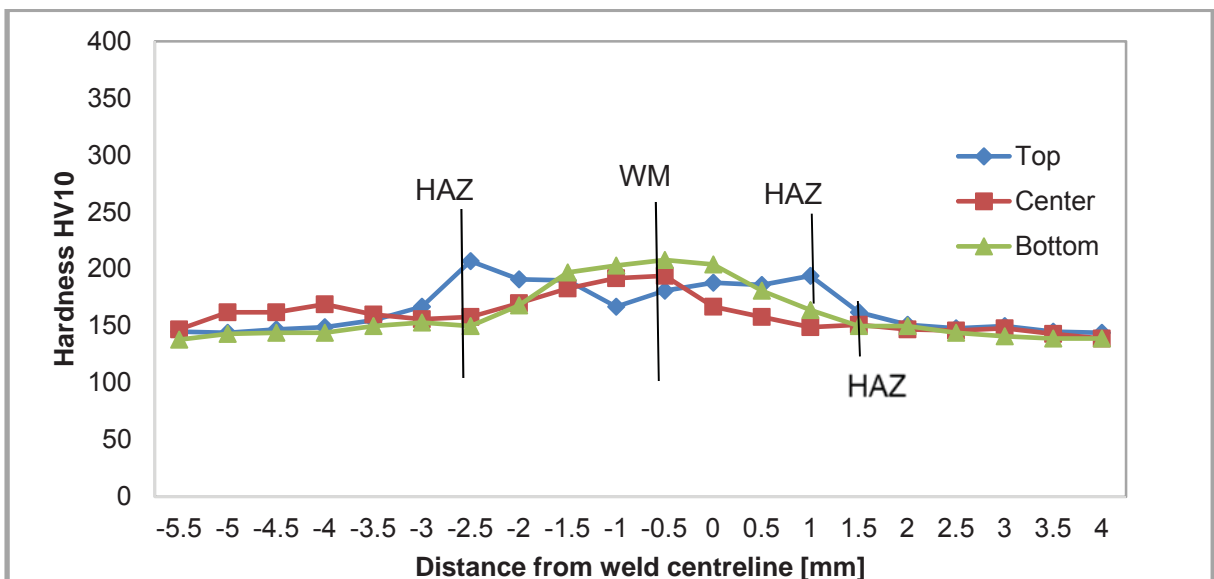


Figure 43: Transverse hardness was HV₁₀ of the E7018 welded sample of the WM, HAZ and BM

Figure 44 indicates the hardness of HV₁₀ profile for the top, middle and bottom section of the E8018 electrode.

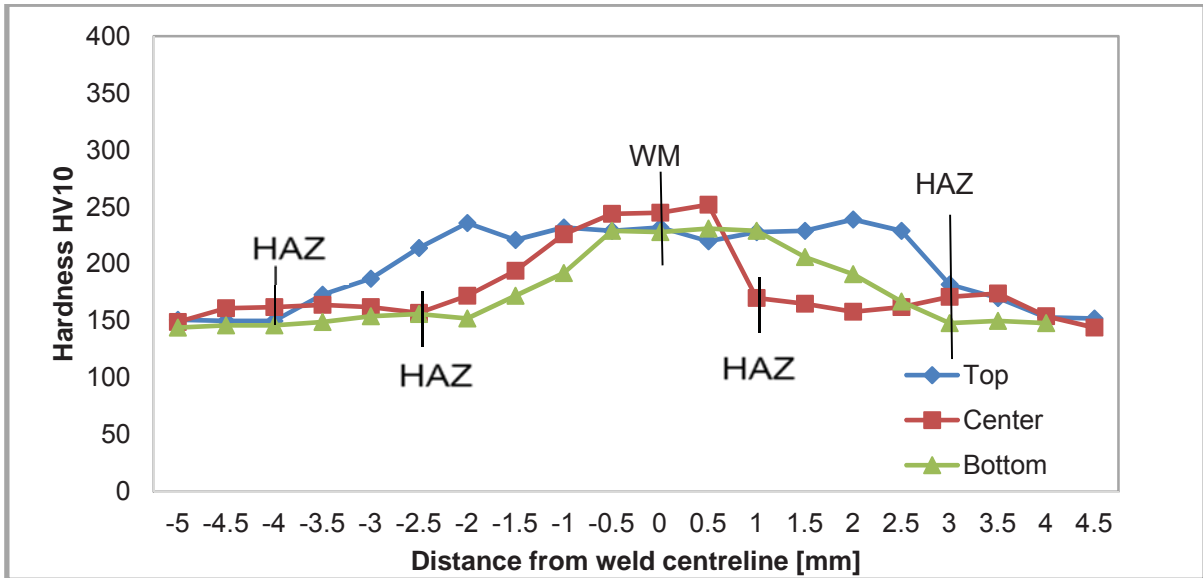


Figure 44: Transverse hardness was HV₁₀ of the E8018 welded sample of the WM, HAZ and BM

Figure 45 indicates the hardness of HV₁₀ for the top, middle and bottom section of the E9018 weld.

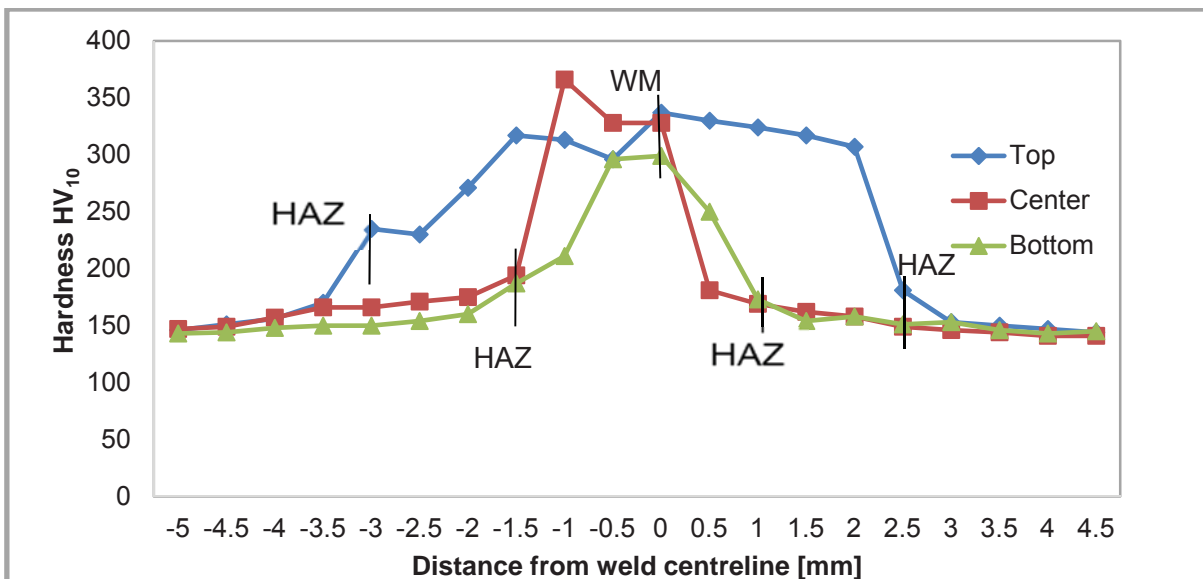


Figure 45: Transverse hardness was HV₁₀ of E9018 welded sample of the WM, HAZ and BM

Figure 46-Figure 48 is a comparison of the top, middle and bottom hardness respectively for the various samples.

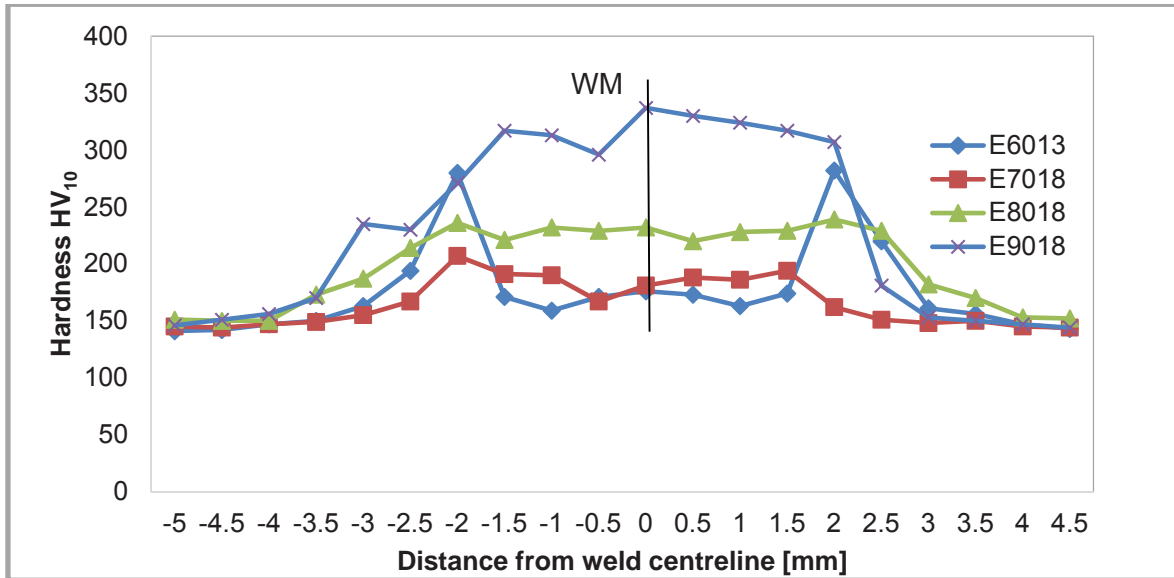


Figure 46: Sample comparison of the top hardness HV₁₀ for the various test samples. There is high hardness in the HAZ of the E6013 electrode. This exceeds the limit of 250 HV₁₀ in the HAZ. In the WM, a constant hardness increase can be observed

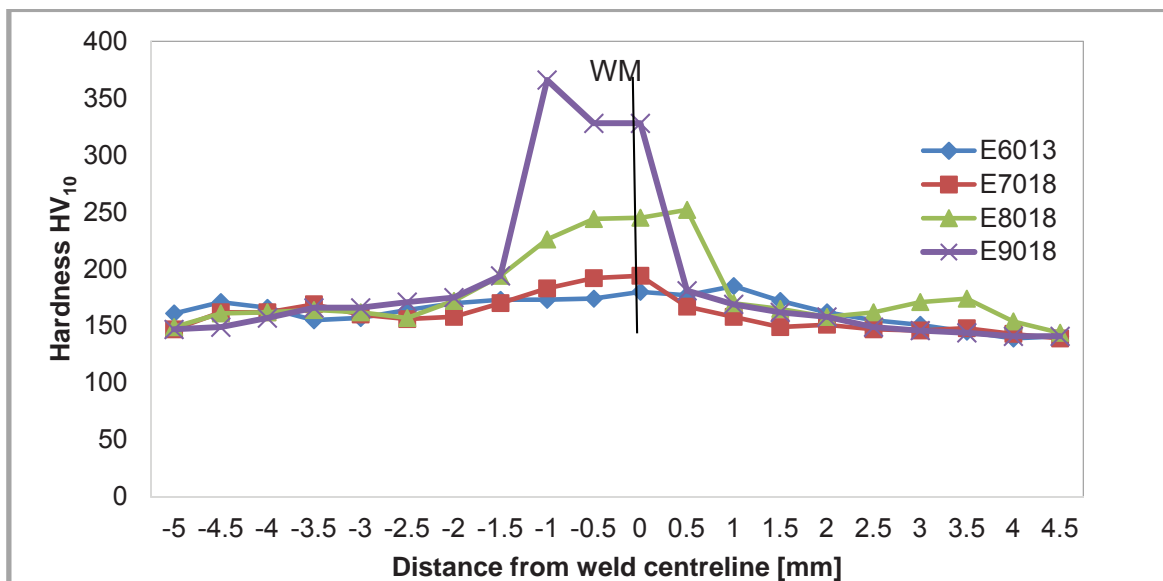


Figure 47: Sample comparison of middle hardness HV₁₀. The increase in hardness can be illustrated for each welding electrode

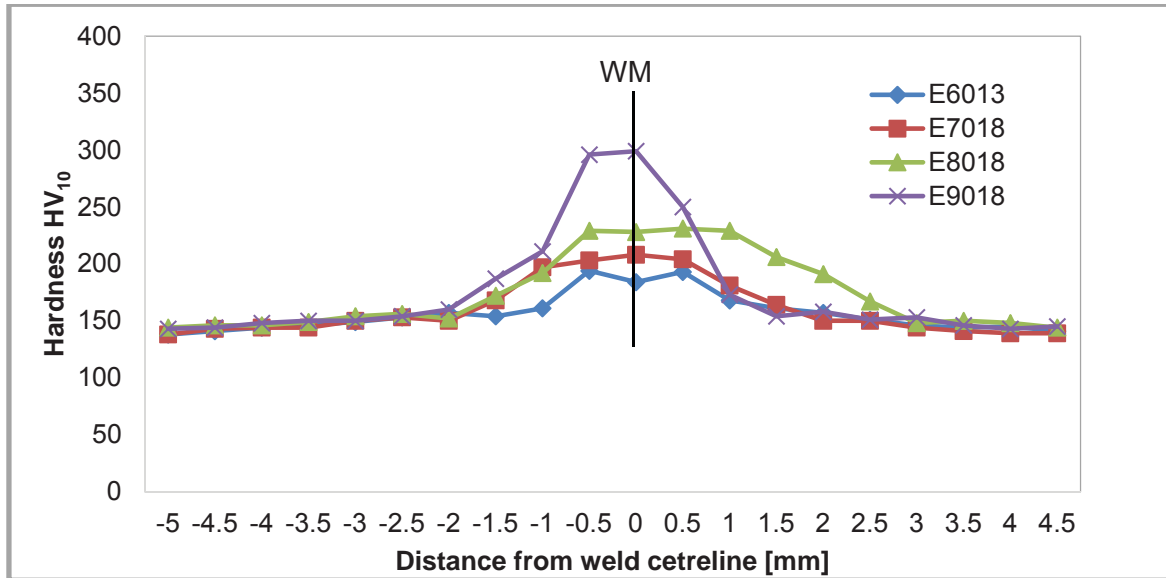


Figure 48: Sample comparison of the bottom hardness HV₁₀. The increase in hardness is indicated for each welding electrode

Figure 49-Figure 51 indicated that the E7018 sample's hardness was plotted before and after the PWHT. The same order as the earlier results was followed from the top to bottom hardness.

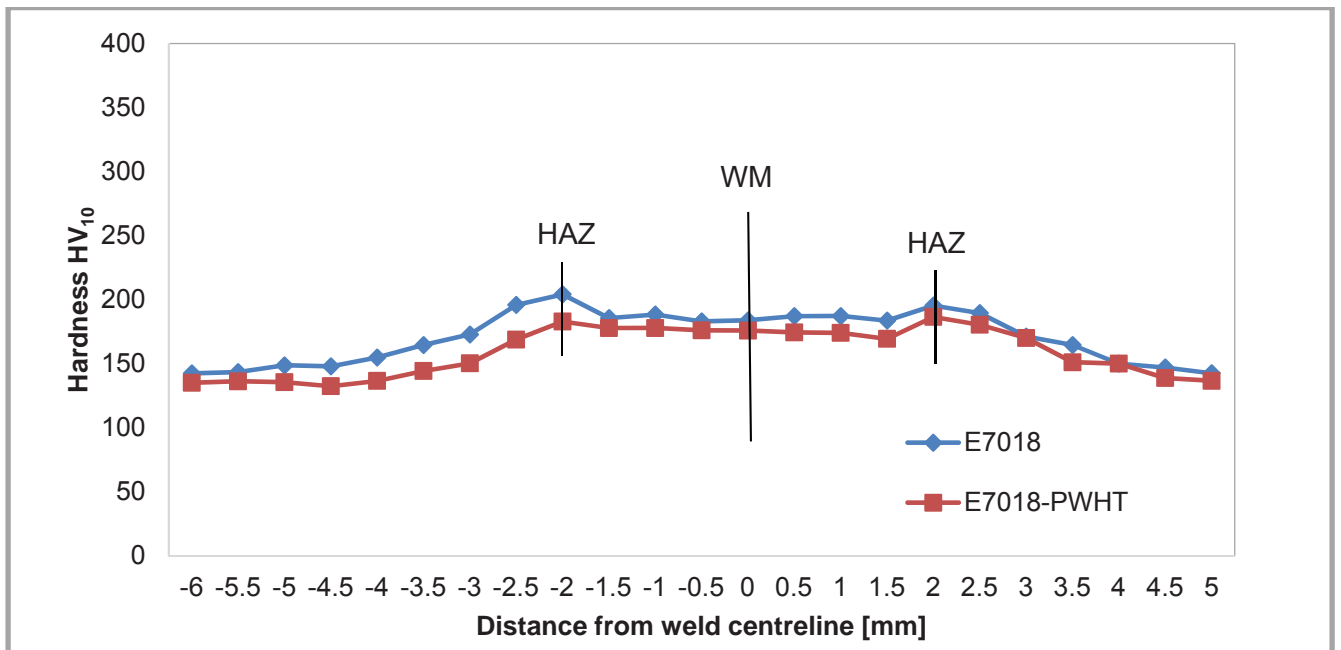


Figure 49: The top hardness HV₁₀ in the weld sample E7018 before the PWHT. This is compared with the E7018-PWHT after a heat treatment at 600°C for two hours

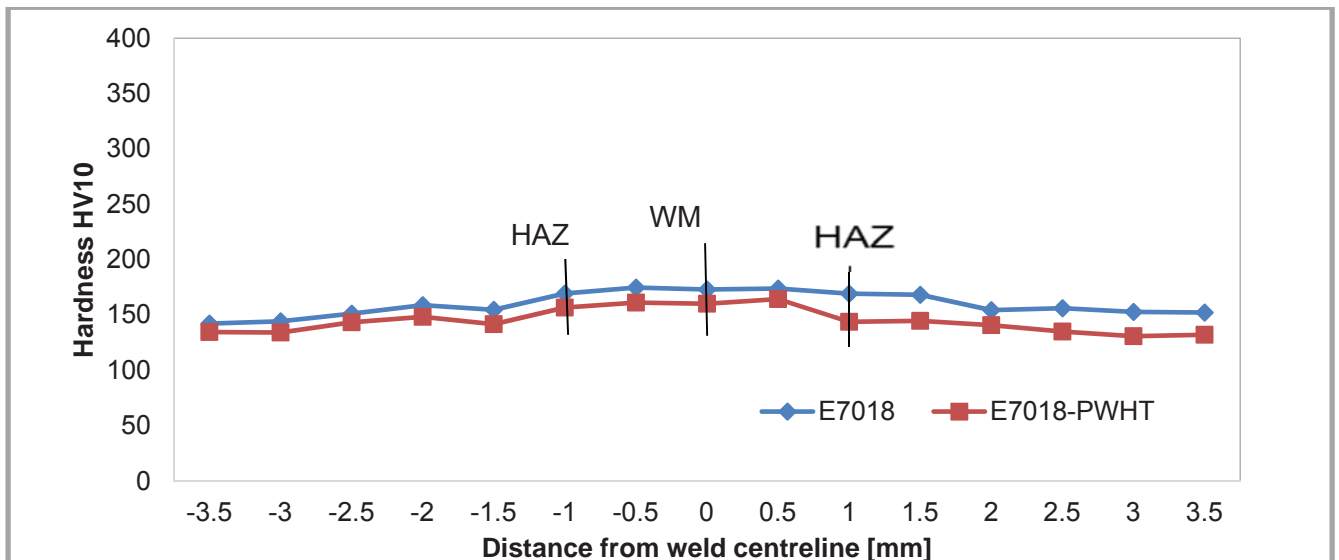


Figure 50: Centre hardness HV₁₀ comparison of the E7018 and E7018-PWHT in the BM, HAZ and WM. The PWHT was at 600°C for two hours. A slight decrease in hardness can be observed

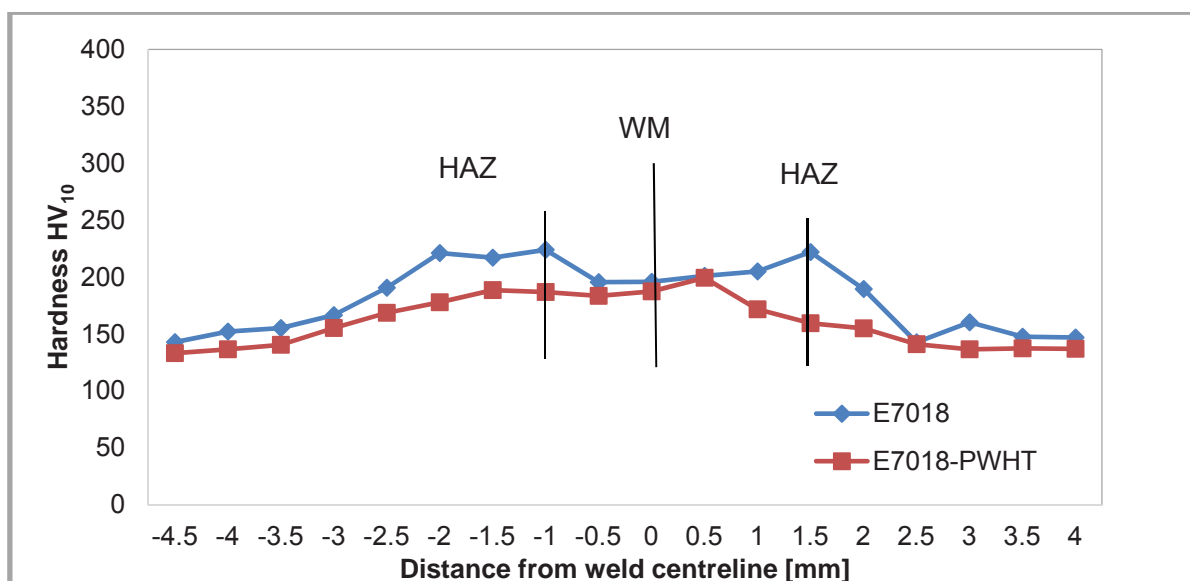


Figure 51: The bottom hardness comparison in HV₁₀ for the E7018 and E7018-PWHT sample in the BM, HAZ and WM. The greatest hardness reduction occurs in the HAZ

Observations

- At the top surface in the E6013 HAZ, the hardness measured (280 HV₁₀) exceeded the standard limitation by NACE SP0472 of 250 HV₁₀. This was the only sample observed with higher hardness than the limitation in the HAZ.
- The final passes (capping) in all of the samples had higher average hardness.

- The PWHT sample had the largest reduction in hardness in the HAZ 30-50 HV₁₀. During the PWHT, a minimal change in hardness, typically less than 15 HV, occurred in the WM.

4.4 Residual stress

Figure 53 and Table 28, the normal, longitudinal and transverse stress distribution of the E7018 sample is illustrated. It is measured at five separate depths through the thickness of the sample at 2.1, 5.2, 8.31, 11.45 and 14.52 mm. The origin of measurement was in the middle of the weld.

Table 28: Residual stress in MPa, measured at separate depths and positions for the normal, transverse and longitudinal stresses for the E7018 sample in the longitudinal direction. The E7018 electrode yield strength was 503 MPa

Direction	Position [mm]	-8	-4	0	4	8
σ_N [MPa]	2.1	12	-78	16	71	75
	5.2	-28	-22	-2	16	57
	8.31	1	103	46	-2	4
	11.45	58	15	68	-36	-76
	14.52	53	67	76	34	0
σ_L [MPa]	2.1	438	406	494	564	384
	5.2	298	337	384	385	316
	8.31	325	532	495	383	263
	11.45	467	515	619	424	247
	14.52	452	548	561	433	375
σ_T [MPa]	2.1	62	-40	54	144	153
	5.2	-115	-198	-167	-83	2
	8.31	-22	33	-45	-66	-36
	11.45	214	219	262	101	13
	14.52	176	181	139	152	162

Residual stress observations in the E7018 sample

- The largest tensile stress in the longitudinal direction is at a depth of 11.45 mm (619 MPa), followed by the stress at a depth of 2.1 and 14.52 mm at the same magnitudes (560 MPa).
- The longitudinal stress was the highest of the three components, confirming published results [32]. It also proved that the largest stress in the longitudinal direction was in the centre of the welded joint throughout the depth of the

sample, within 4 mm of the weld centreline. The largest stress measured was 619 MPa in the longitudinal direction at a depth of 8.31 mm. There was no compressive stress in the longitudinal direction.

- Many measured values for the specific component of the residual stress exceeded the yield strength. A stress higher than the yield strength (σ_y) is not possible. This aspect is discussed in Section 5.4.

In

Figure 53 and Table 29 the normal, longitudinal and transverse stress for the E7018-PWHT is shown.

Table 29: Residual stress measured at separate depths and positions for the normal, transverse and longitudinal stress for the E7018-PWHT sample. The E7018 electrode yield strength was 503 MPa

Direction	Position [mm]	-8	-4	0	4	8
σ_N [MPa]	2.1	13	-28	-27	-8	-1
	5.2	25	-3	-3	10	-9
	8.31	12	-17	-29	23	-9
	11.45	12	-20	-8	14	3
	14.52	-10	-27	-30	3	33
σ_L [MPa]	2.1	42	12	37	14	37
	5.2	43	55	33	46	-5
	8.31	36	52	99	86	8
	11.45	18	50	86	90	23
	14.52	66	75	51	54	71
σ_T [MPa]	2.1	28	-29	-26	2	39
	5.2	43	35	28	22	8
	8.31	25	8	6	39	8
	11.45	-7	-11	4	9	9
	14.52	-2	-28	-43	-3	30

Residual stress observations in the E7018-PWHT sample

- The longitudinal tensile stress across the weld is significantly reduced to an average of 74 MPa (from 587 MPa) before the PWHT.
- In the longitudinal direction, the welded area is in tensile stress across the weld while in the transverse direction, the average stress across the weld is close to 0 MPa and the normal stress (-30 MPa) is compressive.

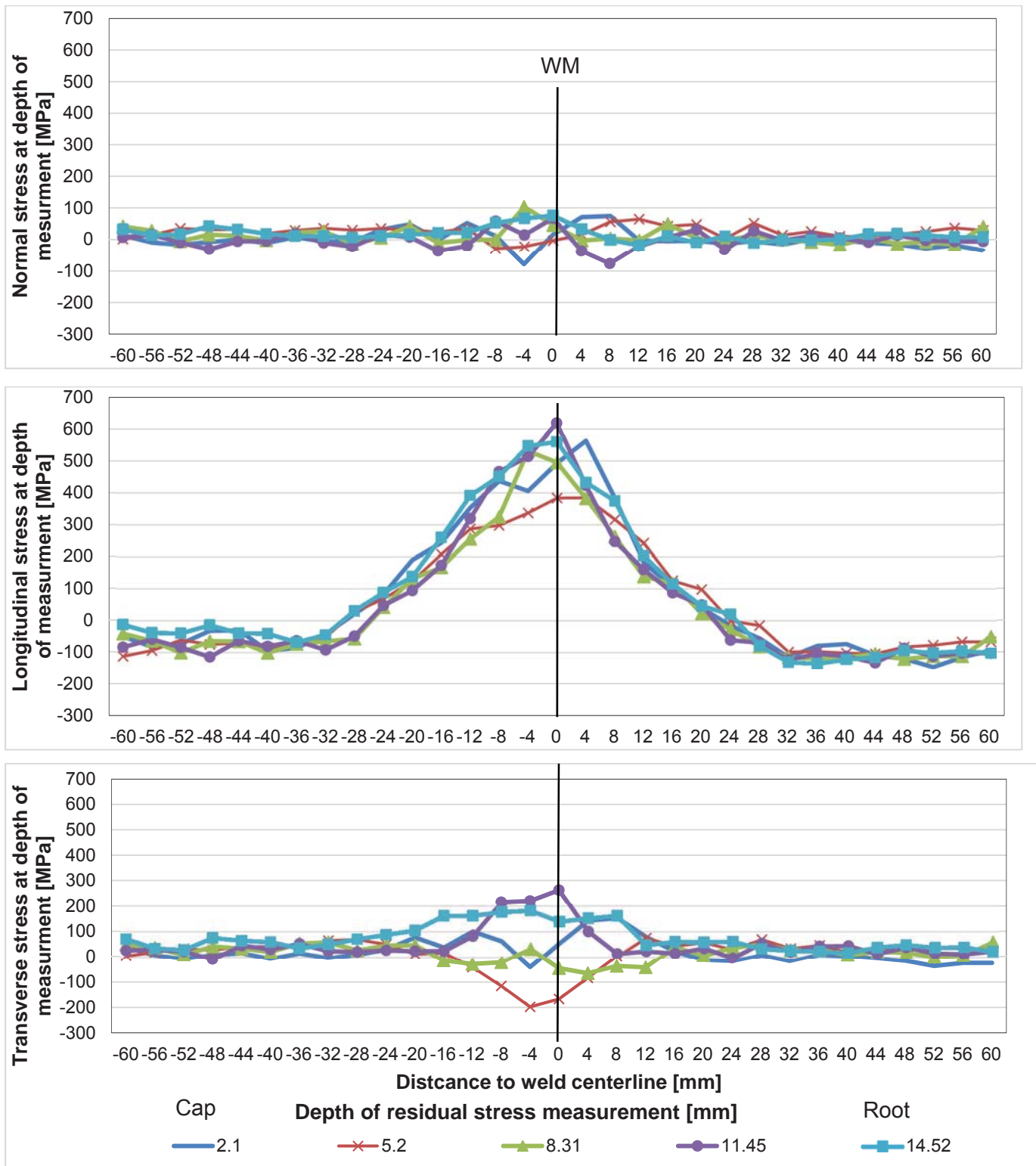


Figure 52: The normal, longitudinal and transverse stress distribution for the E7018 electrode without a PWHT. The stress levels are measured at separate depths in the welded samples

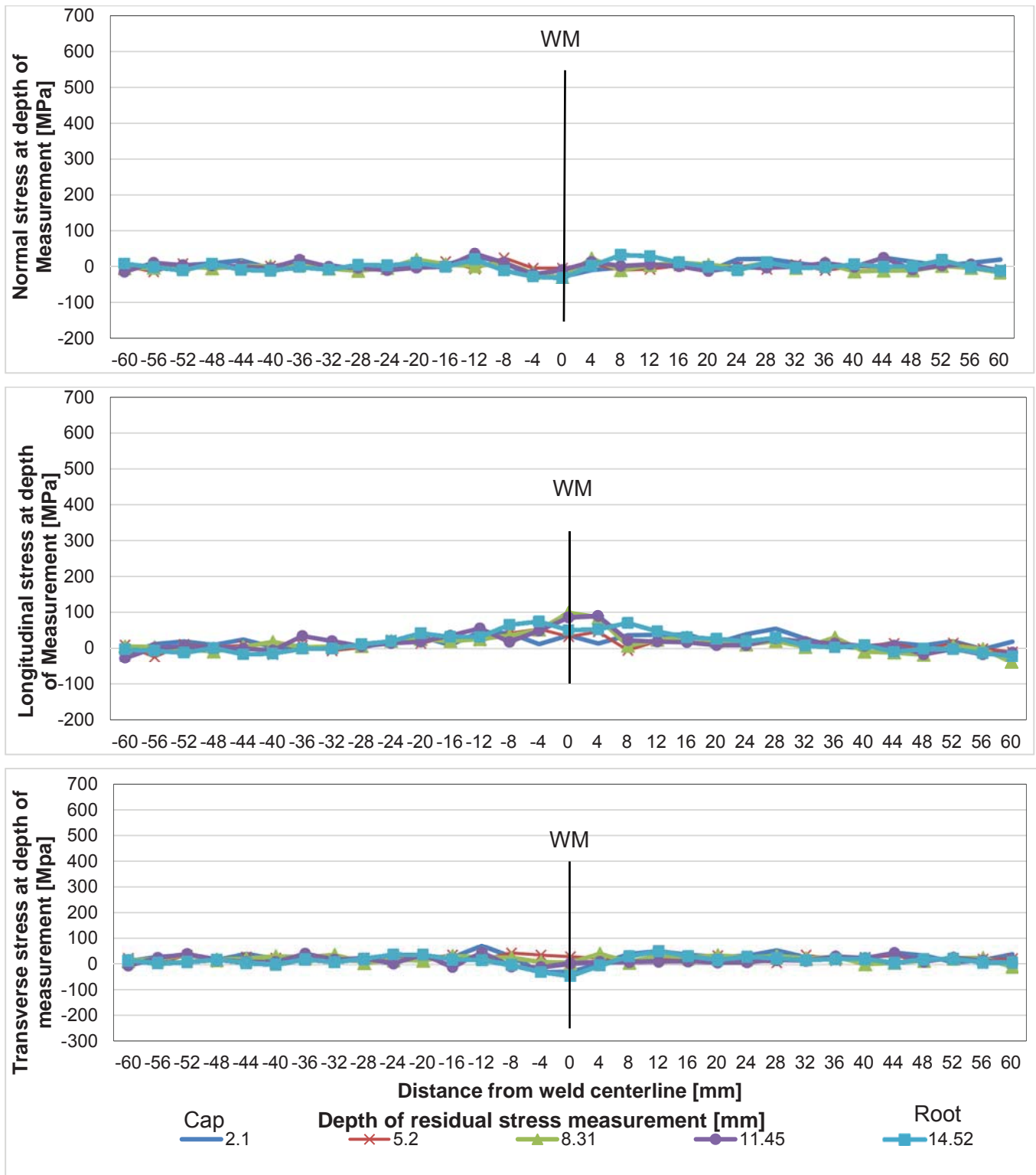


Figure 53: The normal, longitudinal and transverse distribution for the E7018-PWHT. The stress levels is measured at separate depths in the welded samples after the PWHTs were completed

In

Figure 55 and Table 31 the normal, longitudinal and transverse stress distribution of the E8018 can be observed.

Table 30: Residual stress in MPa, measured at separate depths and positions for the normal, transverse and longitudinal stress for the E8018 sample. The E8018 electrode yield strength was 491 MPa

Direction	Position [mm]	-8	-4	0	4	8
σ_N [MPa]	2.1	-156	111	-42	-100	-18
	5.2	-184	-64	50	99	-2
	8.31	-78	51	160	238	114
	11.45	-23	-35	87	48	-25
	14.52	-5	-111	47	130	52
σ_L [MPa]	2.1	257	497	207	240	283
	5.2	151	336	396	380	236
	8.31	227	435	558	549	402
	11.45	357	444	530	447	370
	14.52	357	308	477	523	417
σ_T [MPa]	2.1	-119	94	-101	-142	-83
	5.2	-208	-200	-114	-84	-126
	8.31	-99	-86	36	195	112
	11.45	120	100	292	183	145
	14.52	119	-31	111	156	114

Residual stress observations in the E8018 sample

- In the normal direction, there are large stresses up to 237 MPa. The left-hand side of the weld up to the FL is in compression from 0 to 8 mm, while the right-hand side up to the FL from 0 to 8 mm is in tension up to the maximum stress of 237 MPa.
- In the transverse direction, the maximum residual stresses are in the centre of the welded plate at depths of 8.31 and 11.45 mm.
- In the longitudinal direction, the maximum stresses are in the centre of the weld at depths of 8.31 mm and 11.45 mm, at 558 MPa and 529 MPa respectively.
- The peak transverse and normal stresses are half of the longitudinal stress.

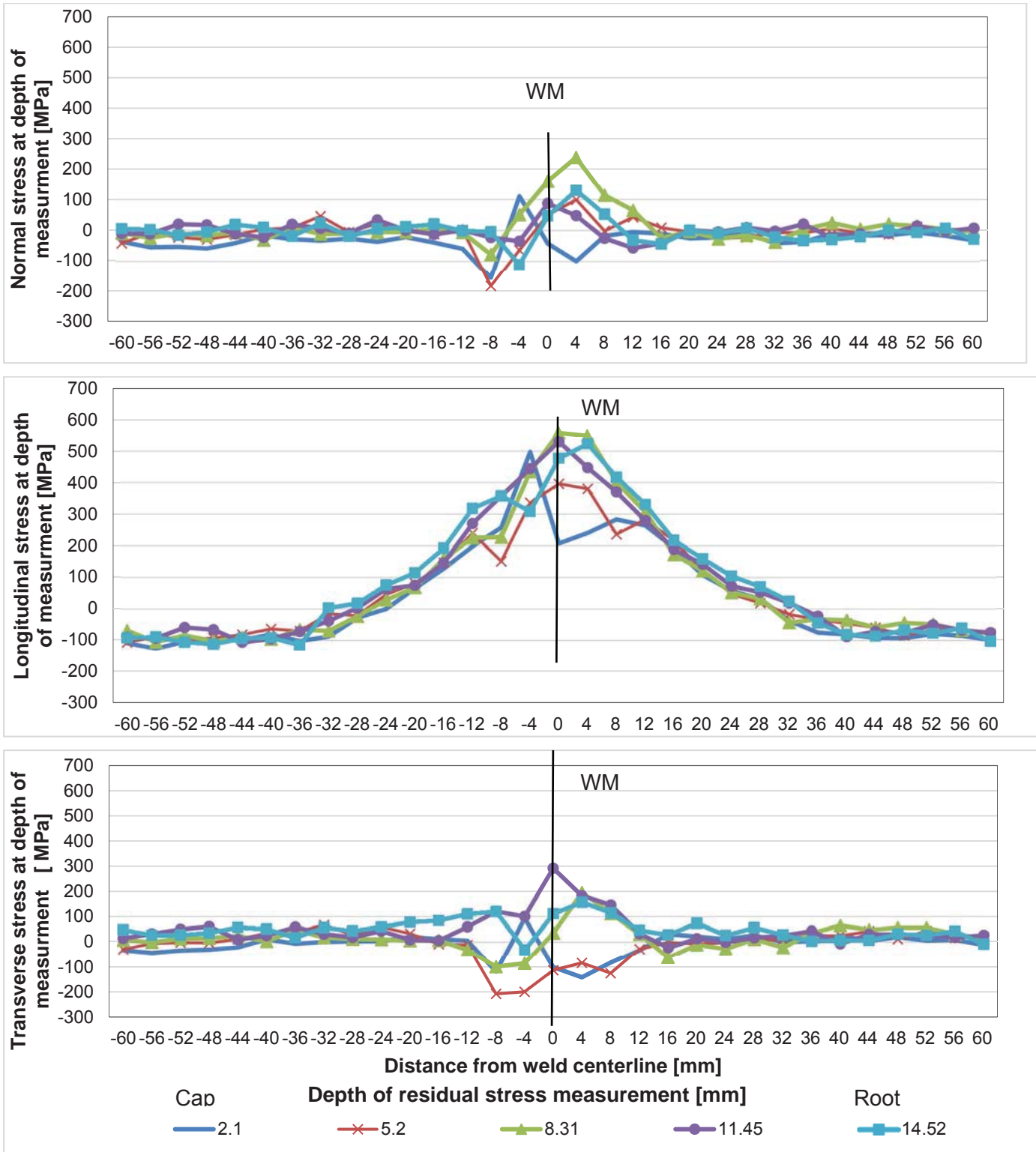


Figure 54: The normal, longitudinal and transverse distribution for the E8018 electrode. The stress levels are measured at separate depths in the welded samples

In

Figure 55 and Table 31 the normal, longitudinal and transverse stress distribution of the E9018 can be observed.

Table 31: Residual stress in MPa, measured at separate depths and positions for the normal, transverse and longitudinal stress for the E9018 sample. The E9018 electrode yield strength was 659 MPa

Direction	Position [mm]	-8	-4	0	4	8
σ_N [MPa]	2.1	-142	-91	-139	-135	-28
	5.2	-93	26	-134	24	-51
	8.31	-30	40	56	-210	-55
	11.45	-96	-106	47	-114	16
	14.52	-31	47	72	-19	141
σ_L [MPa]	2.1	192	267	267	146	245
	5.2	263	388	218	367	271
	8.31	304	541	686	195	243
	11.45	171	369	536	313	276
	14.52	263	282	472	478	450
σ_T [MPa]	2.1	-137	-218	-126	-154	14
	5.2	-19	62	-94	151	54
	8.31	22	83	47	-187	-81
	11.45	-160	-203	-67	-63	-9
	14.52	-18	50	70	60	350

Residual stress observations in the E9018 sample

- In the normal stress distribution, there is a large compressive stress peak at 4 mm below the top surface. This sequence repeats at depths 8.31, 11.45 and 14.52 mm.
- There are large peak stresses away from WM near the FL that can be established in the transverse direction at 4:8 mm.
- The largest longitudinal stress is at a depth of 8.31 mm (686 MPa) followed at a depth of 11.45 mm (536 MPa).
- It can be understood that the peak transverse stresses are half of tensile stress.

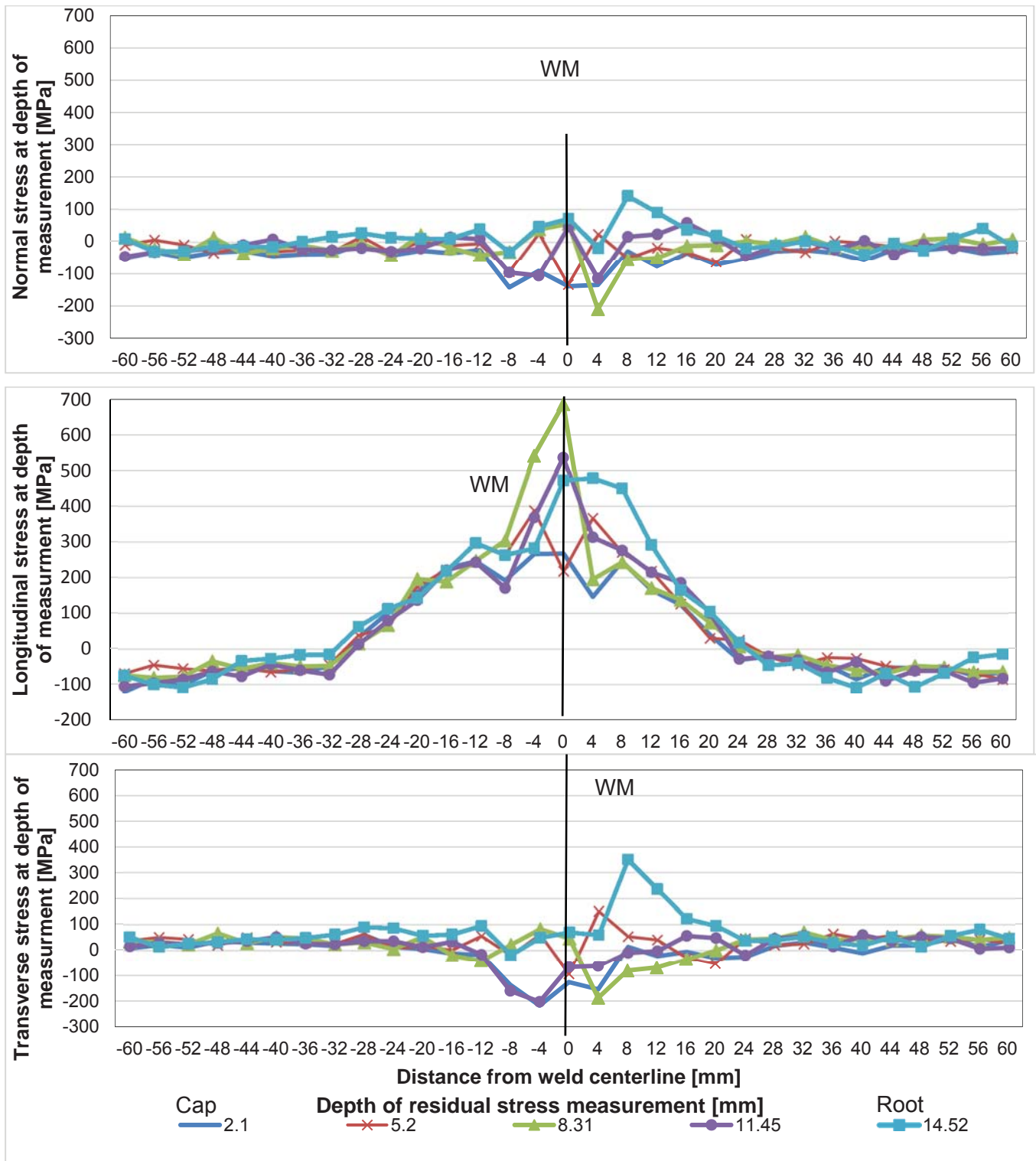


Figure 55: The normal, longitudinal and transverse distribution for the E9018. The stress levels are measured at separate depths in the welded samples

4.5 Microstructures

The following HAZ microstructures (Figure 56-Figure 64) were taken in the root for the E6013, E7018, E9018 and E7018-PWHT. This is a representative of a low, average, and high HI and the effect of the PWHT on the HAZ. In Figure 56, the E6013 with an average low HI of 0.5 kJ/mm is shown. The E6013 HAZ has coarsened grains consisting of primary ferrite with large portions of aligned second phase (AC) and WF side-plates.

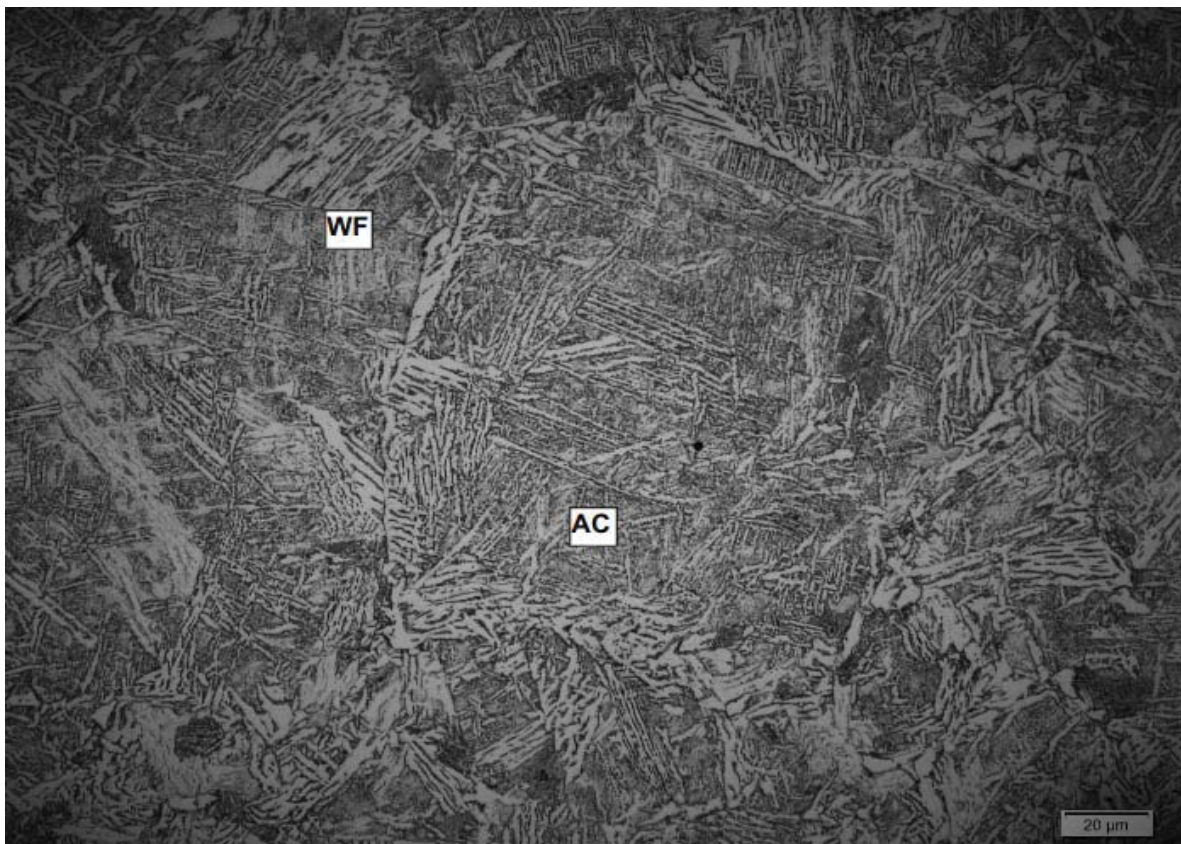


Figure 56: E6013 heat-affected zone, grain coarsened ferrite with AC and WF can be observed. HI is at 0.5 kJ/mm. All images were taken at 50x magnification

Figure 57 indicates the E7018 HAZ with an average HI of 0.7 kJ/mm. The E7018 HAZ comprised large grain refined and grain coarsened HAZ.

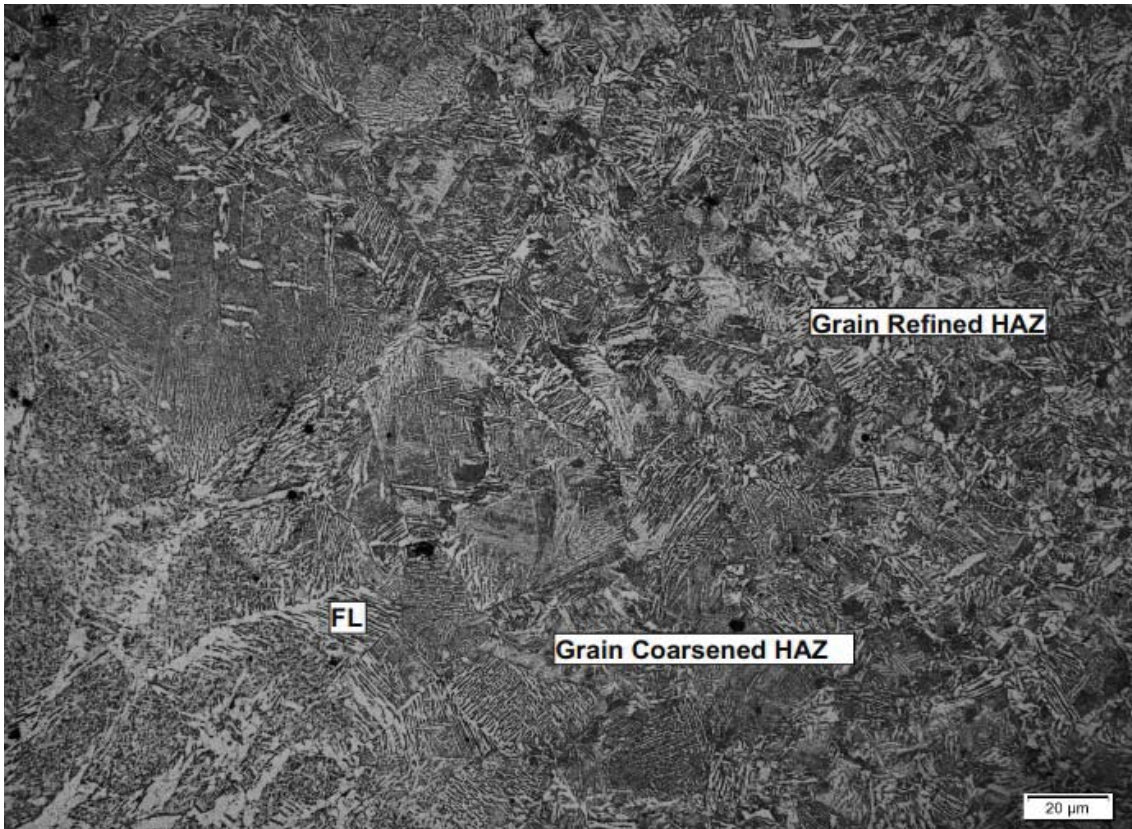


Figure 57: E7018 heat-affected zone, a grain refined and grain coarsened HAZ can be observed. HI was at 0.7 kJ/mm. All images were taken at 50 x magnification.

In Figure 58, the E8018 HAZ comprised out of ferrite with aligned second phase (AC) in the grain coarsened HAZ. The average HI was 1.0 kJ/mm.

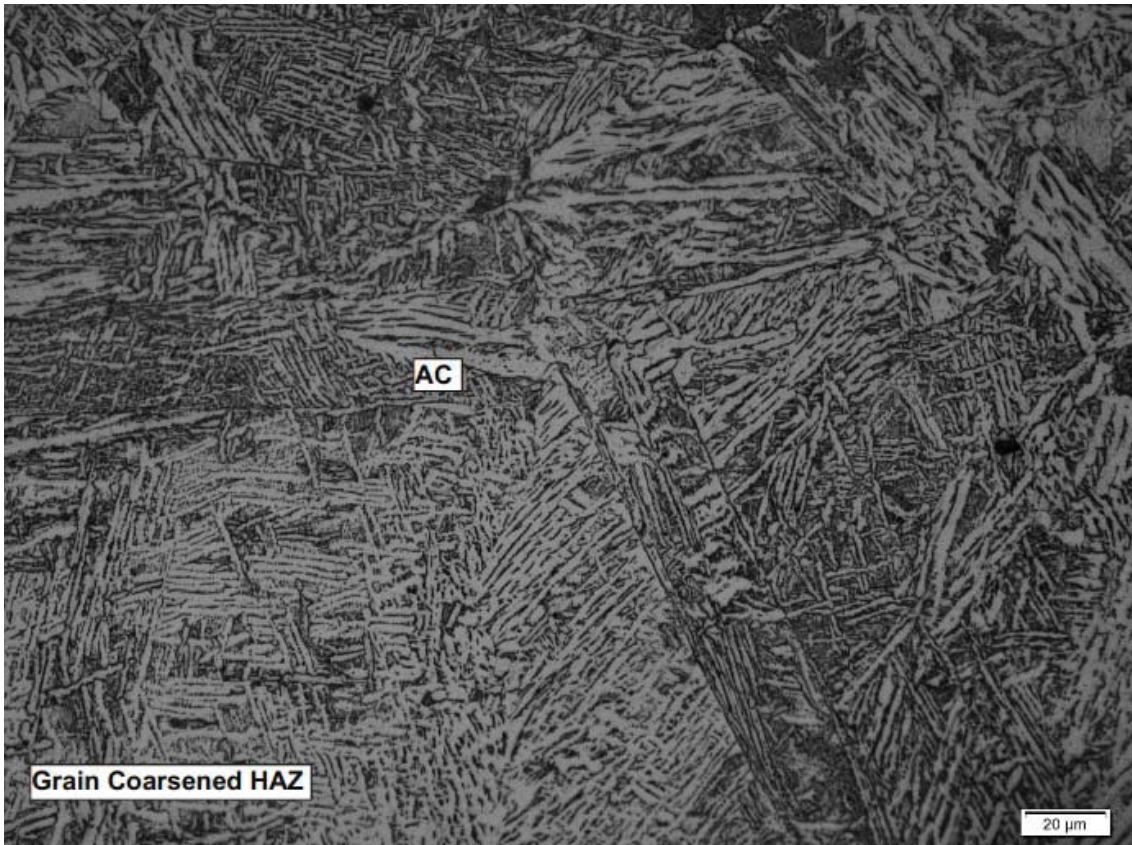


Figure 58: E8018 HAZ, grain coarsened HAZ with AC. High HI was at 1.0 kJ/mm. The sample was taken at 50x magnification

Figure 59, the E7018-PWHT HAZ comprised large quantities of equiaxed ferrite-carbide.

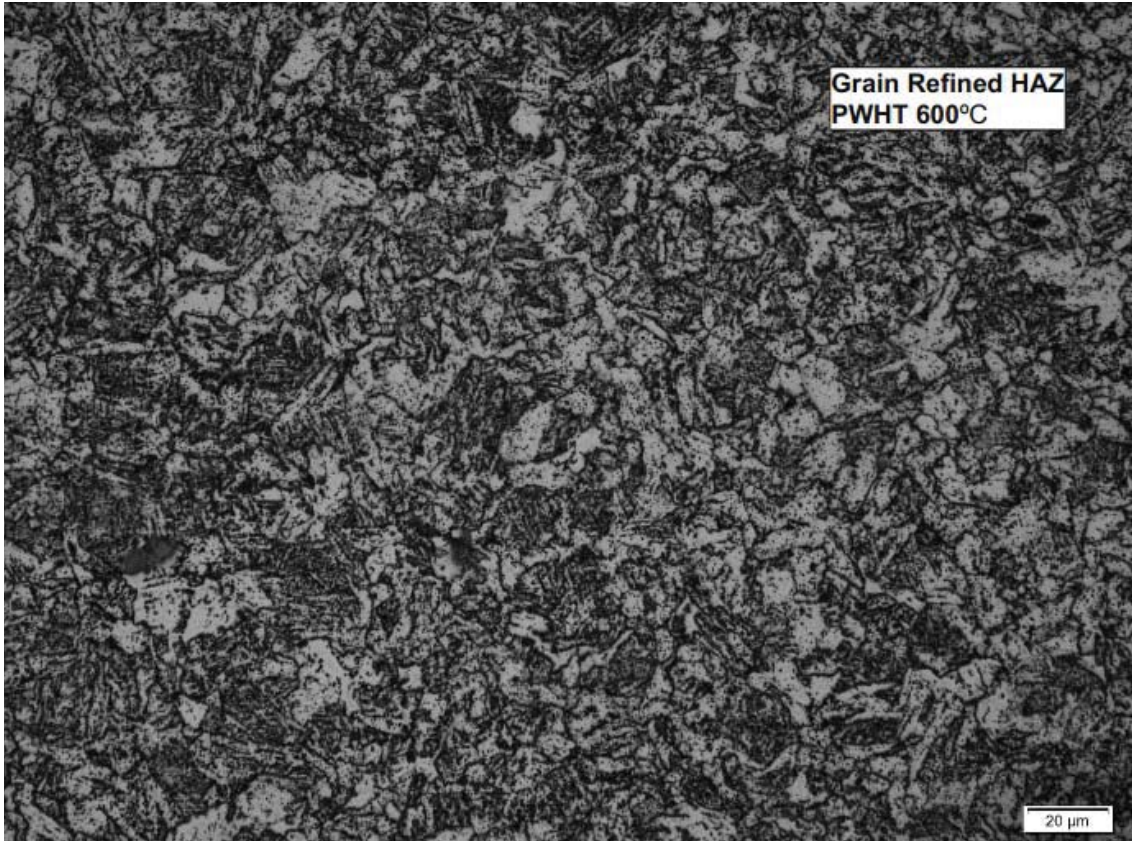


Figure 59: The E7018-PWHT HAZ predominantly comprised of equiaxed ferrite-carbide. Sample underwent a PWHT at 600°C for two hours. All images were taken at 50x magnification

The following microstructures were taken in Figure 60-Figure 64 for the E6013, E7018, E8018, E9018 and E7018-PWHT WM. In Figure 60, the E6013 WM had large quantities of grain boundary ferrite (GF), blocky ferrite (BF) and Widmanstätten Ferrite WF.

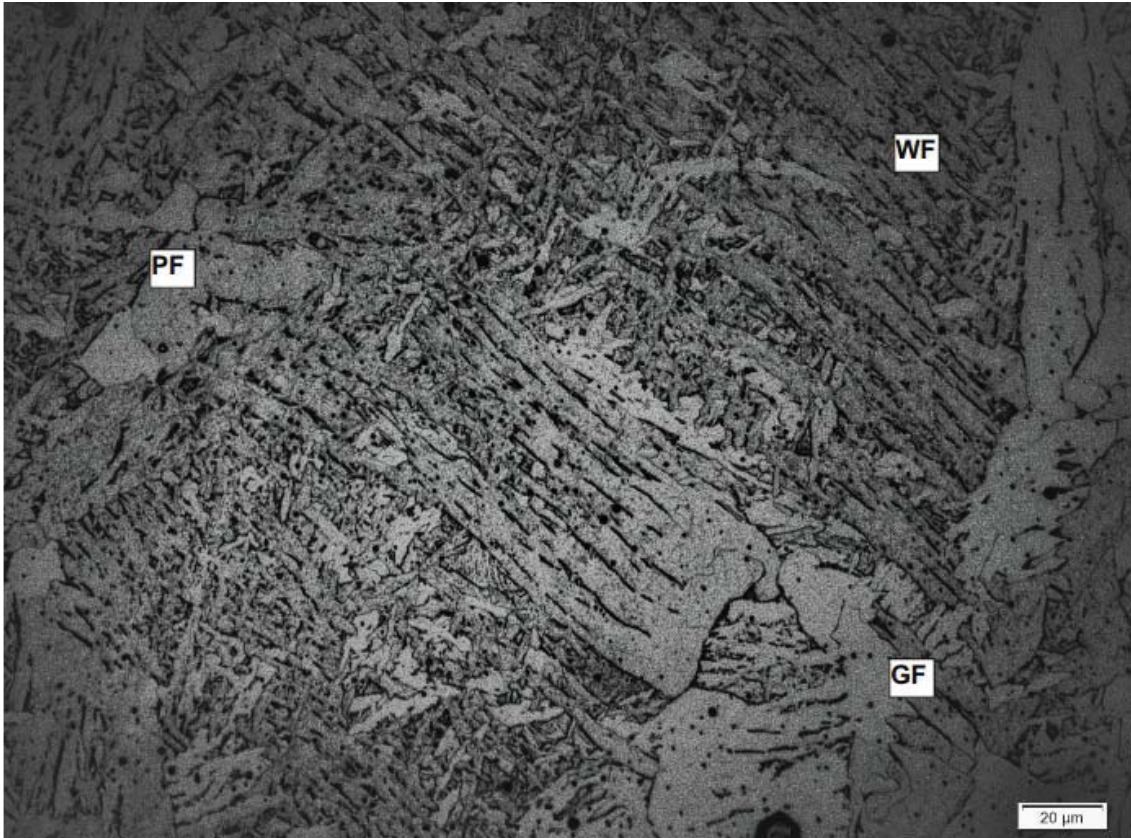


Figure 60: The E6013 WM had large quantities of GF with some BF and WF. Grains are much larger compared to other samples. All images were taken at 50x magnification

In Figure 61, the E7018 WM comprised acicular ferrite (AF, grain boundary ferrite (GF), ferrite and aligned martensite austenite and carbides (MAC).

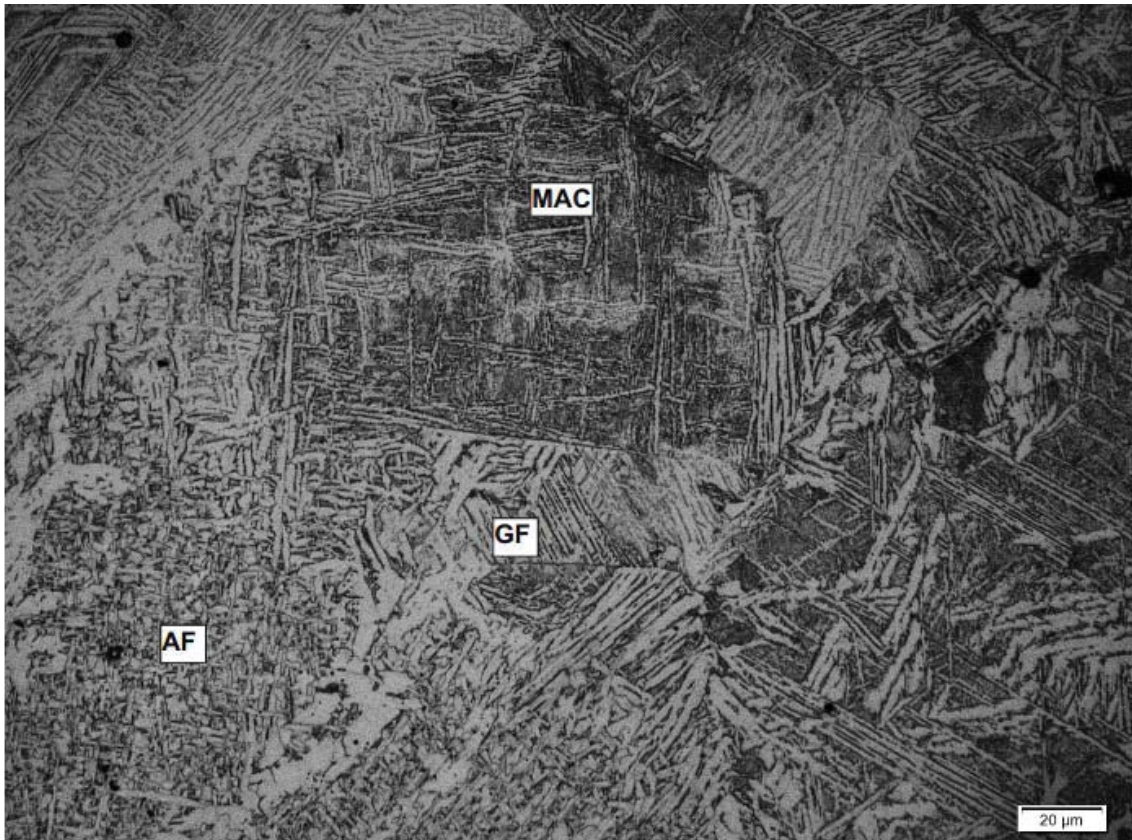


Figure 61: The E7018 WM acicular ferrite (AF, grain boundary ferrite (GF, ferrite and aligned MAC. All images were taken at 50x magnification

In Figure 62, the E8018 WM had some GF with aligned MAC, with the majority of the weld comprising of AF.

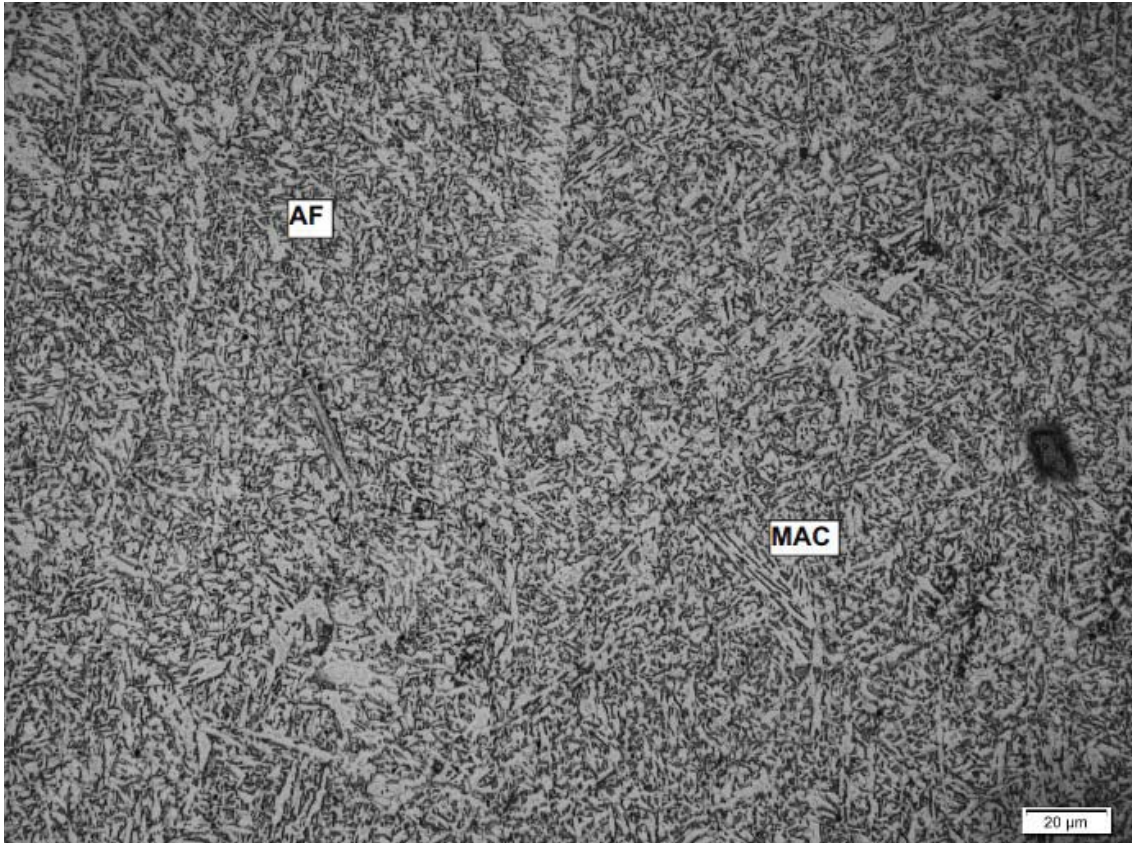


Figure 62: The E8018 WM, AF and ferrite with aligned MAC is shown. The sample was taken at 50x magnification

The E9018 WM was comprised entirely of Bainite (B). This is consistent with the increase of Cr-Mo into the weld metal.

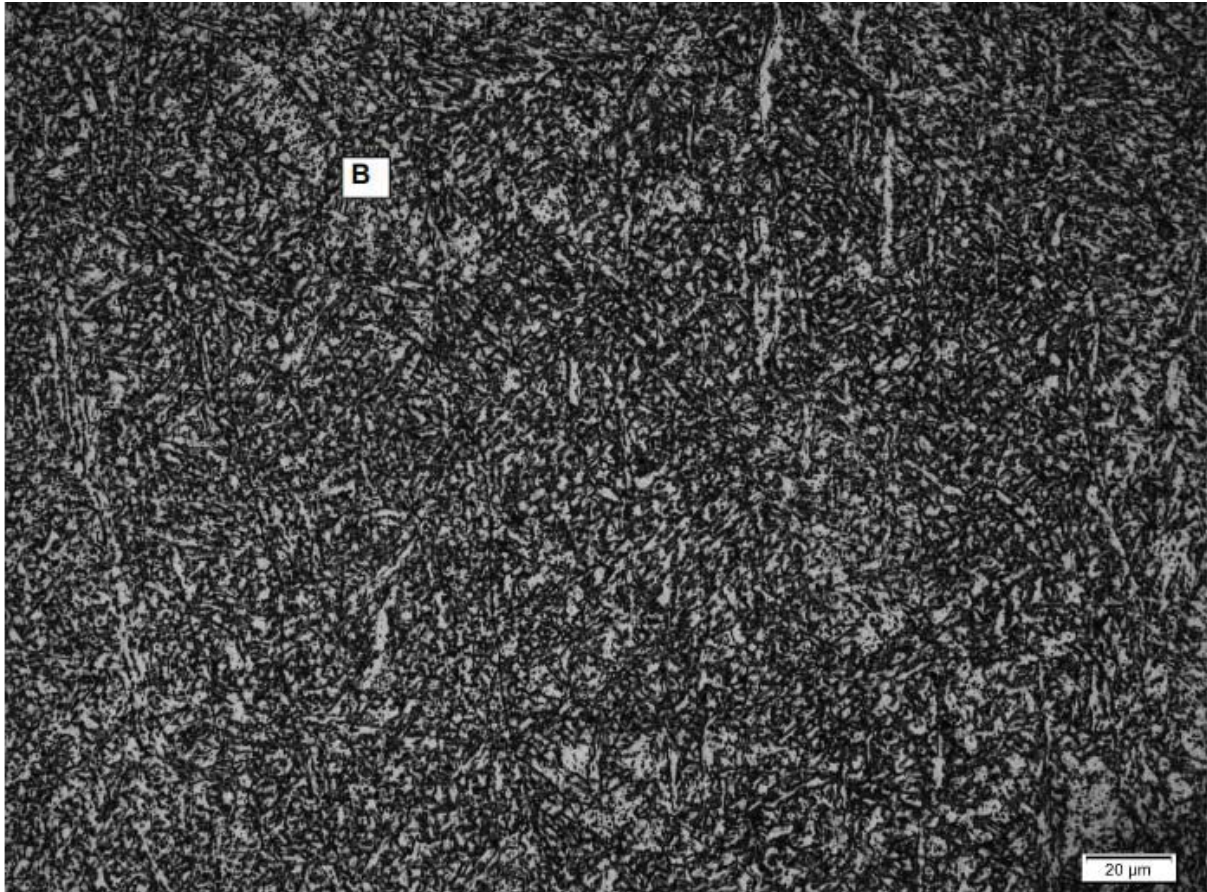


Figure 63: E9018 weld metal, consisting entirely of Bainite (B). All images were taken at 50x magnification

In Figure 64 the E7018-PWHT WM can be observed; the sample comprised large ferrite grains and grain refined areas.

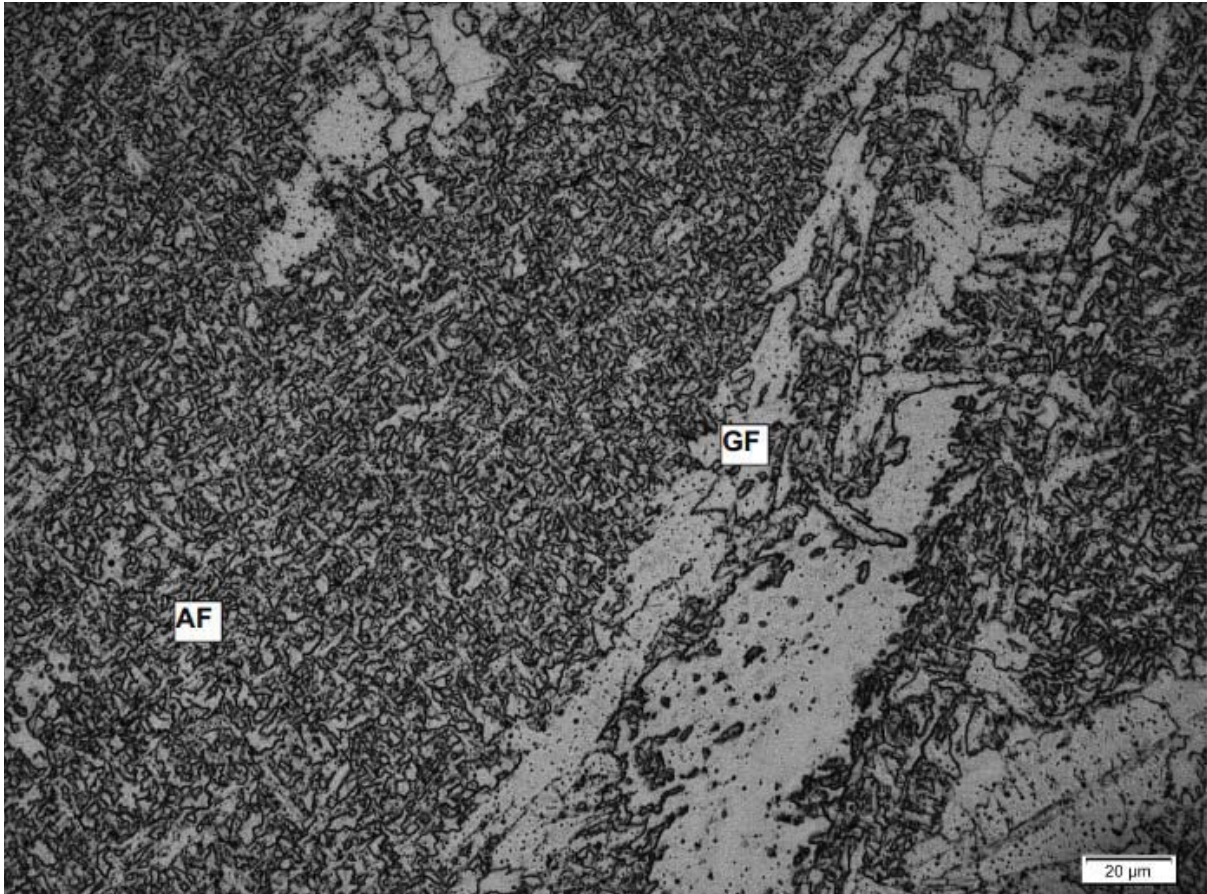


Figure 64: The E7018-PWHT WM comprising of large ferrite grains and AF. The Images was taken at 50x magnification

4.6 Stress-corrosion cracking test

4.6.1 Evaluation of base metal cracking observed in samples

After metallographic preparation, cracks were observed in the base material of all test coupons. The crack morphology was typical of HIC. The type of HIC can be classified as stepwise cracking (NACE TM0103-2003). In Section 2.6.6, the CLR, CTR and CSR were calculated. The comparison was made on the crack length of samples in Table 32. The dimensions differ with the biggest cracks in E7018 and E9018. The E6013 and E8018 crack dimensions were the smallest and it passes the acceptance criteria.

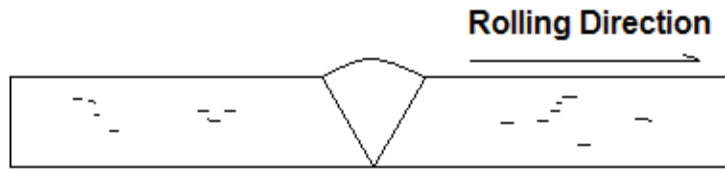


Figure 65: Schematic transverse section on AA indicating the rolling direction and cracks in the BM

Table 32: Length of Hydrogen-Induced Cracking (HIC) cracking lengths in BM. Values in bold indicates that crack ratios were higher than the acceptance criteria

Electrode	Crack measurements (mm)	Crack length Ratio (%)	Crack Thickness Ratio (%)	Crack Sensitivity Ratio (%)	Failure Location
E6018	3.388×0.411	3	2	1	BM
E7018	18.858×1.611	19	10	2	BM
E8018	1.126×0.123	9	3	0	BM
	1.827×0.195				
	3.943×0.197				
	1.828×0.092				
E9018	19.294×2.365	23	57	4	BM
	3.745×7.416				
Acceptance Criteria (%)*		15	5	2	

*Criteria are all the maximum allowed

In Figure 65, a transverse section with a sketch of cracks and rolling direction is shown. The morphology of the cracks is repeated throughout the samples to at least 5 mm away from the HAZ.

In Figure 67, an image shows the typical observed cracks. In Figure 66-Figure 71, the cracks are present in the BM. The measured crack length and width of the respective samples is stated on the images. In Figure 66 and Figure 67, the E6013 sample is illustrated.

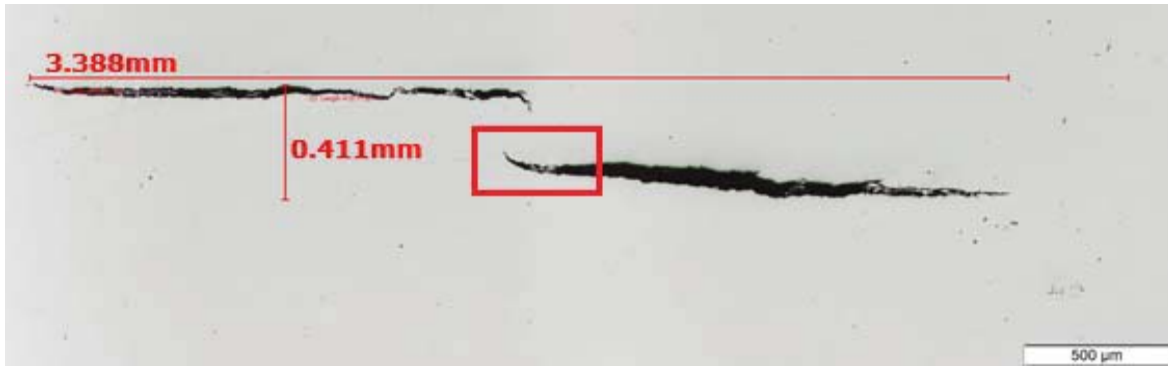


Figure 66: Polished and measured micrograph of the E6013 electrode sample showing HIC cracks at the BM

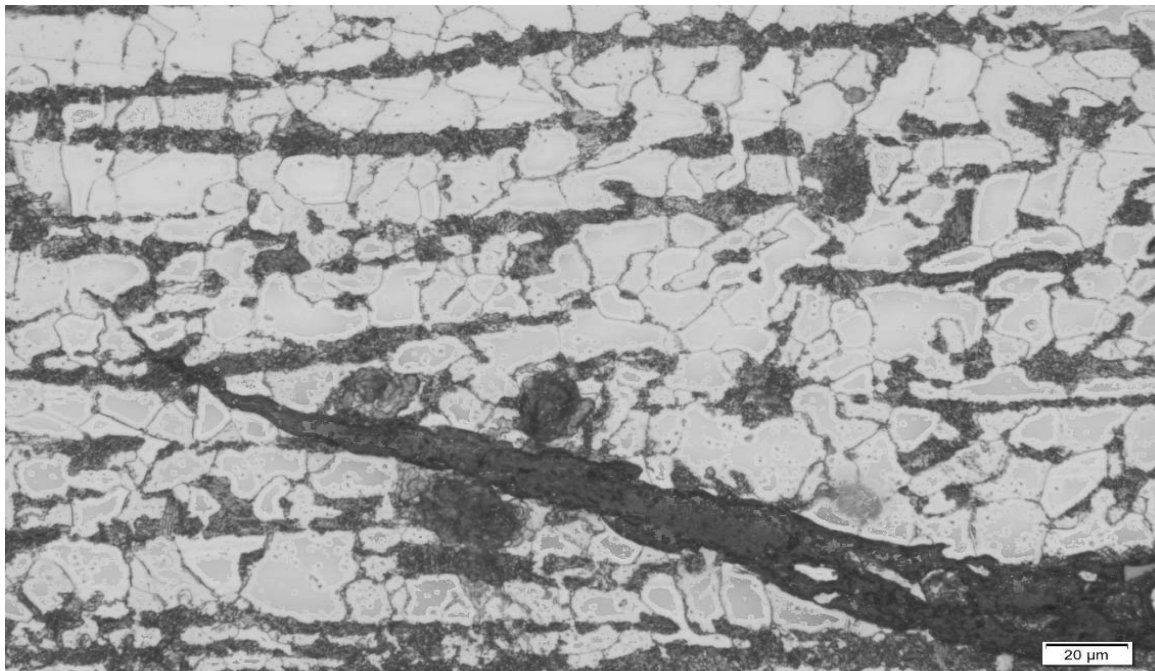


Figure 67: Typical cracks observed at 500x magnification. This image was taken from sample E6013. The crack is a magnification of the red square in Figure 66



Figure 68: Polished and measured micrograph of the E7018 showing HIC cracks in the BM. The dimensions were 18.858x1.611 mm

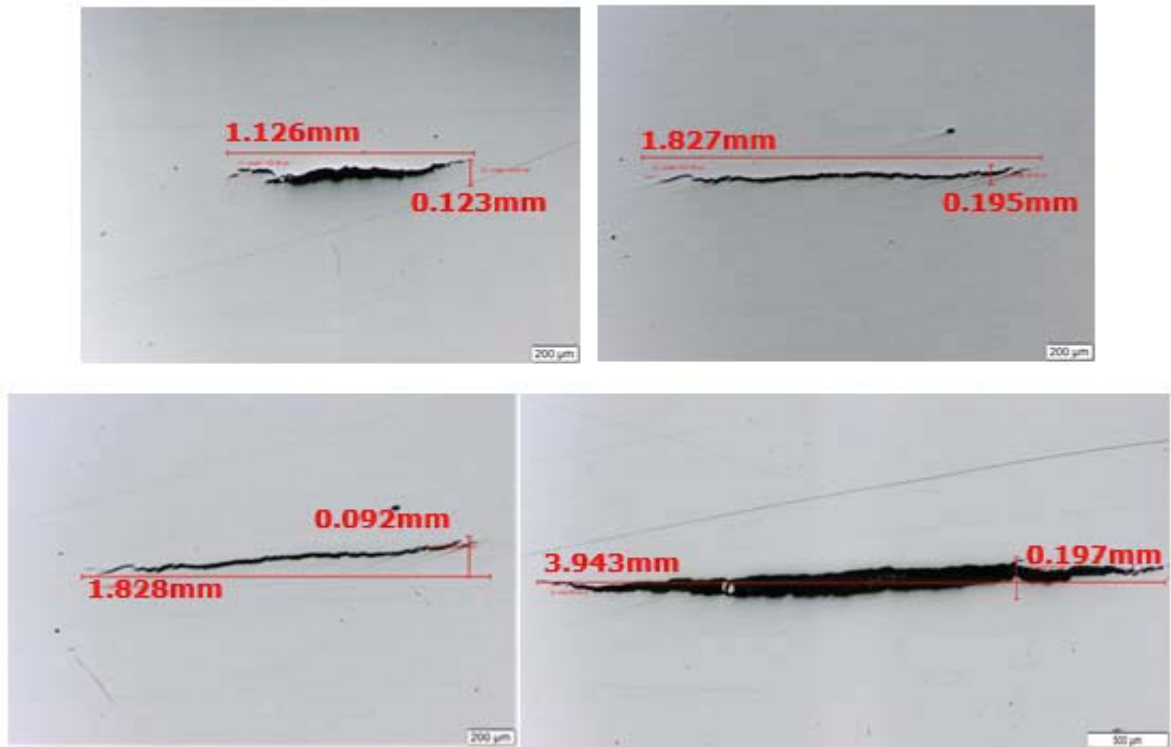


Figure 69: Polished and measured micrographs of sample E8018 showing cracks in the BM



Figure 70: Polished and measured micrograph of the E9018, showing HIC cracks in the BM of 2.365x19.294 mm

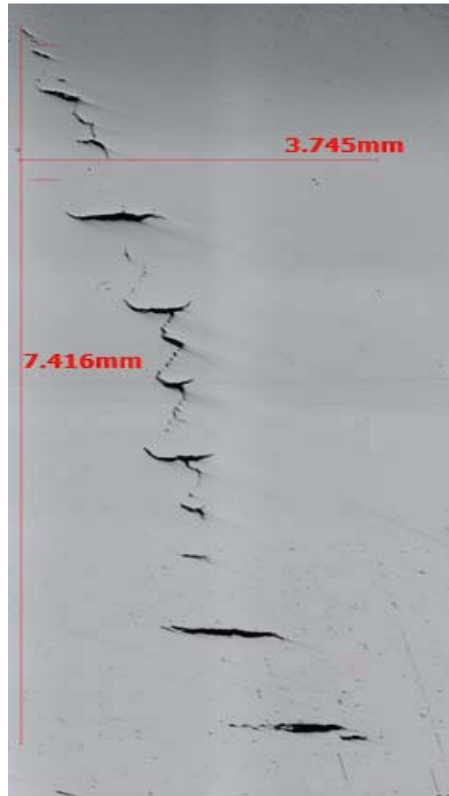


Figure 71: Polished and measured micrograph of the E9018 electrode sample showing HIC (stepwise cracking) cracks at the BM of length 7.416x3.745mm

4.6.2 Weld metal cracking observed in the E9018 sample (SCC)

From Section 4.4, the peak residual stress was proven to be on the weld centreline. It can be understood that the crack originated from the outer surface and progressed to the middle of the weld where the stress was the largest. In Figure 72-Figure 73, the E9018 sample is illustrated with a defect in the WM; this was only observed in the E9018 electrode. Magnetic particle inspection indicated cracks across the outer surface of the E9018 sample. All the other samples' outer surfaces were defect-free.

The defect was studied under SEM (Scanning Electron Microscopy) to determine the chemical composition of the non-metallic inclusion (Figure 74). A chemical composition is included from Spectra 1-3 on the images and the comparison is in Figure 75-Figure 77. The spectrum indicates an increase in oxygen content from Spectrum 1 to Spectrum 2 and 3. The corroded product is suspected to be Fe_2O or Fe_2CO_3 .

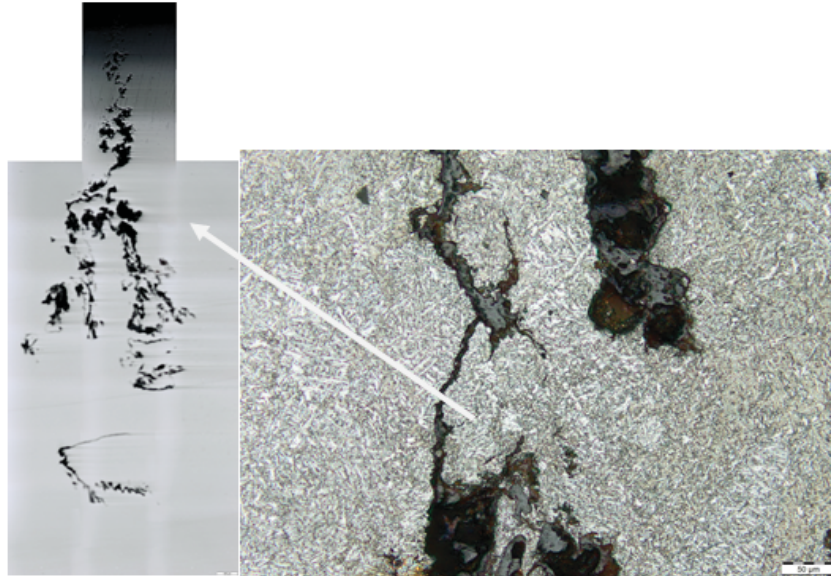


Figure 72: SCC in the E9018 WM; the left-hand side is the polished micrograph, and on the right is the etched microstructure. The crack originated from the outer surface into the centre of the weld



Figure 73: The branch-like SCC cracking of the E9018 WM. There were severe cracks in the centre of the welded member

Figure 74 indicates the SEM analysis of three sections in the WM. The only parts that indicated corrosion were Spectra 2 and 3.

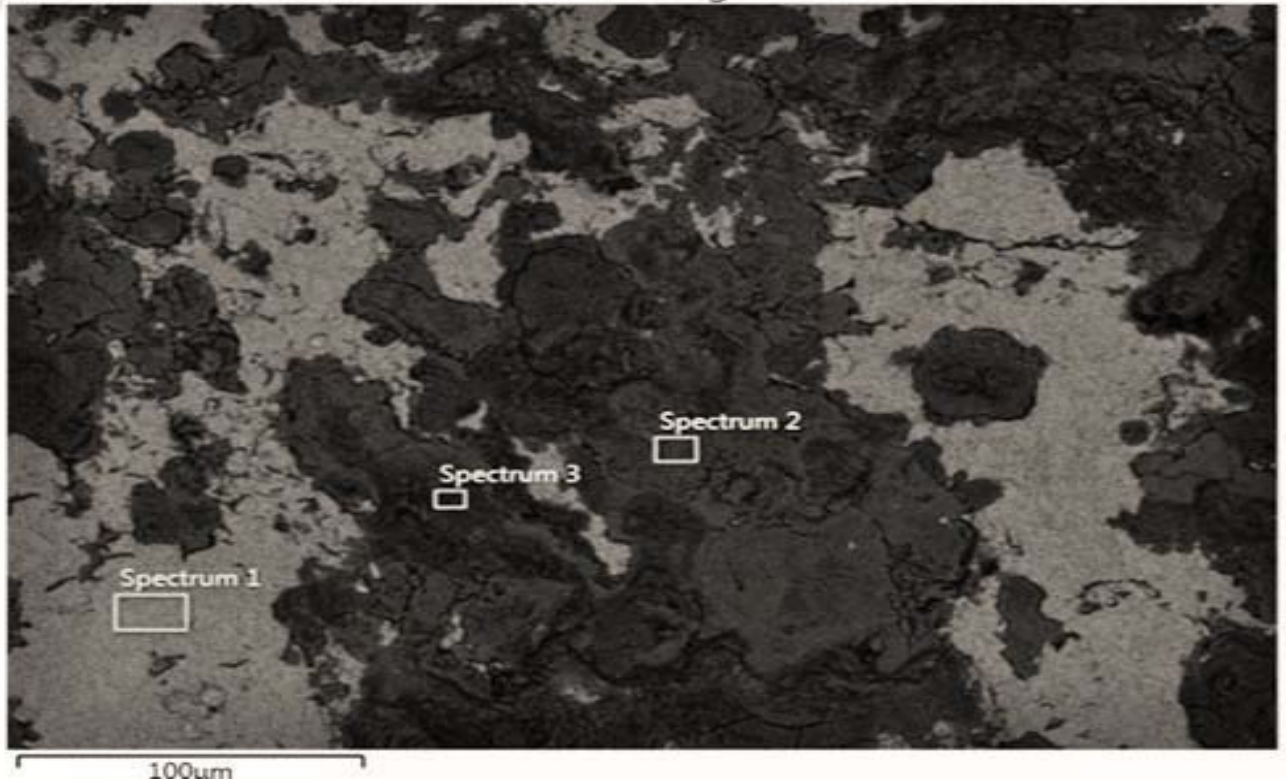


Figure 74: A SEM analysis was conducted in the crack to ensure that the crack was not progressing through the presence of a non-metallic inclusion such as slag. Spectrum 1 comprises un-corroded WM and Spectrum 2 and 3 are within the corroded condition

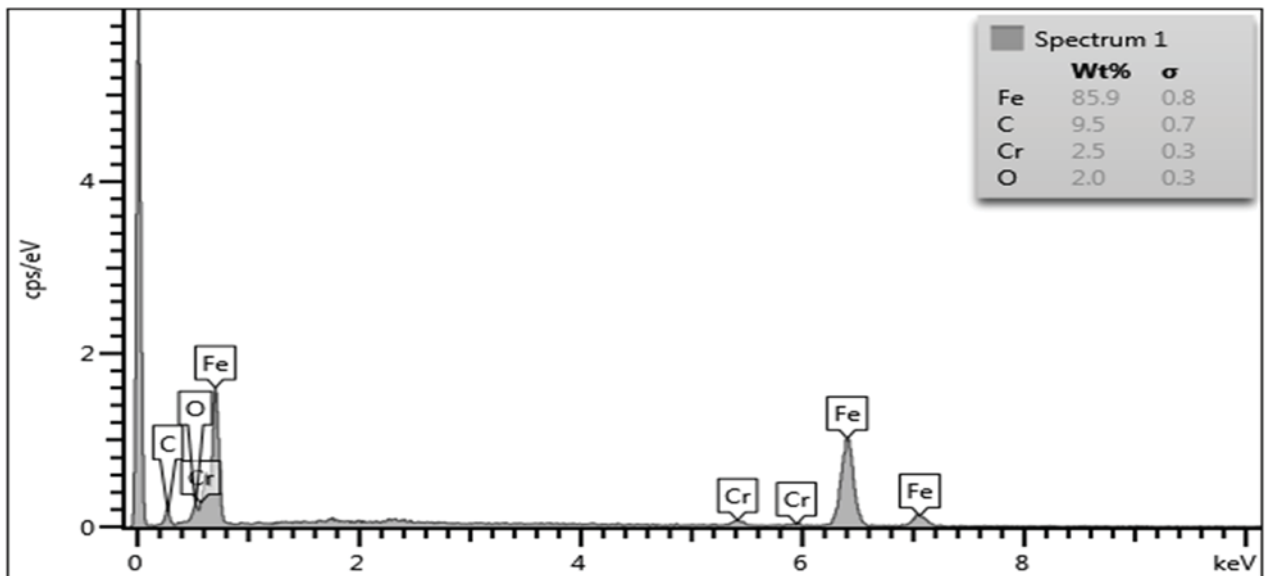


Figure 75: WM analysis in Spectrum 1 was from unaffected WM

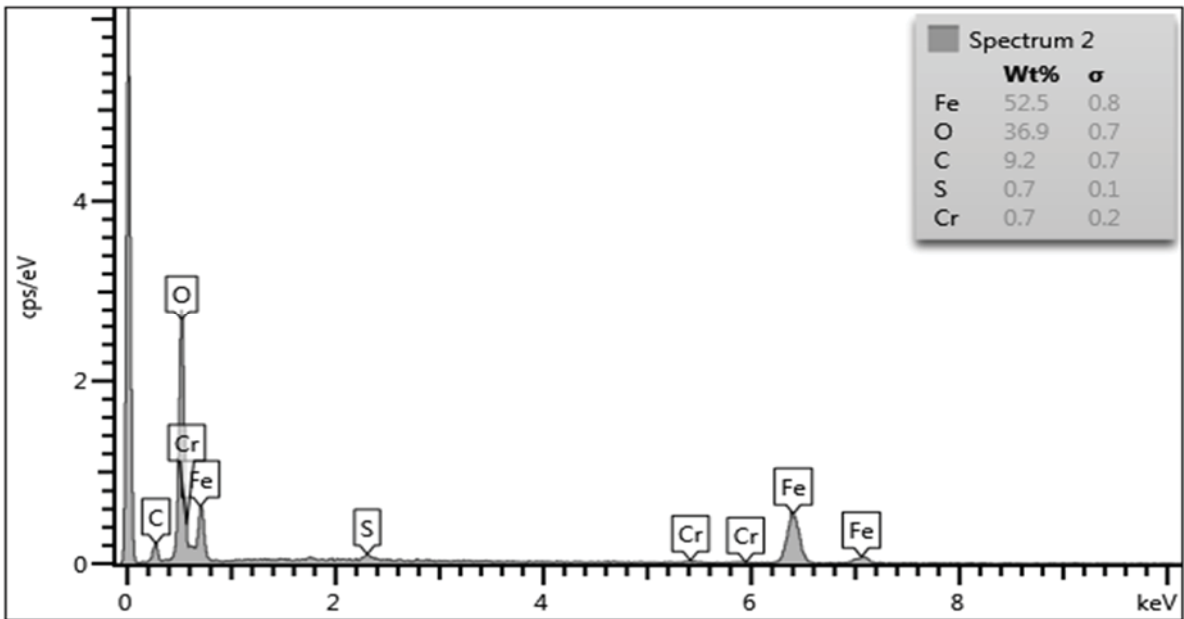


Figure 76: In Spectrum 2, a significant decrease can be observed in Cr and Fe and an increase in oxygen content

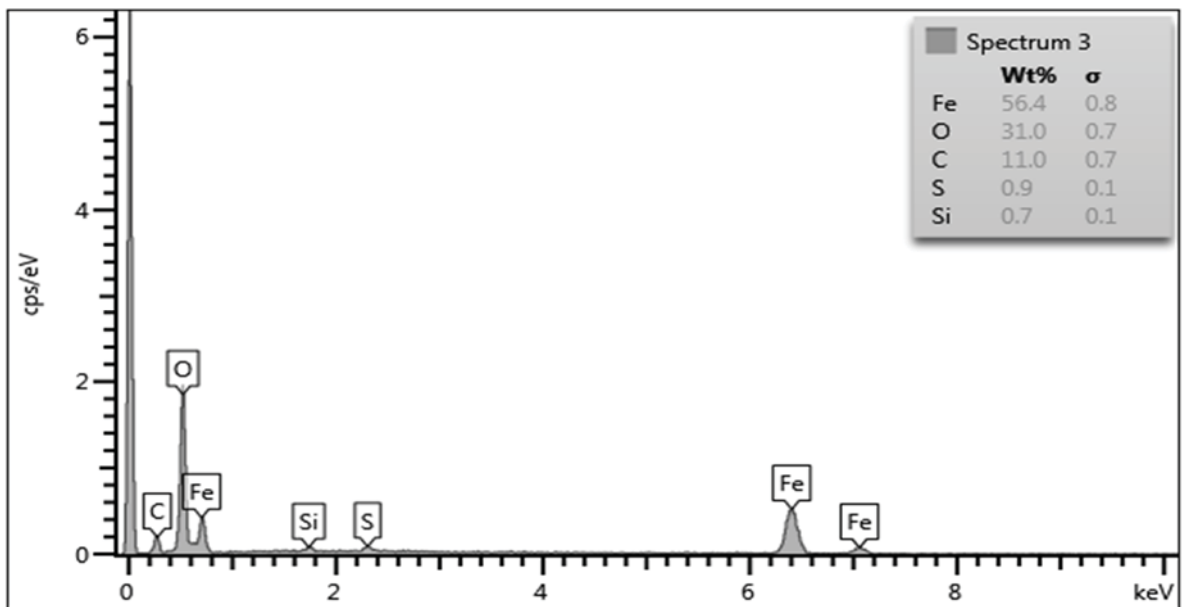


Figure 77: In Spectrum 3, a significant decrease is observed in Cr and Fe, and also an increase in oxygen and carbon for the E9018 consumable

5 DISCUSSION

5.1 Tensile testing

The aim of the tensile test was to measure the yield and tensile strength in the all-weld and the transverse direction of the weld. The yield and tensile strength were used to evaluate and compare the measured Von Mises residual stress in Section 5.3 in the WM.

5.1.1 Transverse tensile strength

The transverse tensile strength results are set out in Table 25. There were no significant differences in yield and tensile strength for two identical samples from the E6013, E7018, E7018-PWHT, E8018 and E9018 welded joints respectively. The tensile properties of the SA 516 Gr 70 BM was similarly stable.

Tensile test coupons machined transversely to welded joints, was fabricated with E7018, E8018 and E9018 electrodes, failing in the BM, away from the HAZ. It is expected that failure will occur at the lowest tensile strength. In this case, the failure was in the BM. The welding also did not affect the mechanical properties, thus the BM mechanical properties defined the tensile strength of the sample, machined transverse to the welded joint. The low elongation of the tensile samples, machined transverse to the welded joint, was likely owing to the difference in the strength of the BM and WM.

The E6013 failed in the WM owing to a weld defect. There were slag inclusions in the weld (Figure 78).

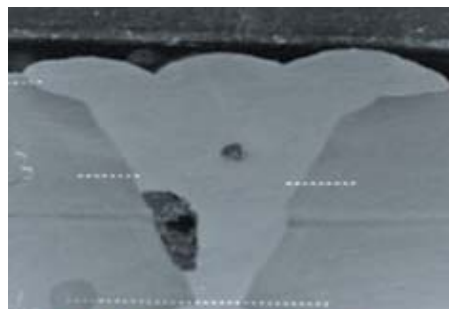


Figure 78: Slag inclusion in the WM that resulted in the failure of the E6013 sample, causing lower tensile strength

The E7018-PWHT sample failed in the WM; the WM did not contain any visible defect. There was a reduction of 15 MPa in tensile strength after the PWHT was applied. The tensile strength is lower than the E7018, E8018 and E9018. It was expected that the tensile strength and yield strength would be lower after a PWHT.

5.1.2 All-weld tensile strength

The tensile strength increased as the specified filler metal strength increased. The E6013, E7018 and E8018 tensile strength was according to the AWS 5.1 and 5.5 specifications [22], [75]. The all-weld tensile strength of the E9018 deposit was 110 MPa higher than the maximum specified tensile strength (Table 33). As expected, there was an increase in tensile strength of the electrodes, mainly because of the addition of alloying elements such as chromium and molybdenum.

It is specified by AWS 5.5 that the E9018 and E8018 welds should be subjected to a PWHT at 690°C for one hour. The excessive tensile and yield strength can be accredited owing to the absence of a PWHT and the presence of the alloying elements. This does not affect the conclusions of this study, since hardness and residual stress were measured in the as-welded condition. From the discussed literature, a PWHT will reduce hardness and residual stress [47], [74], [75].

Table 33: The E9018 minimum (all-weld) specified tensile strength according to AWS 5.5 in the stress relieved condition vs the actual yield strength and tensile strength [22]

Sample	Yield strength [MPa]	Tensile strength [MPa]
E9018 actual welded sample	660	830
E9018 maximum specified value	530	720

In Figure 79, the yield strength of the E8018 electrode was marginally lower than the E7018 WM; this was an unexpected result.

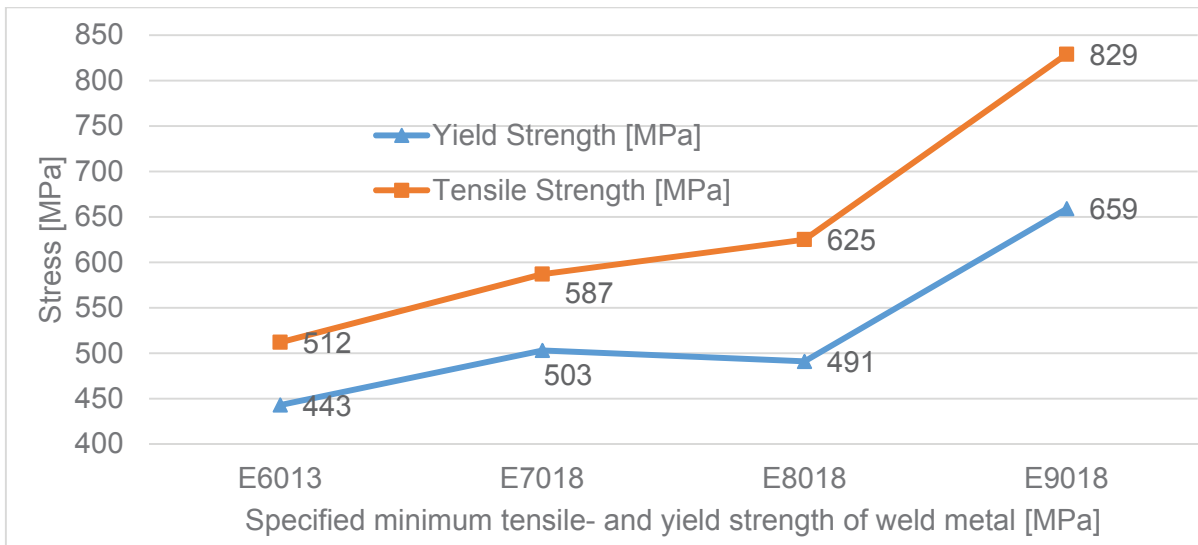


Figure 79: The WM yield strength and tensile strength of the E6013, E7018, E8018 and E9018 welded samples

5.1.3 Summary of observations on tensile test results

- Due to the failure position in the BM, the WM strength did not affect the yield and tensile strength of the transverse tensile test coupons. The only exceptions were the E6013 that failed owing to a defect in the weld, and the E7018-PWHT that failed in the WM
- It was unexpected that the yield strength decreased from the E7018 to the E8018 electrodes. The obtained yield strength was consistent with the residual stress measured (Section 5.4).

5.2 Impact testing

5.2.1 Weld metal toughness

The E6013 sample had an average impact strength of 47 J (Table 27), below the manufacturer's minimum of 70 J. Rutile electrodes predominantly have lower average impact strength owing to the high oxygen content, although it was still below the specified limit. The low impact strength of the E6013 WM was likely caused by the presence of slag inclusions (Figure 81). The E7018, E8018 and E9018 electrode samples exhibited various toughness, which can be expected, since the chemical composition was not the same.

5.2.2 Heat-affected zone toughness

The impact strength in the HAZ is noted in Table 27; there were some variations in the HAZ impact strength. This will be discussed in Section 5.3, in consort with the interrelationship with hardness. The HAZ impact strength of the E6013 welded joint was significantly lower (63 J) than the corresponding value of welded joints, fabricated using E7018, E8018 and E9018 electrodes.

5.2.3 The effect of post-weld heat treatment on the impact strength of the E7018-1 welded joint

The E7018 WM had an impact strength of 324 J compared to 250 J of the E7018-PWHT sample. There was a decrease of 70 J in the WM's impact strength. The as-welded WM structure (Figure 61) mainly consisted of AF. The stress relieving PWHT resulted in grain growth (Figure 64) indicates the WM structure after PWHT). Subsequent to the grain growth, the hardness and the impact strength decreased during the PWHT of E7018 WM.

The average value for the HAZ's impact strength in the E7018 electrode was 233 J compared to the E7018-PWHT samples' average of 242 J. A slight increase in impact strength after the PWHT was therefore achieved. It is expected from the literature that there will be an increase in impact strength in the HAZ [47].

Summary of observations on impact strength in the weld metal and heat-affected zone

- The E7018 electrode's WM had a higher impact strength than the E8018 and E9018 WM. The higher impact strength is assumed to be attributable to a formation of a fine grain structure (Figure 61) with a tensile strength lower than the E8018 and E9019 (Figure 62 and Figure 63)
- The 7018-PWHT electrode resulted in an increase in the HAZ's impact strength, relative to the as-welded E7018 electrode joint. The increase in impact strength of the HAZ during the PWHT was associated with a decrease in hardness (Figure 51)

- The E7018-PWHT had a decrease in WM impact strength. This decrease was likely owing to the coarsening of GF during PWHT. The comparison is illustrated in Figure 61 and Figure 64.

5.3 Hardness of the heat-affected zone and weld metal

5.3.1 Weld metal hardness in the E6013, E7018, E8018 and E9018 electrodes

A summary of the top, middle, bottom, average and maximum weld hardness measured in the samples in the WM are indicated in Table 34. It was expected that as the electrode's minimum specified tensile strength increased, their hardness would increase [78].

Table 34: The average hardness of the WM for the top, middle and bottom measurements

Position	Weld metal hardness of electrode in HV ₁₀			
	E6013	E7018	E8018	E9018
Top	168	182	229	313
Centre	178	190	247	341
Bottom	185	205	229	298

The average hardness for the E6013 electrode in the WM was 177 HV₁₀, with the hardest point as 193 HV₁₀. The WM hardness was well below the maximum specified hardness of 210 HV₁₀, as noted in NACE SP0472:2015 [8].

The E7018 results are indicated in Figure 43; the average hardness was 193 HV₁₀, with the highest hardness of 208 HV₁₀ in the WM. The average hardness before the PWHT in the WM was close to the limit of the NACE SP0472:2015 of 210 HV₁₀. The last pass in the WM (top) had a lower hardness, which may be as a result of the last pass at a higher interpass temperature, causing a lower hardness in the WM. This was consistent in all four samples.

The E8018 hardness test results are indicated in Figure 44. The E8018 WM hardness exceeded the NACE SP0472:2015 limit (210 HV₁₀ and 200 HB) with an average WM

hardness of 235 HV₁₀ (224 HBN). The values were converted to Brinell and compared with the hardness results of Kotecki and Howden in Section 5.7 [29].

The E9018 electrode’s hardness results are indicated in Figure 45. The average hardness in the weld was 317 HV₁₀ that is 298 HBN, with the highest hardness of 366 HV₁₀ (344 HBN). This exceeds the hardness limit in NACE SP0472:2015 of 210 HV₁₀ and the authors Kotecki and Howden of 236 HV₁₀ (225 HB) [29].

5.3.2 Heat-affected zone hardness of the E6013, E7018, E8018 and E9018

The average hardness in the HAZ was compared with the E6013, E7018, E8018 and E9018 electrode’s average HI from Section 3.3.4 (Table 36 and Figure 77). The E6013 electrode indicated a maximum hardness of 280 HV₁₀ (Figure 42). The limit according to the NACE SP0472:2015 is 250 HV₁₀ for the hardness in the HAZ. There was no cracking, despite the maximum hardness exceeding 280 HV₁₀ in the HAZ. In the E7018 electrode sample, the maximum hardness in the HAZ was 220 HV₁₀. The E8018 electrode results observed the highest hardness of 180 HV₁₀ (Figure 44). The maximum hardness in the E9018 electrodes sample was 212 HV₁₀ for the welded joint.

Table 35: Average hardness in the HAZ of the E6013, E7018, E8018 and E9018 electrodes

Sample	E6013	E7018	E8018	E9018
Hardness HV ₁₀ in the HAZ	252	220	180	212

The HAZ hardness was inconsistent in the samples. There was a reduction in the HAZ’s hardness as the HI increased (Figure 80). This is consistent with EN 1011 [24], increasing the HI results in a longer Δt_{8-5} , resulting in a lower hardness. It was proven that the high HAZ’s hardness of the E6013 welded joint was associated with a HI of 0.54 kJ/mm. The last passes at the top and in the root had lower average HI’s resulting in a higher hardness in the HAZ. The effect of the PWHT on the E7018 electrode’s sample will be discussed in Section 5.3.3.

Table 36: The average HI used for each sample compared with the average hardness in the HAZ

	E6013	E7018	E7018-PWHT	E8018	E9018
Average Method A	0.54	0.89	0.89	1.13	0.73
Average Method B	0.53	0.51	0.51	0.83	0.61
Average of A and B	0.54	0.60	0.60	0.98	0.67
Average HV ₁₀ in the HAZ	252	220	185	180	212

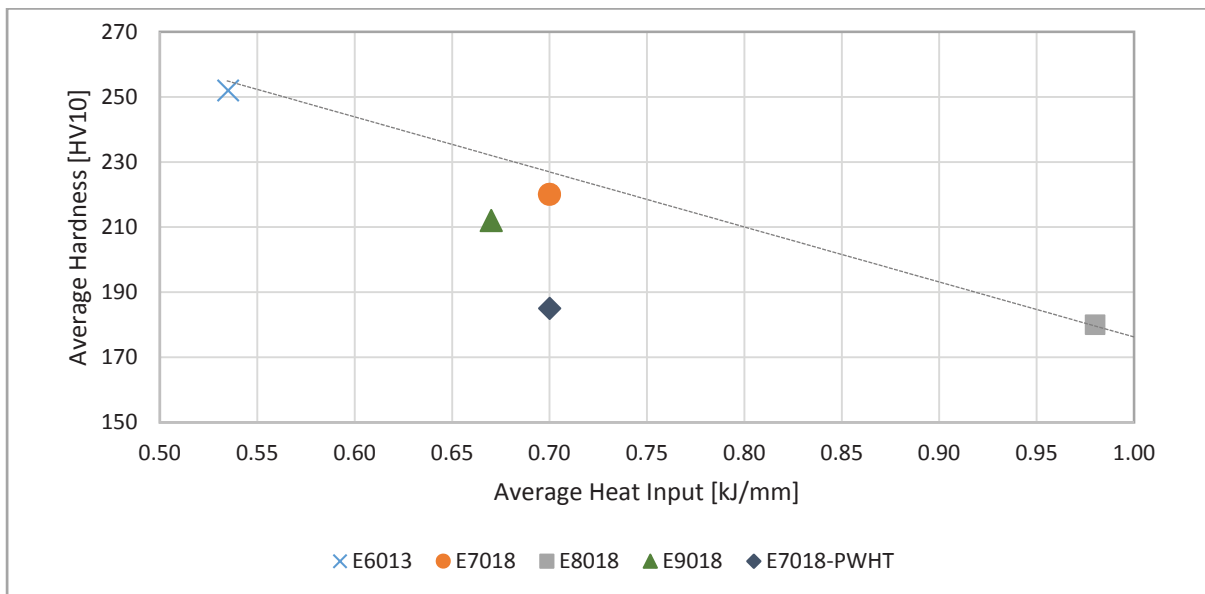


Figure 80: Average hardness after the last run (capping) in the HAZ, compared with the average HI

5.3.3 Comparison of the E7018 and E7018-PWHT weld metal and heat-affected zone's hardness

In Figure 49-Figure 51, the average change in the WM hardness during the PWHT was 7-10 HV₁₀ units. The most significant changes were in the HAZ where the hardness changed with 20-66 HV₁₀ units. It is expected from the literature that the PWHT will reduce the hardness. This data corresponds with the earlier work of Kotecki and Howden discussed in this study [29]. They reported a larger change in hardness in the HAZ and little change in the WM. The average change in hardness was calculated in the top, middle and root pass. The results are illustrated for the top, middle and bottom pass in Table 37 and Table 38.

Table 37: Hardness of the E7018 and E7018-PWHT in the WM and heat-affected zone

Position	E7018	E7018-PWHT
WM - TOP	189	178
WM - MID	164	148
WM - BOT	202	178
HAZ - TOP	172	150
HAZ - MID	154	133
HAZ - BOT	212	186

Table 38: Hardness reduction of the PWHT sample in the top, middle and bottom runs of the E7018-PWHT sample

	Position	Top	Middle	Bottom
Number of measurements		22	14	17
Minimum	Weld metal	0	8	2
Maximum	Heat-affected zone	27	25	63

5.3.4 Summary of hardness observations

- The WM hardness was increased by increasing the electrode strength.
- The PWHT resulted in a minor change in hardness in the WM, but significant changes in the HAZ. This corresponded with the published results.
- The maximum hardness allowed in the WM by NACE SP0472:2015 was exceeded in the E8018 and E9018 electrodes.
- The WM hardness of the E8018 electrode was similar to the hardness measured by Kotecki and Howden, where cracking started [29].
- A higher interpass temperature resulted in a lower hardness in the final passes in the WM.
- A low HI resulted in a high hardness in the HAZ of both the cap and root run (top and bottom).
- In the HAZ of the E6013 electrode sample, the maximum hardness allowed by NACE SP0472:2015 was exceeded.

5.3.5 Tensile strength and hardness

In Figure 81, the transverse and all-weld tensile specimens' tensile strengths are plotted against the equivalent BS 7910:2013 [79]. This calculates the tensile strength as a function of hardness for the following:

BM:

$$\sigma_U = 3.3 HV_{10} - 8$$

WM:

$$\sigma_U = 3 HV_{10} + 22.1$$

The average hardness's in the BM and WM were used to calculate the expected tensile strength (Table 39 and Table 40).

Table 39: The average transverse tensile test hardness was calculated at the region of failure to calculate the expected tensile strength. In most samples, failure occurred in the BM, while the E6013 failed in the WM, owing to a defect

Series	Average hardness of failure location [HV ₁₀]	Tensile strength calculated from average hardness at failure location according to BS 7910:2013 [MPa]	Actual tensile strength [MPa]
E6013	180	586	455
E7018	148	480	511
E8018	151	490	516
E9018	149	484	516
E7018-PWHT	145	471	497
SA 516 Gr 70	141	457	490

Table 40: Average hardness in the WM used to calculate the expected tensile strength

Series	Average weld metal hardness [HV ₁₀]	Tensile strength calculated from average weld metal hardness according to BS 7910:2013 [MPa]	Actual tensile strength [MPa]
E6013	177	553	512
E7018	192	598	587
E8018	235	727	625
E9018	317	973	829

In Table 39, it was illustrated that a close relationship existed between the predicted and the actual tensile strength if the sample had failed in the BM. Only the E6013 coupon deviated owing to the defect in the weld.

In the all-weld tensile strengths in Table 40, the E6013 coupon (despite the defect) and the E7018 coupon was close to a 1:1 ratio, while the E8018 and E9018 coupons deviated from each other. The WM in both the E8018 and the E9018 consumables was mainly comprised of Acicular Ferrite and Bainite that resulted in high tensile strength. The increase of alloying elements such as chromium and molybdenum results in the formation of Acicular Ferrite and Bainite.

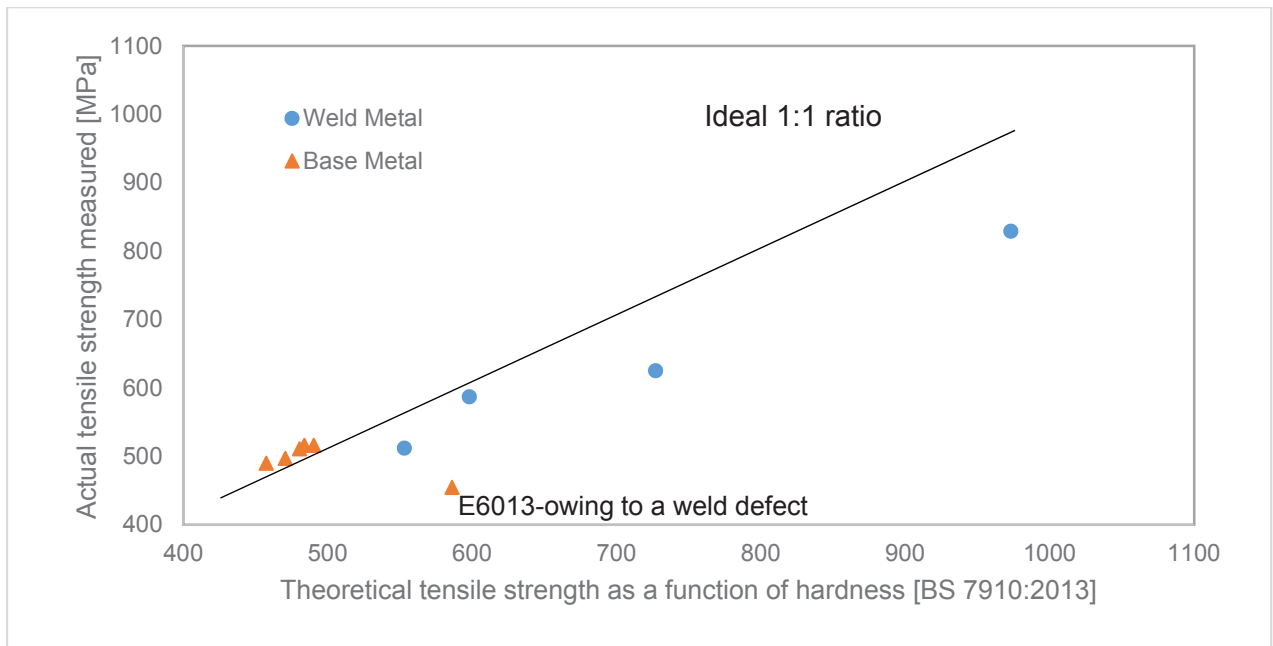


Figure 81: The actual tensile strength was measured and compared to the tensile strength as a function of hardness at the failure position, according to BS7910:2013. These were performed for transverse and all-weld samples. The E6013 coupon's value deviated owing to a defect

5.3.6 The relationship between toughness and hardness

Weld metal

Table 41 and Figure 83 indicates the relationship between the WM's impact strength and the WM hardness for the five electrodes.

The E6013 rutile electrodes exhibited deficient impact and a low average hardness. As stated, rutile coverings mostly exhibit lower impact strength because of their higher oxygen content.

The E7018 coupon indicated a reduction in hardness and impact strength in the WM after the PWHT. Higher hardness's were observed in the E8018 and E9018 WMs, which was an expected result. The E8018 and E9018 electrodes are used when welding creep resistant steels. It was expected that there will be fluctuations in the WM impact strength, since differing filler metal strengths were used. Impact toughness was, as expected, lower in the as-welded E8018 and E9018 WM owing to alloying of Cr and Mo, resulting in a higher hardness than the E7018 electrode, causing a lower

ductility. The PWHT of E7018 WM resulted in grain growth of GF, reducing impact strength.

The coupons of the basic electrodes (E7018, E7018-PWHT, E8018 and E9018) had the highest average impact strength and hardness compared to the rutile electrode that had deficient impact strength and hardness properties.

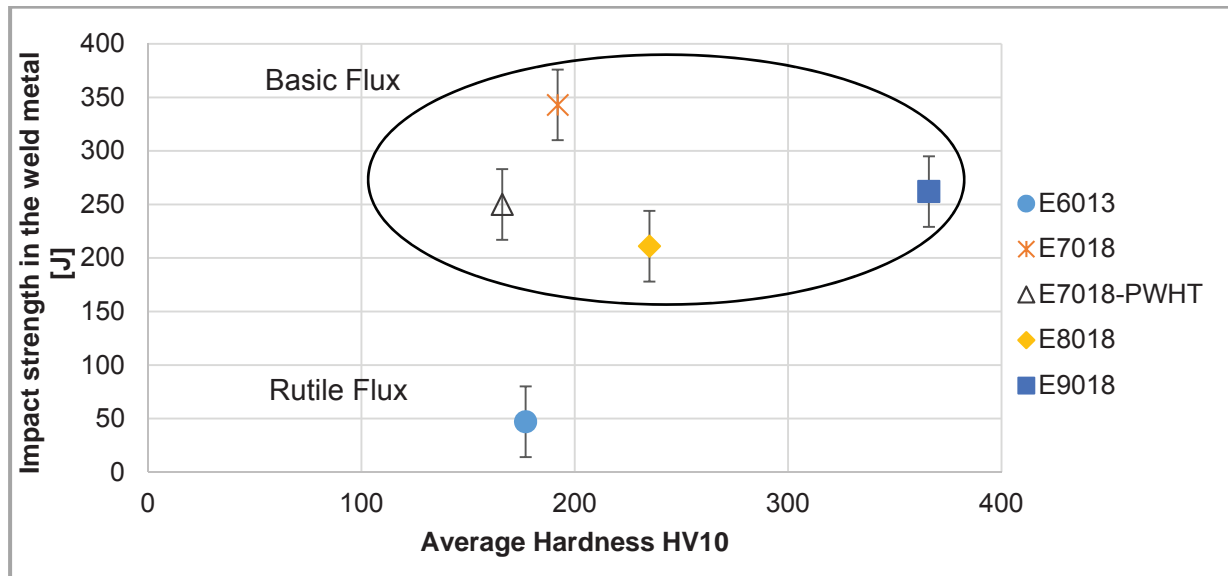


Figure 82: Impact toughness of the WM compared to the hardness of the WM

Table 41: Average impact strength of the WM compared with the average hardness in the WM

Sample	Impact toughness in J	Hardness HV ₁₀
E6013	47	177
E7018	343	192
E7018-PWHT	250	166
E8018	211	235
E9018	262	366

Relationship between hardness and toughness in the heat-affected zone

Figure 83 and Table 42 indicates the relationship between toughness and average hardness in the HAZ. From all the tested samples, the E6013 sample had deficient toughness in the HAZ. The average hardness in the HAZ for the E6013 was 252 HV₁₀. The low impact is associated with excessive high hardness and Widmanstätten Ferrite

and large grain's in the HAZ. The average HI was considerably lower than the other samples (Figure 56).

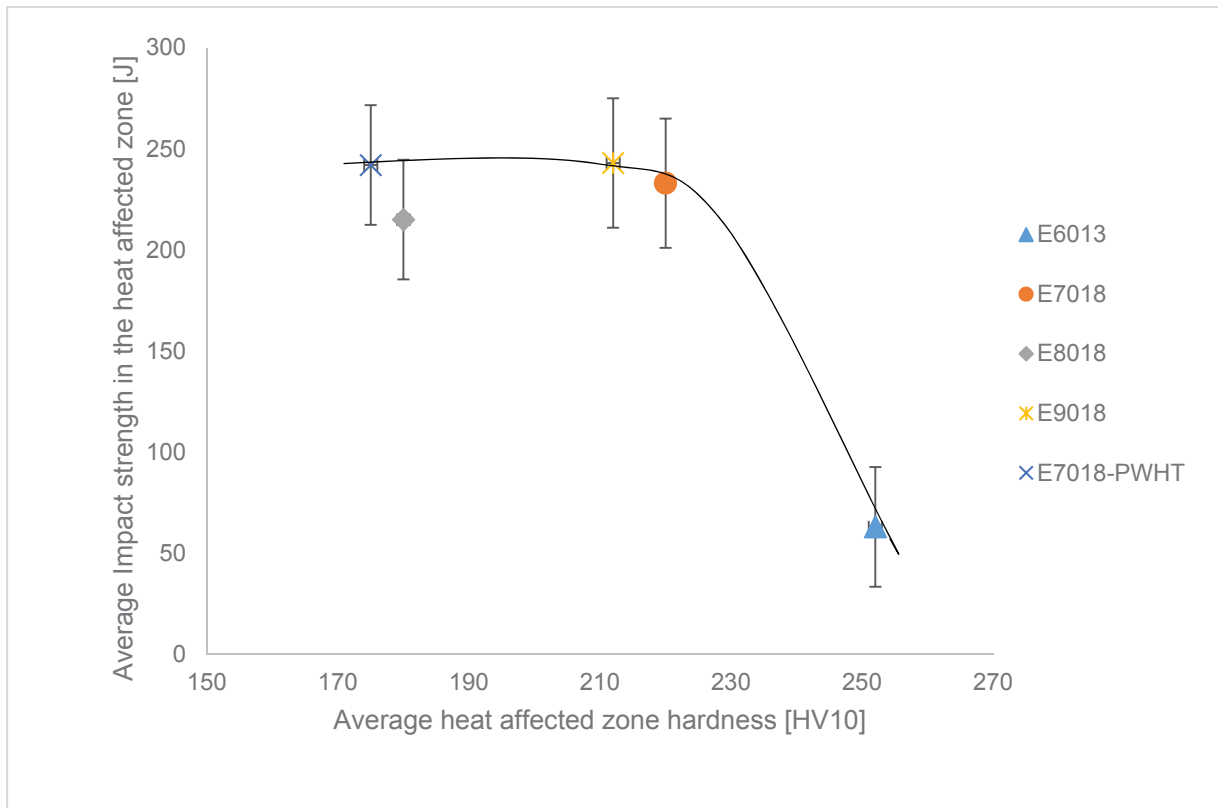


Figure 83: Average impact strength in the HAZ was compared with the average hardness in the HAZ

Table 42: Impact toughness in the HAZ compared to the maximum hardness

Electrode	Impact toughness in the heat-affected zone [J]	Hardness in the heat-affected zone HV ₁₀
E6013	63	252
E7018	233	220
E8018	215	180
E9018	243	212
E7018-PWHT	242	175

5.4 Residual stress

The aim of the study was to change the weld hardness by increasing the electrode strength and measuring the residual stress in the welded area. The coordinate system used is indicated in Figure 84.

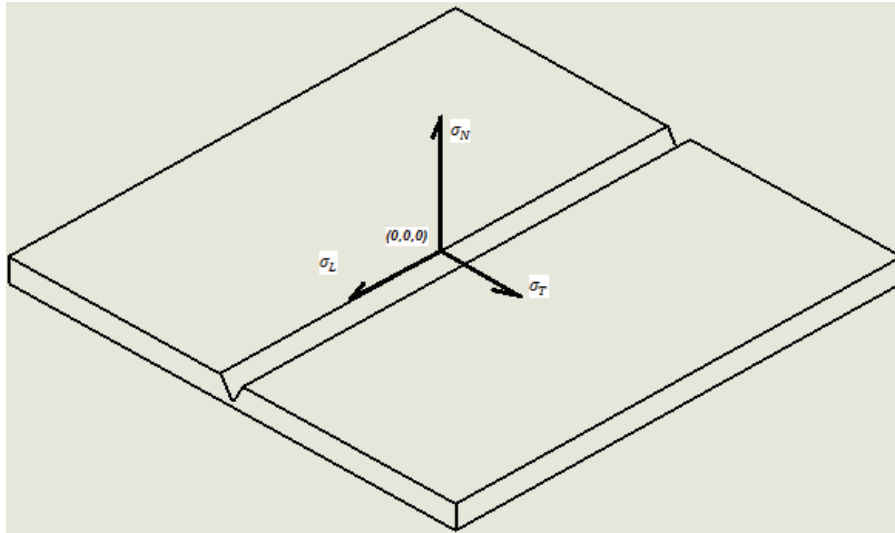


Figure 84: The coordinate system used for the measurement of residual stress. The axis is at intercept (0, 0, 0) in the normal, longitudinal and transverse directions

5.4.1 Summary of observations on the residual stress

Normal stress

Of the three components, the normal stress is consistently the lowest in all the samples, illustrating a plane stress situation.

Longitudinal stress

In all the samples, the WM had a large tensile residual stress in the longitudinal direction. The E7018, E8018 and E9018 (619 MPa, 558 MPa, and 686 MPa respectively) had the largest peaks in the middle of the weld at a depth of 8.31 mm. It was also observed that the maximum longitudinal stress is close to the centreline.

Transverse stress

The transverse residual stress fluctuated in no particular order in the WM. The one side is compressive while the rest is tensile. At various depths the residual stress was compressive or tensile in the WM. The largest stress was close to the root at 11.45 mm.

5.4.2 Von Mises Stress in weld metal

To evaluate the magnitude of the triaxial residual stress, the Von Mises criterion was applied to the mesh using the normal, longitudinal and transverse components. Table 43 indicates the results of the calculated Von Mises Stress for welded joints, fabricated using the E7018, E8018 and E9018 electrodes.

Table 44 indicates that no stress exceeds the yield strength.

In the calculation below, an example is indicated of the E7018 at position 0 mm, depth 8.31 mm. At this position, the normal residual stress was 46 MPa, the longitudinal residual stress was 495 MPa, and the transverse residual stress was -45 MPa, giving a Von Mises Stress of 501 MPa:

$$\begin{aligned}\text{Resultant stress}_{E7018,0\text{ mm}} &= [\sigma_N^2 + \sigma_L^2 + \sigma_T^2 - (\sigma_N\sigma_L + \sigma_N\sigma_T + \sigma_T\sigma_L)]^{\frac{1}{2}} \\ &= [(46)^2 + (495)^2 + (-45)^2 - (46 \times 495 + (46 \times -45) + (-45 \times 495))]^{\frac{1}{2}} \\ &= 501 \text{ MPa}\end{aligned}$$

The residual stress decreased rapidly in the WM as the distance increased from the centreline. The measured yield strength was compared to the maximum residual stress in

Table 44 in the all-weld tensile specimens, after the Von Mises Stress criterion was applied.

Table 43: The calculated Von Mises residual stress for principal stresses, using the normal, longitudinal and transverse components

Von Mises residual stress in the weld metal [MPa]						
Sample	Distance along weld [mm]	-8	-4	0	4	8
E7018	2.1	403	466	460	461	278
	5.2	377	472	490	427	291
	8.31	336	468	501	420	281
	11.45	357	435	485	408	289
	14.52	354	435	457	355	326
E8018	2.1	396	395	284	363	338
	5.2	348	482	451	405	318
	8.31	316	467	473	335	289
	11.45	333	428	384	352	344
	14.52	319	385	402	381	338
E9018	2.1	332	435	400	291	255
	5.2	326	345	333	300	284
	8.31	311	481	635	395	312
	11.45	304	530	555	404	273
	14.52	288	234	401	463	273

Table 44: The yield strength of the filler metal, compared with the maximum residual stress measured at each level when the Von Mises failure criteria were applied

	E7018	E8018	E9018
yield strength measured in all-weld specimens [MPa]	503	491	686
Depth [mm]	Maximum stress by Von Mises failure Criteria [MPa]		
2.1	466	396	435
5.2	490	482	345
8.31	501	473	635
11.45	485	428	555
14.52	457	402	463

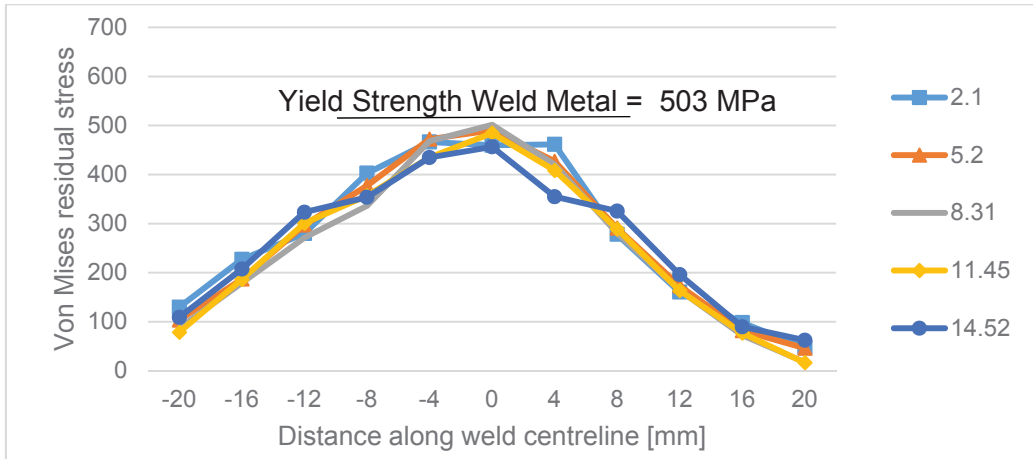


Figure 85: The E7018 resultant residual stress calculated at varied depths below the top surface. The maximum stress does not exceed the yield strength of the WM

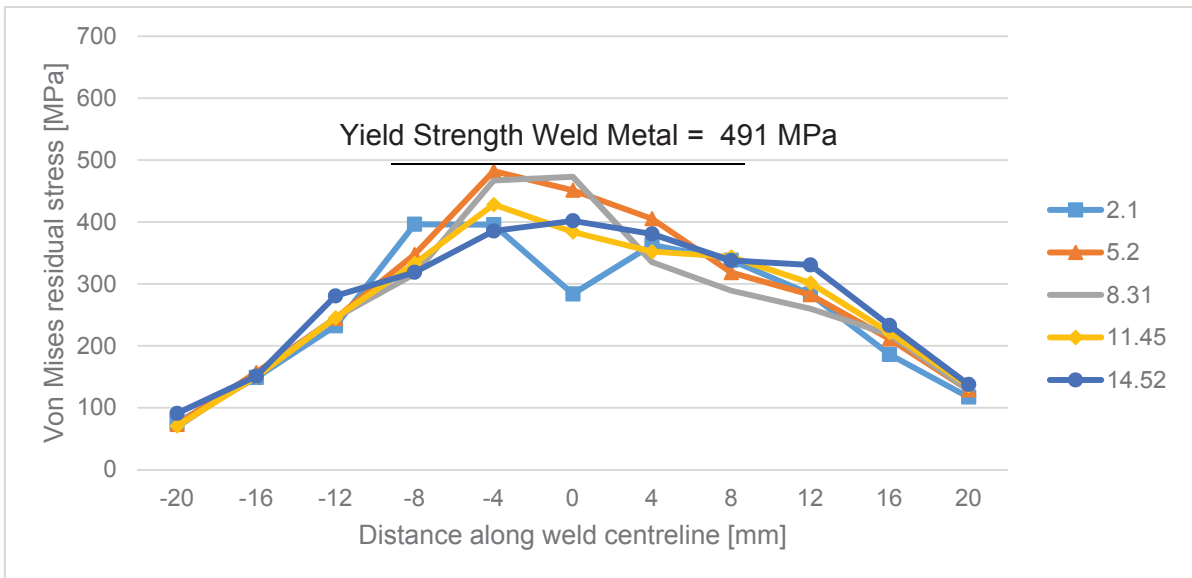


Figure 86: The E8018 welded sample's resultant residual stress calculated at depths 2.1, 5.2, 8.31, 11.45 and 14.52 mm

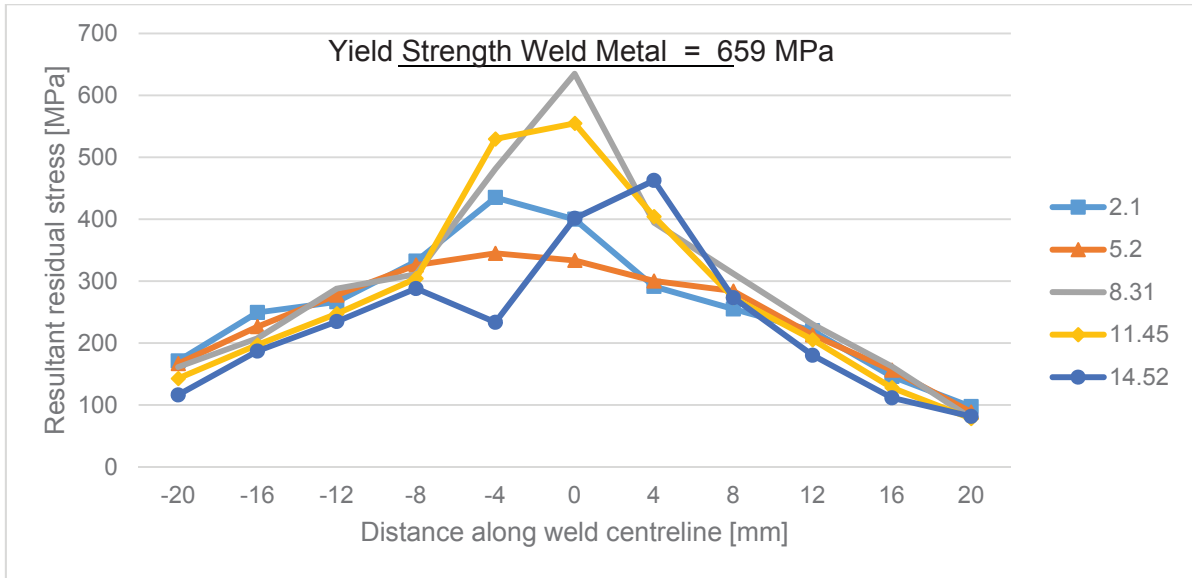


Figure 87: The E9018 welded samples' resultant residual stress calculated at depths 2.1, 5.2, 8.31, 11.45 and 14.52 mm.

Figure 85-Figure 87 indicated that the maximum measured residual stress in the WM was comparable to the yield strength. In Table 45, it was indicated that the Von Mises residual stress was invariably between 96-99.6% of the actual yield strength in the WM (in the as-welded condition).

Table 45: The yield strength of the all-weld tensile specimens used to compare the maximum yield strength to the magnitude of the Von Mises residual stress in the WM

Sample	Yield strength [MPa]	Max Stress measured as from Von Mises [MPa]	Ratio: Stress _{VM} / yield strength [%]
E7018	503	501	99.6
E8018	491	473	96.3
E9018	659	635	96.4
E7018-PWHT*	173	114	65.9

*The E7018-PWHT sample's yield strength is taken at the stress relieving temperature of 600°C.

As stated in the literature study, the residual stress magnitude may be up to the yield strength of the WM. The resultant stress was also the largest in the middle of the thickness, with lower a stress on the outside surfaces. In the welded region, it is in tensile.

5.4.3 Effect of a post-weld heat treatment on weld residual stress

In Figure 88, there was a significant drop in residual stress after the PWHT. It was expected from the literature study that a reduction in residual stress will occur after a PWHT was applied [47], [48]. The PWHT was performed at a temperature of 600°C for two hours.

Table 46: The resultant residual stress in MPa, calculated by the Von Mises theorem in the E7018-PWHT coupon

Direction	Position [mm]	-8	-4	0	4	8
E7018-PWHT	2.1	26	41	63	20	39
	5.2	17	51	34	32	16
	8.31	21	61	114	56	16
	11.45	23	66	89	79	18
	14.52	72	102	88	54	40

This can be attributed to creep strain in the WM generated during the PWHT. The WM yield strength is significantly lower, resulting in the strain at an elevated temperature. The E7018 electrode coupon did not contain any Cr or Mo alloying elements, increasing the strength at elevated temperature. It is therefore expected that it will have a significant reduction during the PWHT in residual stress.

In Figure 88, the E7018 graph and the E7018-PWHT Von Mises residual stress were compared to illustrate the drop in stress after a PWHT was applied. In the plate welded, using an E7018 electrode, the PWHT performed at 600°C for two hours resulted in a reduction in the Von Mises residual stress from 480 MPa to 84 MPa, a reduction of 83% (Table 47).

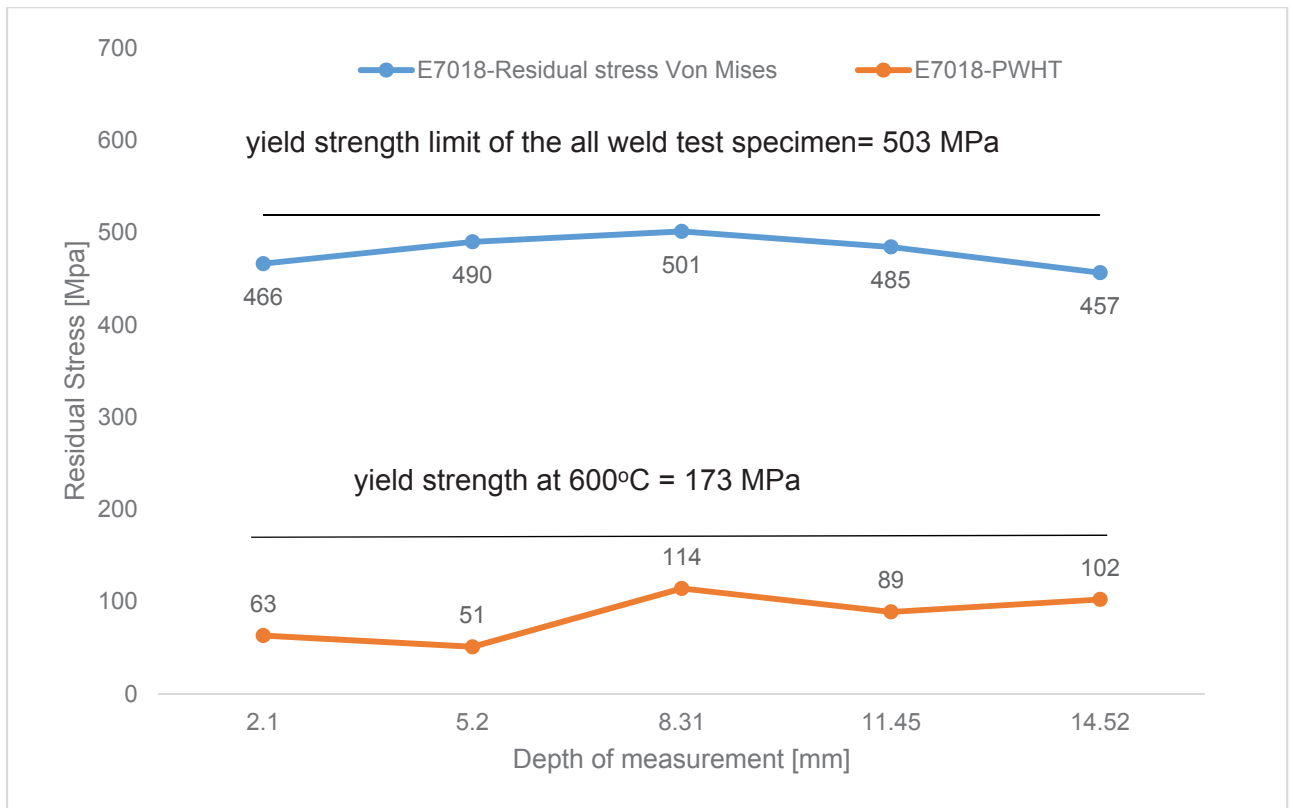


Figure 88: Maximum resulting residual stress at separate depths in the WM, compared to the all-weld residual stress of the E7018 welded coupon and compared to the E7018-PWHT coupon

Table 47: The resultant residual stress of the E7018, compared to the E7018-PWHT at various depths below the top surface of the weld. The average residual stress is also reported

Depth [mm]	E7018	E7018-PWHT
2.1	466	63
5.2	490	51
8.31	501	114
11.45	485	89
14.52	457	102
Average residual stress [MPa]	480	84

5.4.4 Calculation of the minimum expected residual stress in the weld metal as a function of the preheat temperature

From the previous sections in this study, the residual stress in the WM is close to the yield strength. An increase in preheat temperature (T_i) will result in a longer cooling time Δt_{8-5} and this will affect the hardness and the residual stress. This can be illustrated from the basic calculation when a thermal stress is induced.

$$\sigma = E\alpha\Delta(T_f - T_i)$$

It may therefore be possible to reduce the residual stress by increasing the preheat temperature. This is evaluated in the following section and compared with the measured residual stress results.

The API 579-1 [80] calculates the expected minimum yield strength as a function of temperature for certain steels at room temperature. It is calculated by the following formula:

$$\sigma_{YS} = \sigma_{YS}^{room\ or\ preheat\ temperature} \cdot exp[C_0 + C_1T + C_2T^2 + C_3T^3 + C_4T^4 + C_5T^5]$$

Where:

σ_{YS} = Expected yield strength

σ_{YS}^{Actual} = Actual Yield Strength

T = exposure at elevated temperature

Material		C ₀	C ₁	C ₂	C ₃	C ₄	C ₅
Carbon Steel **	1	3.79E-02	-1.86E-03	6.69E-06	-1.83E-08	2.32E-11	-1.23E-14
1.25Cr-0.5Mo 2.25Cr-1Mo **	2	3.38E-02	-1.74E-03	8.33E-06	-2.11E-08	3.30E-11	-2.69E-14

**The E7018 electrode is in group 1, while the E8018 and E9018 electrodes are in group 2.

By supplementing the preheat temperature value into the equation, the expected minimum yield strength can be calculated for the associated preheat temperature. This was performed to observe the effect on residual stress when the preheat temperature was increased.

As an example, the minimum expected yield strength was calculated at 75°C for the E7018 welded sample, where the preheat temperature was concluded. The minimum expected yield strength of 488 MPa was below the actual yield strength of 503 MPa. The expected minimum yield strength for the E7018, E8018 and E9018 as a function of preheat temperature is illustrated in Table 48:

$$\begin{aligned}\sigma_{YS} &= \sigma_{YS}^{room\ temperature} \cdot \exp[C_0 + C_1T + C_2T^2 + C_3T^3 + C_4T^4 + C_5T^5] \\ &= 503 \text{ MPa} * \exp[C_0 + C_1x75 + C_275^2 + C_375^3 + C_475^4 + C_575^5] \\ &= 488 \text{ MPa}\end{aligned}$$

Table 48: The expected minimum yield strength (σ_{YS}) at room temperature as a function of temperature, in this case the preheat temperature. The emphasised line represents the preheat temperature where this study occurred

Preheat temperature [°C]	σ_{YS} 'E7018 [MPa]	σ_{YS} 'E8018 [MPa]	σ_{YS} 'E9018 [MPa]
25	499	486	652
50	476	466	618
75	454	446	585
100	434	427	554
125	414	409	525
150	395	391	497
175	377	375	471
200	360	359	446
225	343	344	422
250	328	329	400
275	313	315	379
300	299	302	359
325	285	289	340
350	272	277	322
375	260	265	305
400	248	254	289

In Table 49, the actual yield strength was compared to the minimum expected yield strength according to the API 579 standard for the E7018, E8018 and E9018 welded coupons. The actual yield strength always exceeded the minimum yield strength, as could be expected.

Table 49: The actual yield strength compared to the minimum expected yield strength at 75°C (where the preheat temperature was obtained) for various electrodes

Sample	Actual yield strength [MPa]	Minimum expected yield strength calculated at 75°C [MPa]	Largest Von Mises Residual stress [MPa]
E7018	503	454	501
E8018	491	446	473
E9018	659	585	635

In Figure 89, the minimum expected yield strength was plotted as a function of the preheat temperature. The yield strength is reduced as the preheat temperature is increased. This was performed to estimate the minimum expected residual stress in the WM as a function of the preheat temperature. Note that this is only an estimate of the minimum expected residual stress in the WM; it was clear that the maximum residual stress will be higher than calculated.

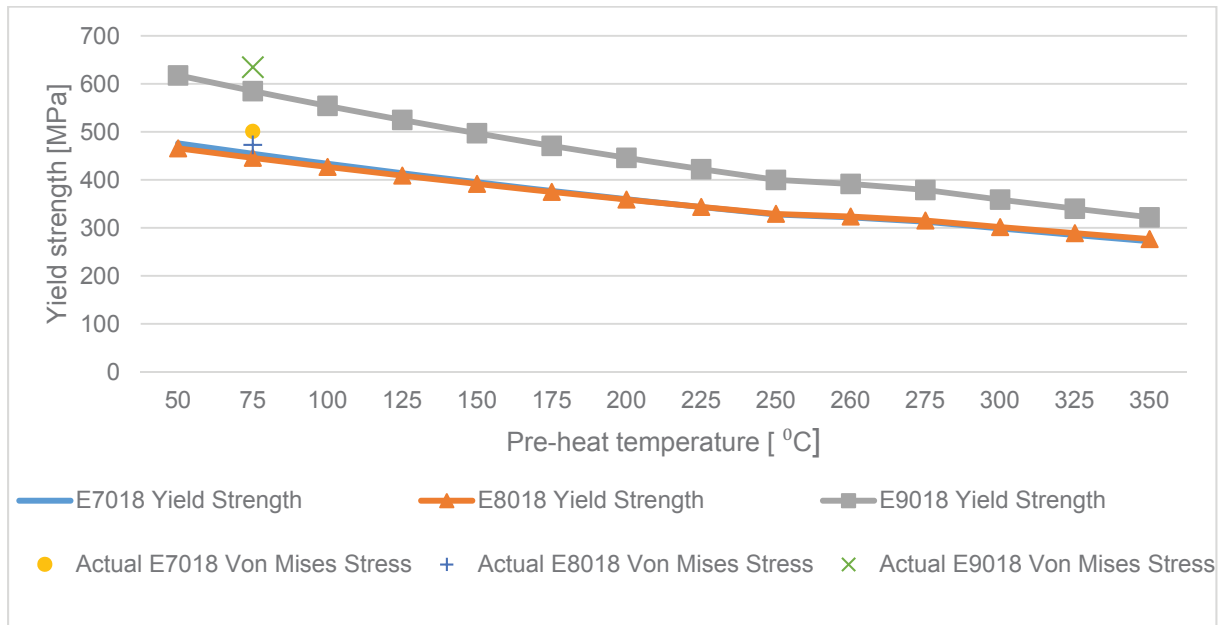


Figure 89: The estimated effect of an increase in preheat temperature on the minimum expected yield strength. The residual stress is close to the yield strength. As the temperature increases, there is a decrease in the minimum yield strength, therefore a decrease in residual stress

5.4.5 Summary on the interpretation of residual stress measurements

- The Von Mises residual stress in the BM did not surpass the yield strength of the BM at room temperature.
- The largest stress was in the middle of the WM, at a depth of 8.31 mm, close to the weld centreline.
- The API 579 calculation of minimum expected yield strength as a function of preheat temperature indicated that as the preheat temperature increased, the minimum yield strength will decrease; consequently, the residual stress will also decrease. Note that this is only an estimation.

- After the PWHT was applied there was a significant drop in the residual stress. The predominant residual stress relief mechanism during the PWHT can be attributed to creep strain at elevated temperatures.

5.5 Metallography

In Figure 90, the BM samples of SA 516 Gr 70 is illustrated, before and after the PWHT was performed. There was some spheroidising in the base material during the PWHT at 600°C for two hours.

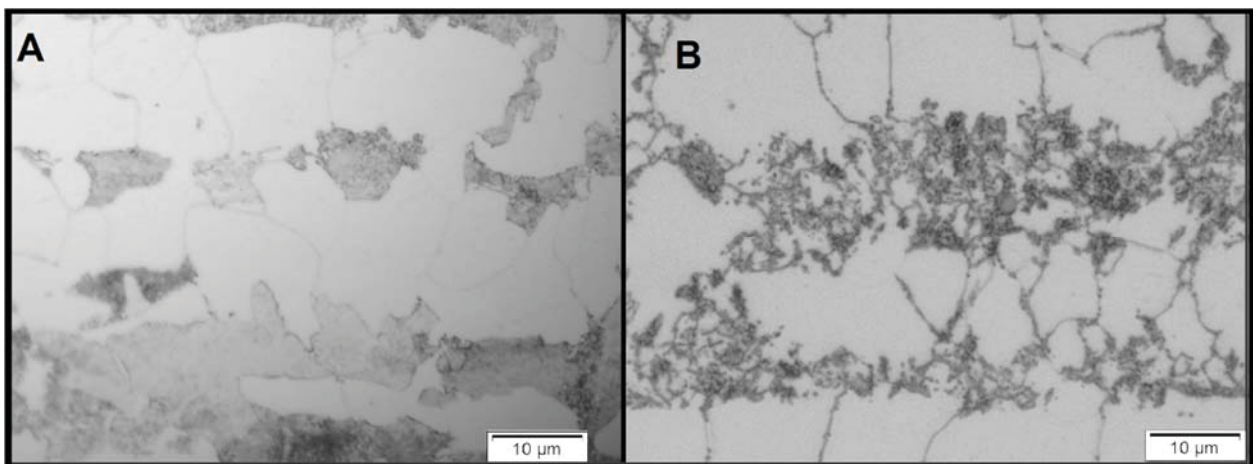


Figure 90: A) The E7018 pearlite and ferrite content at 1000x magnification. B) The E7018-PWHT sample, where spheroidising of the pearlite is evident

5.6 Susceptibility to cracking

The aim of the corrosion test was to investigate the interrelationship of hardness and residual stress in a corrosive environment. As stated, the hardnesses were increased by increasing the electrode strength.

5.6.1 Base metal cracking

The BM was susceptible to HIC in the BM (SA 516 Gr 70). All samples had cracks in the BM (E6013, E7018, E8018 and E9018) in Figure 67-Figure 71.

In samples E7018 and E9018, the cracks were larger than the maximum acceptance criteria. Most of the cracks were in the middle of the through-thickness in the rolled direction. Apart from the cracks that formed in the middle of the through-thickness, the cracks were in the BM, well away from the weld and the HAZ. The cracks in the through-thickness followed stepwise cracking. It is usually accepted that HIC cracking of carbon steels in a H₂S-containing environment has a stepwise morphology [81].

5.6.2 Weld metal cracking

The only sample that cracked by SCC in the WM was the E9018 coupon (Figure 72). The WM crack opened at the surface and progressed to the middle. High quantities of oxygen were present in the corrosion product. In some areas, an increase in carbon content was observed (Spectrum 3 in Figure 77). The corrosion product is highly likely to be iron carbonate (FeCO₃). This chemical species was observed by authors when investigating iron sulphide/carbonate layers in H₂S [82].

It is assumed that the crack originated on the outer surface and progressed into the centre of the weld where the tensile stress was the highest (Figure 72). The Von Mises residual stress was 400 MPa at the sub-surface area, while the Von Mises residual stress in the middle was 635 MPa (average Von Mises Stress).

The WM hardness of the E8018 and E9018 samples exceeded the hardness limit specified by the NACE SP0472 of 210 HV₁₀. The E8018 sample did not crack with an average hardness of 235 HV₁₀, which is 25 HV₁₀ harder than the limit. The E9018 sample cracked as expected, with the average WM hardness of 317 HV₁₀. This is ± 110 HV₁₀ over the limit of the NACE SP0472 specification of 210 HV₁₀.

The results from this study were converted in Table 50, and plotted and compared with the data of Kotecki and Howden in Figure 91. From the results, the conclusion is that the samples cracked above a hardness of 236 HV₁₀ (225 BHN). Current results from SMAW were therefore consistent with earlier reported data on SAW [29]. The E8018 did not crack with an average WM hardness of 235 HV₁₀ (224 HBN). This corresponded with the results from Kotecki and Howden.

Table 50: Average WM hardnesses from this study was converted to Brinell hardness. This was compared with the results that Kotecki and Howden obtained in their study as in Figure 91 [29].

Hardness unit of measurement	E6013	E7018	E8018	E8019
Average WM hardness- HV ₁₀ (as reported)	177	192	235	317
Average WM hardness- Brinell (converted using ASTM E 140)	169	183	224	303

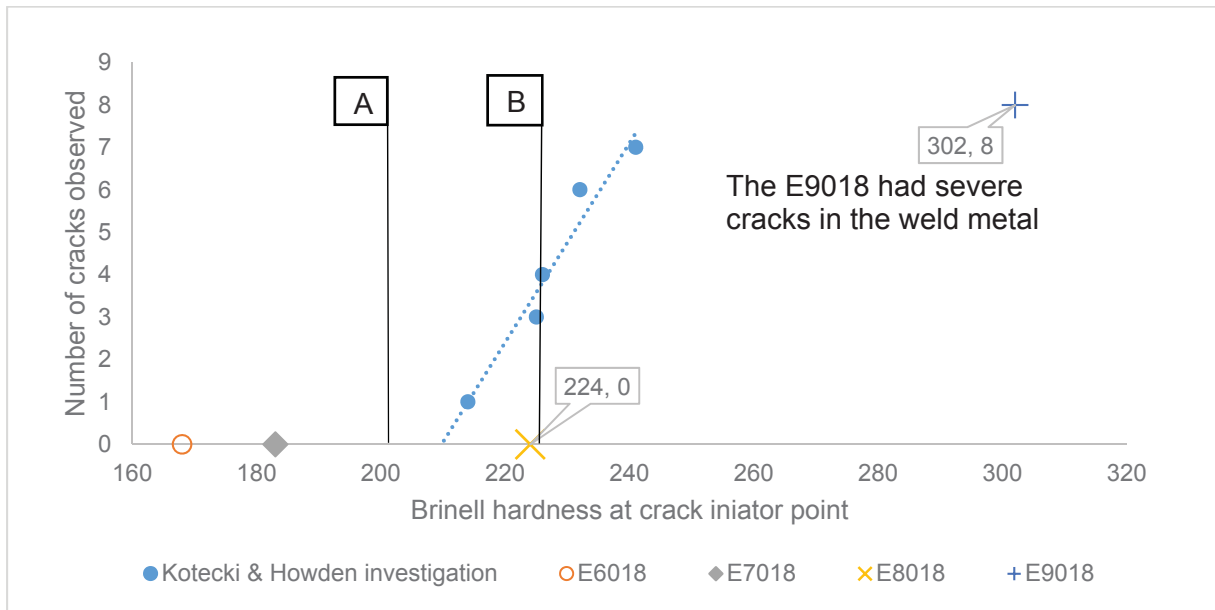


Figure 91: Data from the E7018, E8018, and E9018 coupons compared to the results of Kotecki and Howden [29]. The E9018 sample cracked severely. The results were converted to Brinell. The hardness limit, according to the NACE SP0472 of 200 HB, is illustrated by A. The highest WM hardness that did not crack, determined during current study, is illustrated by B

6 CONCLUSIONS

This investigation set out to study the interrelationship of hardness and residual stress on SCC. The following conclusions were drawn on the test results.

6.1 Tensile test

There was an increase in WM tensile strength and WM hardness, as the specified minimum tensile strength of the electrode increased. The yield strength did not necessarily increase with the increase of electrode strength. The E8018 (80 ksi) electrode with an actual yield strength of 491 MPa was lower than the yield strength of the E7018 (70 ksi) weld deposit of 503 MPa. The yield strength was consistent with measured residual stress.

The PWHT of the E7018-1 weld deposit resulted in a marginally lower tensile strength and yield strength. As a result, the transverse E7018-PWHT sample failed in the WM, not in the BM as the E7018 sample.

6.2 Impact testing

- The WM's impact strength of a rutile electrode was extremely deficient, even lower than the manufacturer specified in the WM, owing to a slag inclusion defect.
- The SCC behaviour was thought not to be related to impact strength. The low impact strength of the E6013 WM was considered not to have an influence on the results of the study.
- Basic electrodes indicated higher average impact strength than the rutile electrodes, caused by fast cooling slag and an oxygen increase in the rutile slag.
- There was a significant increase in impact strength in the HAZ after a PWHT was performed. This was consistent with previous results.

6.3 Hardness of weld metal and heat-affected zone

Low HIs with the final passes, for example the capping of the top and in the root, lead to high hardness in the HAZ. The hardness limit of the NACE SP 0472 was exceeded

in the E6013 HAZ. Applying a PWHT to an E7018-1 deposit reduced the maximum hardness in the HAZ from approximately 204 to 183 HV₁₀.

6.4 Residual stresses

- It was indicated by the Von Mises theorem that the residual stresses did not exceed the yield strength of the WM.
- The largest Von Mises residual stress was consistently in the centre of the through-thickness of the weld sample at a depth of 8.31 mm on the WM.
- The Von Mises peak stress was consistently in the middle of the sample, between the stop start in the longitudinal position.
- Applying a PWHT of 600°C for two hours on an E7018 welded joint resulted in a reduction of the Von Mises residual stress from 480 MPa to 82 MPa. The predominant stress relieving mechanism is creep.
- The average residual stress was lower in the E8018 (80 ksi) compared to the E7018 (70 ksi), consistent with the actual yield strength of the filler metal.
- Increasing the preheat temperature will result in a lower average residual stress.

6.5 Stress-corrosion cracking

The E8018 sample exceeded the NACE SP0472:2015 hardness limit, but not the limit of Kotecki and Howden; subsequently, there was no SCC [29]. The E9018 sample was the only sample where SCC occurred. The maximum WM hardness of the E9018 welded joint exceeded the hardness limit in the NACE SP 0472 of 210 HV₁₀ and that of Kotecki and Howden of 236 HV₁₀.

The results therefore indicated that the WM hardness of 210 HV₁₀ (200 BHN) specified by the NACE SP0472:2015 is overtly conservative. Subsequently, if hardness is below the specified limit, cracking will not occur, irrespective of weld residual stress up to the yield strength of the WM.

6.6 Summary

This study set out to investigate the relationship of WM hardness and residual stress susceptibility to SCC of carbon steel welds in a hydrogen sulphide environment. As the nominal filler metal strength increased, WM hardness, electrode strength and consequently, residual stress increased. Residual stress levels were consistent with the measured all-weld yield strength. Kotecki and Howden used welded SAWs to establish that cracking will occur above 225 HBN. In addition, the NACE SP 0472 limits the hardness in the WM and HAZ to 210 HBN and 248 HV respectively.

Current results of differential hardness welded by the SMAW were indicated to be consistent with these results (Figure 91). Within the NACE SP0472 hardness limitation, carbon steel welds will not be susceptible to SCC, despite tensile residual stresses close to magnitude of the yield strength of the filler metal.

High preheat temperatures and interpass temperatures are beneficial for carbon steel welds intended for sour service. This results in a reduction in hardness in both the weld and the HAZ. In addition, it is required by the NACE SP0472 to control the hardness. Basic calculations show that there may be a reduction in residual stress.

7 LIMITATIONS AND SHORTCOMINGS

In this dissertation, there were several limitations and shortcomings.

7.1 Samples

In this study, a total of 250 kg of steel was used for the manufacture of the samples. For this particular test, there were three samples for each welding electrode (E6013, E7018, E8018 and E9018). There was one extra plate that underwent a PWHT. Despite the initial design and planning, there were still too few test samples for the mechanical testing. There was only one corrosion test sample for each series.

The E6013 sample's residual stress was not measured, owing to the presence of a defect in the WM. A stress concentration in the WM (owing to the defect) would have resulted in a change to the residual stress. It should have been re-welded, but because of a time constraint at that stage in the study, it was omitted. In retrospect, this should have been given more attention.

7.2 Process

The only process used in the study was SMAW. In the manufacturing environment, multiple processes and combinations of welding processes are used, such as SAW and tungsten inert welding.

7.3 Heat input

Although the HI was kept as close as possible for the various results in the BM, there were significant differences in the HAZ's properties of the E6013 electrode. The low HI used when welding with the E6013 electrodes caused a higher cooling rate in the HAZ, a high hardness and lower impact strength than that achieved with other electrodes. It therefore indicates that a pWPS or WPS should be followed rigorously during fabrication. With future work, a more mechanised approach will be followed to ensure constant HI for multi-pass welds.

7.4 Residual stress

Samples were heavily constrained to keep deformation to an absolute minimum to maximise the residual stress. The measurements represent residual stress of constrained samples. Without the constraint, the residual stress would have been much lower. It is uncertain what the magnitude of residual stress will be if it is unconstrained. It is likely that shear stress was present as a result of the clamped samples. Only tensile residuals stresses has an influence on SCC, hence no consideration was given to the shear stresses. It is also worthy to note that XRD should have been employed to measure the residual stress (in the plane stress condition) at the surface of the sample and combined with current results, since SCC initiates on the surface condition.

7.5 Stress-corrosion cracking

The initial corrosion tests were designed to test the hardness stress limitation with a “cracked” and “not cracked” result. In retrospect, additional samples should have been welded with the various consumables. For instance, an E6013, E7018, E8018 and E9018 could have been welded with high and low HI simulating differential hardness and residual stress within the electrode, in consort with a set that underwent a PWHT. Furthermore, shorter samples could have been welded and interval testing could have been implemented at increments on separate days to establish when cracking initiated. These samples could have been included in the stress-corrosion study at varying intervals to determine a crack initiation relationship with hardness.

8 PROPOSED RESEARCH

In this study, the residual stress was measured at different depths of the welded samples. There were some peaks aligned at the different depths as a result of multi-pass welding. The variables were too numerous to establish if there was a consistent pattern in the formation of residual stress. Future work may involve measuring the changes in residual stresses during welding and the effect of various weld preparations on residual stress during multi-pass welds.

The main consequence of preheating is to control the microstructure's hardness in the base metal and the HAZ. The study focus was on the hardness limitation with its relationship to residual stress. Earlier work indicated that, with an increase in preheat temperature, there was a decrease in the calculated residual stress [43]–[45]. SCC in H₂S environments may be reduced by using higher preheat temperatures or always applying a PWHT. This will result in a softer HAZ and a lower average residual stress. Future work can test if a PWHT can be replaced with high preheat temperatures in carbon steels for thick components.

REFERENCES

- [1] S. Shipilov, R. Jones, J.-M. Olive, and R. Rebak, in *Environment-Induced Cracking of Materials, Volume 1 - Chemistry, Mechanics and Mechanisms*, Elsevier, 2008.
- [2] L. Garverick, in *Corrosion in the Petrochemical Industry*, ASM International, 1994.
- [3] G. Linnert, *Metallurgy Second Edition Welding Metallurgy*. 2003.
- [4] C. L. Jenney and A. O'Brien, *Welding Handbook, Volume 1 - Welding Science and Technology (9th Edition)*. American Welding Society (AWS), 2001.
- [5] G. Totten, M. Howes, and T. Inoue, in *Handbook of Residual Stress and Deformation of Steel*, ASM International, 2002.
- [6] K. A. Macdonald, in *Fracture and Fatigue of Welded Joints and Structures*, Woodhead Publishing, 2011.
- [7] A. C. on M. of Inspection, in *Welding Inspection Handbook (3rd Edition)*, American Welding Society (AWS), 2000.
- [8] NACE SP0472, "NACE SP0472-2010 : Methods and Controls to Prevent In-service Environmental Cracking of Carbon Steel Weldments in Corrosive Petroleum Refining Environments," 2010.
- [9] Nace TM0177, *TM0177-96 Standard Test Method Laboratory Testing of Metals for Resistance to Sulfide Stress Cracking and Stress Corrosion Cracking in H₂S Environments*, no. 21212. 2005.
- [10] B. L. Bramfitt and A. O. Benscoter, in *Metallographer's Guide - Practices and Procedures for Irons and Steels*, ASM International, 2002.
- [11] A. Cottrell, in *Introduction to Metallurgy (2nd Edition)*, Maney Publishing for IOM3, the Institute of Materials, Minerals and Mining, 1975.
- [12] R. W. J. Messler, in *Joining of Materials and Structures - From Pragmatic Process to Enabling Technology*, Elsevier, 2004.
- [13] L. E. Samuels, in *Light Microscopy of Carbon Steels*, ASM International, 1999.
- [14] J. F. Lancaster, in *Metallurgy of Welding (6th Edition)*, Woodhead Publishing, 1999.
- [15] G. Krauss, in *Steels - Processing, Structure, and Performance (2nd Edition)*, ASM International, 2015.
- [16] K. Easterling, *Introduction to the Physical Metallurgy of Welding*. Elsevier, 2013.

- [17] R. A. Higgins, in *Engineering Metallurgy - Applied Physical Metallurgy (6th Edition)*, Elsevier, 1993.
- [18] E. Oberg, F. D. Jones, H. L. Horton, and H. H. Ryffel, in *Machinery's Handbook (28th Edition) & Guide to Machinery's Handbook*, Industrial Press, 2008.
- [19] A. Paradowskaa and J. Price, "The effect of heat input on residual stress distribution of steel welds measured by neutron diffraction," *J. Achiev. Mater. Manuf. Eng.*, 2006.
- [20] K. Lorenz, "Evaluation of Large Diameter Pipe Steel Weldability by Means of the Carbon Equivalent," in *International Conference on Steels for Linepipe and Fittings*, 1981
- [21] T. Kasuya, M. Okumura, and N. Yurioka, "Methods for predicting maximum hardness of heat-affected zone and selecting necessary preheat temperature for steel welding," *Nippon Steel Technical Report*.
- [22] A5.5/A5.5M, *Specification for Low-Alloy Steel Electrodes for Shielded Metal Arc Welding: (AWS A5.5/A5.5M:2006)*. American Welding Society (AWS), 2006.
- [23] W. T. Becker and R. J. Shipley, in *ASM Handbook, Volume 11 - Failure Analysis and Prevention*, ASM International, 2010.
- [24] BS EN 1011 Part 1 and 2, "Welding. Recommendations for welding of metallic materials," 2000.
- [25] M. Stewart and O. T. Lewis, in *Pressure Vessels Field Manual - Common Operating Problems and Practical Solutions*, Elsevier, 2013.
- [26] G. Desjardins and R. Sahney, "post weld heat treatment (PWHT) Page," in *Encyclopedic Dictionary of Pipeline Integrity*, Clarion Technical Publishers, 2012.
- [27] J. L. Dossett and G. E. Totten, in *ASM Handbook, Volume 04A - Steel heat Treating Fundamentals and Processes*, ASM International, 2013.
- [28] P. Heating and S. Relieving, "Postweld Heat Treatment," *Weld. Innov.* 16.1, vol. XV, no. 2, 1998.
- [29] D. Kotecki and D. Howden, "Submerged-Arc-Weld Hardness and Cracking in Wet Sulfide Service," *WRC Bull.*, 1973.
- [30] E. J. Hearn, in *Mechanics of Materials, Volume 2 - An Introduction to the Mechanics of Elastic and Plastic Deformation of Solids and Structural Materials (3rd Edition)*, Elsevier, 1997.
- [31] C. L. Jenney and A. O'Brien, in *Welding Handbook, Volume 1 - Welding Science*

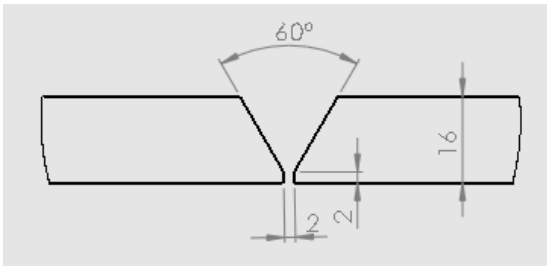
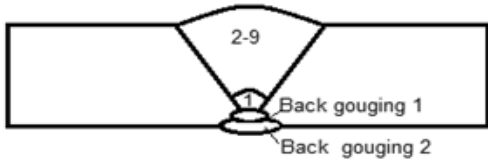
- and Technology (9th Edition)*, American Welding Society (AWS), 2001.
- [32] R. H. Leggatt, "Residual stresses in welded structures," *Int. J. Press. Vessel. Pip.*, vol. 85, no. 3, pp. 144–151, Mar. 2008.
- [33] N. S. Rossini, M. Dassisti, K. Y. Benyounis, and A. G. Olabi, "Methods of measuring residual stresses in components," *Mater. Des.*, vol. 35, pp. 572–588, Mar. 2012.
- [34] P. J. Withers and H. K. D. H. Bhadeshia, "Residual stress. Part 1 – Measurement techniques," *Mater. Sci. Technol.*, vol. 17, no. 4, pp. 355–365, Apr. 2001.
- [35] ASM Handbook Volume 4: Heat Treating, *ASM Handbook Volume 4: Heat Treating*. 1991.
- [36] A. Raman, in *Materials Selection and Applications in Mechanical Engineering*, Industrial Press, 2007, p. 267.
- [37] G. Totten, M. Howes, and T. Inoue, in *Handbook of Residual Stress and Deformation of Steel*, ASM International, 2002.
- [38] K. H. J. Buschow, R. W. Cahn, M. C. Flemings, B. Ilschner, E. J. Kramer, and S. Mahajan, in *Encyclopedia of Materials - Science and Technology, Volumes 1-11*, Elsevier, 2001.
- [39] G. M. Crankovic and A S M Handbooks, *ASM Handbook, Volume 10:: Materials Characterization. Vol. 10*. A S M International, 1986.
- [40] A. Dibenedetto and M. Aresta, in *Inorganic Micro- and Nanomaterials - Synthesis and Characterization*, De Gruyter, 2013.
- [41] K. Weman, "in *Welding Processes Handbook (2nd Edition)*, Woodhead Publishing, 2012.
- [42] C. Carvalho Silva, J. Teixeira de Assis, S. Philippov, and J. Pereira Farias, "Residual Stress, Microstructure and Hardness of Thin-Walled Low-Carbon Steel Pipes Welded Manually."
- [43] E. Armentani, R. Esposito, and R. Sepe, "The influence of thermal properties and preheating on residual stresses in welding," *Int. J. Comput. Mater. Sci. Surf. Eng.*, 2007.
- [44] T.-L. Teng and C.-C. Lin, "Effect of welding conditions on residual stresses due to butt welds," *Int. J. Press. Vessel. Pip.*, vol. 75, no. 12, pp. 857–864, Oct. 1998.
- [45] M. E. Aalami-Aleagha, M. Foroutan, S. Feli, and S. Nikabadi, "Analysis preheat effect on thermal cycle and residual stress in a welded connection by FE simulation," *Int. J. Press. Vessel. Pip.*, vol. 114–115, pp. 69–75, Feb. 2014.

- [46] T.-L. Teng and C.-C. Lin, "Effect of welding conditions on residual stresses due to butt welds," *Int. J. Press. Vessel. Pip.*, vol. 75, no. 12, pp. 857–864, Oct. 1998.
- [47] ASM international, *ASM handbook: Welding, brazing, and soldering*. ASM International, 1993.
- [48] P. Dong, S. Song, and J. Zhang, "Analysis of residual stress relief mechanisms in post-weld heat treatment," *Int. J. Press. Vessel. Pip.*, vol. 122, pp. 6–14, 2014.
- [49] P. Dong, J. K. Hong, and P. J. Bouchard, "Analysis of residual stresses at weld repairs," *Int. J. Press. Vessel. Pip.*, vol. 82, no. 4, pp. 258–269, Apr. 2005.
- [50] A. G. Olabi and M. S. J. Hashmi, "Stress relief procedures for low carbon steel (1020) welded components," *J. Mater. Process. Technol.*, vol. 56, no. 1–4, pp. 552–562, Jan. 1996.
- [51] B. Chen *et al.*, "In situ neutron diffraction measurement of residual stress relaxation in a welded steel pipe during heat treatment," *Mater. Sci. Eng. A*, vol. 590, pp. 374–383, Jan. 2014.
- [52] H. Alipooramirabad, A. Paradowska, R. Ghomashchi, A. Kotousov, and M. Reid, "Quantification of residual stresses in multi-pass welds using neutron diffraction," *J. Mater. Process. Technol.*, vol. 226, pp. 40–49, Dec. 2015.
- [53] W. Woo, G. B. An, E. J. Kingston, A. T. DeWald, D. J. Smith, and M. R. Hill, "Through-thickness distributions of residual stresses in two extreme heat-input thick welds: A neutron diffraction, contour method and deep hole drilling study," *Acta Mater.*, vol. 61, no. 10, pp. 3564–3574, Jun. 2013.
- [54] S.-H. Kim, J.-B. Kim, and W.-J. Lee, "Numerical prediction and neutron diffraction measurement of the residual stresses for a modified 9Cr–1Mo steel weld," *J. Mater. Process. Technol.*, vol. 209, no. 8, pp. 3905–3913, Apr. 2009.
- [55] R. Budynas and K. Nisbett, *Shigley's Mechanical Engineering Design*. McGraw-Hill Education, 2010.
- [56] B. J. Hamrock, S. R. Schmid, and B. O. Jacobson, *Fundamentals of Machine Elements*. McGraw-Hill Higher Education, 2004.
- [57] B. Lu and J. Luo, "Relationship Between Yield Strength and Near- Neutral pH Stress Corrosion Cracking Resistance of Pipeline Steels—An Effect of Microstructure - 1.3278258," *NACE Int.*, vol. 62, no. 2, p. 12.
- [58] D. A. Jones, *Principles and prevention of corrosion*. Prentice Hall, 1996.
- [59] M. Houle and B. JE, "ASME Section IX : welding qualifications," in *ASME Section IX: Welding qualifications*, 2013.

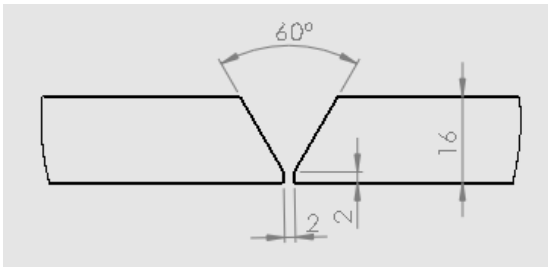
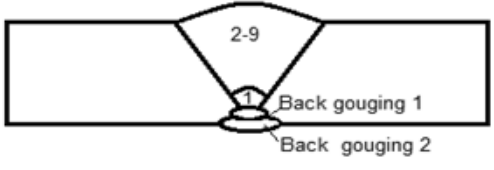
- [60] H. L. Schmeilski and D. R. Gallup, "Factors Affecting Inservice Cracking of Weld Zone in Corrosive Service," 1986.
- [61] R. L. O'Brien, in *Jefferson's Welding Encyclopedia (18th Edition)*, American Welding Society (AWS), 1997.
- [62] S. Kyriakides and E. Corona, in *Mechanics of Offshore Pipelines, Volume I: Buckling and Collapse*, Elsevier, 2007.
- [63] K. Herrmann, "Relationships between Hardness and other Mechanical...", in *Hardness Testing - Principles and Applications*, ASM International, 2011.
- [64] G. F. Vander Voort, *Metallography - Principles and Practice*. ASM International, 1999.
- [65] J. A. Beavers and G. H. Koch, "Limitations of the slow strain rate test for stress corrosion cracking testing," *Corrosion*, vol. 48, no. March, pp. 256–266, 1992.
- [66] B. Isecke, in *Test Methods for Assessing the Susceptibility of Prestressing Steel to Hydrogen Induced SCC: (EFC 37)*, Maney Publishing, 2004.
- [67] R. Baboian, in *Corrosion Tests and Standards: Application and Interpretation (2nd Edition): (MNL 20)*, ASTM International, 2005.
- [68] ASME, *2013 ASME Boiler and Pressure Vessel Code, Section II - Materials*. American Society of Mechanical Engineers, 2013.
- [69] Omega, "Emissivity of Common Materials," *Volume 1 Infrared*, 2003..
- [70] Böhler, "BÖHLER E7018-1," 2013..
- [71] A. P. D. Committee, "5. Classification System for Carbon Steel Electrodes for SMAW...", in *Everyday Pocket Handbook for Shielded Metal Arc Welding (SMAW)*, American Welding Society (AWS), 1998.
- [72] ASTM International, "ASTM A370 - 16 Standard Test Methods and Definitions for Mechanical Testing of Steel Products." 2016.
- [73] ASM international, *ASM Handbook Volume 8: Mechanical Testing and Evaluation*, no. v. 3. 1992.
- [74] ISO, "ISO 15156-3:2015 'Petroleum and natural gas industries -- Materials for use in H₂S-containing environments in oil and gas production -- Part 3: Cracking-resistant CRAs (corrosion-resistant alloys) and other alloys," 2015.
- [75] AWS A5.1/A5.1M, "Specification for Carbon Steel Electrodes for Shielded Metal Arc Welding," 2012.
- [76] ASM International, *ASM Handbook, Volume 04 - Heat Treating*. ASM International, 1991.

- [77] A. G. Olabi and M. S. J. Hashmi, "The effect of post-weld heat-treatment on mechanical-properties and residual-stresses mapping in welded structural steel," *J. Mater. Process. Technol.*, vol. 55, no. 2, pp. 117–122, Nov. 1995.
- [78] E. J. Pavlina and C. J. Tyne, "Correlation of Yield Strength and Tensile Strength with Hardness for Steels," *J. Mater. Eng. Perform.*, vol. 17, no. 6, pp. 888–893, Apr. 2008.
- [79] BS 7910, "Guide to methods for assessing the acceptability of flaws in metallic structures," 2005..
- [80] M. Smith, "Fitness for Service, API 579-1/ASME FFS-1," 2007.
- [81] W. D. Wang, "Ultrasonic Measurement of Mechanical Properties of SA-516-70 Steel in Wet H," in *Volume 7: Operations, Applications, and Components*, 2006, vol. 2006, pp. 315–319.
- [82] W. Sun, S. Nešić, and S. Papavinasam, "Kinetics of Corrosion Layer Formation. Part 2—Iron Sulfide and Mixed Iron Sulfide/Carbonate Layers in Carbon Dioxide/Hydrogen Sulfide Corrosion," *Corrosion*, vol. 64, no. 7, pp. 586–599, Jul. 2008.

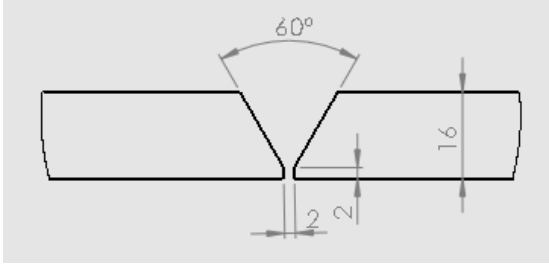
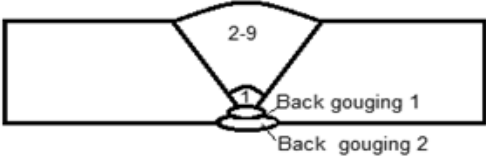
Appendix A

PQR No E6013			
Base Metal			
Material 1	SA 516 gr 70	P-No. Group No	P1
Material 2	SA 516 gr 70	P-No. Group No	P1
Thickness / Type	16 mm Plate	PWHT	None
Filler metal			
Process	SMAW	Filler metal classification	
Process type	Manual	E6013	AWS A5.1
Filler metal trade name 1	Vitemax		
Joint Preparation			
Pre-heat	75		
Prep Method	Thermal cutting, grinding		
Initial Clean	Flapper disk		
Interpass Clean	Wire Brush		
Joint Design		Pass Sequence	
			

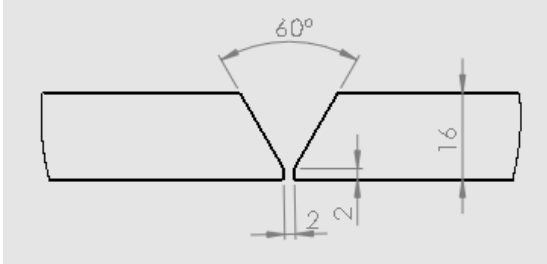
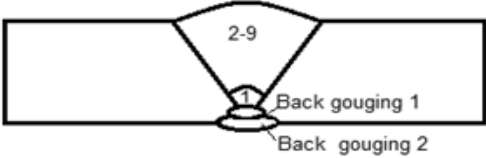
Electrical							
	Electrode size [d]	Travel speed [mm/s]	Amps [I]	Volts [V]	HI [kJ/mm]	Weld Position	Polarity
Run 1	2.15	230	120	12-14	0.5	1G	DC EP
Run 2	3.2	203	123	16-21	0.7	1G	DC EP
Run 3	3.2	207	126	16-21	0.6	1G	DC EP
Run 4	3.2	198	126	16-21	0.7	1G	DC EP
Run 5	3.2	184	126	16-21	0.7	1G	DC EP
Run 6	3.2	194	126	16-21	0.8	1G	DC EP
Run 7	3.2	175	126	16-21	0.8	1G	DC EP
Run 8	3.2	250	126	16-21	0.6	1G	DC EP
Back gouging 1, Run 1	3.2	184	126	16-21	0.7	1G	DC EP
Back gouging 2, Run 2	3.2	276	126	16-21	0.7	1G	DC EP

PQR No E7018			
Base Metal			
Material 1	SA 516 gr 70	P-No. Group No	P1
Material 2	SA 516 gr 70	P-No. Group No	P1
Thickness / Type	16 mm Plate	PWHT	None
Filler metal			
Process	SMAW	Filler metal classification	
Process type	Manual	E7018-1 H8	AWS A5.1
Filler metal trade name 1	Afrox 7018-1		
Joint Preparation			
Pre-heat	75		
Prep Method	Thermal cutting, grinding		
Initial Clean	Flapper disk		
Interpass Clean	Wire Brush		
Joint Design		Pass Sequence	
			

Electrical							
Weld deposit	Electrode size [mm]	Travel speed [mm/s]	Amps [I]	Volts [V]	HI [kJ/mm]	Weld Position	Polarity
Run 1	3.2	224	123	19-24	0.9	1G	DC EP
Run 2	3.2	220	126	19-24	1.0	1G	DC EP
Run 3	4	304	165	19-23	1.1	1G	DC EP
Run 4	4	272	165	19-24	1.0	1G	DC EP
Run 5	4	376	165	19-24	0.8	1G	DC EP
Run 6	4	408	165	19-24	0.7	1G	DC EP
Run 7	4	344	165	19-24	0.9	1G	DC EP
Back gouging Run 1	3.2	348	123	19-25	0.7	1G	DC EP
Back gouging Run 2	4	360	165	21-23	0.8	1G	DC EP

PQR No E8018			
Base Metal			
Material 1	SA 516 gr 70	P-No. Group No	P1
Material 2	SA 516 gr 70	P-No. Group No	P1
Thickness / Type	16 mm Plate	PWHT	None
Filler metal			
Process	SMAW	Filler metal classification	
Process type	Manual	E8018-B2	AWS A5.5
Filler metal trade name 1	Afrox KV2		
Joint Preparation			
Pre-heat	75		
Prep Method	Thermal cutting, grinding		
Initial Clean	Flapper disk		
Interpass Clean	Wire Brush		
Joint Design		Pass Sequence	
			

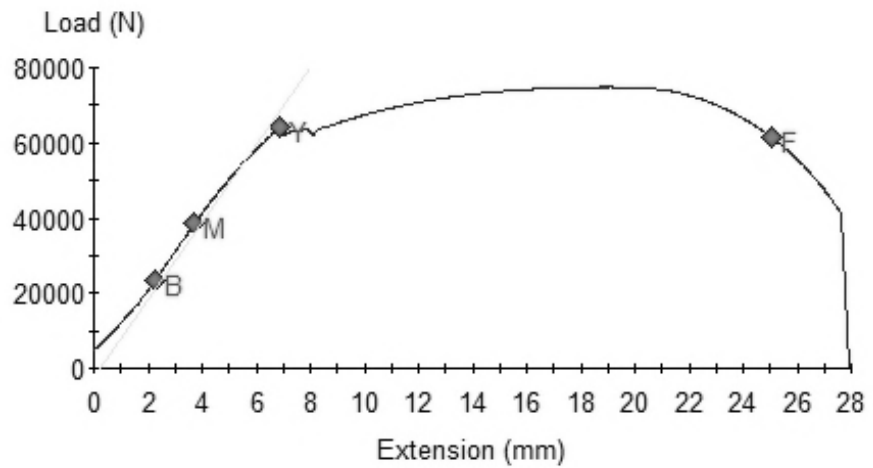
Electrical							
	Electrode size [mm]	Travel speed [mm/s]	Amps [I]	Volts [V]	HI [kJ/mm]	Weld Position	Polarity
Run 1	3.2	217	123	19-24	1.3	1G	DC EP
Run 2	4	216	160	21-27	1.5	1G	DC EP
Run 3	4	180	165	21-27	2.4	1G	DC EP
Run 4	4	227	165	21-27	1.0	1G	DC EP
Run 5	4	220	165	21-27	1.5	1G	DC EP
Run 6	4	167	165	21-27	1.8	1G	DC EP
Back gouging, Run 1	3.2	313	123	19-24	0.5	1G	DC EP
Back gouging, Run 2	4	220	165	21-27	1.5	1G	DC EP

PQR No E9018			
Base Metal			
Material 1	SA 516 gr 70	P-No. Group No	P1
Material 2	SA 516 gr 70	P-No. Group No	P1
Thickness / Type	16 mm Plate	PWHT	None
Filler metal			
Process	SMAW	Filler metal classification	
Process type	Manual	E9018-B3	AWS A5.5
Filler metal trade name 1	Afrox KV3		
Joint Preparation			
Pre-heat	75		
Prep Method	Thermal cutting, grinding		
Initial Clean	Flapper disk		
Interpass Clean	Wire Brush		
Joint Design		Pass Sequence	
			

Electrical							
	Electrode size [mm]	Travel speed [mm/s]	Amps[I]	Volts [V]	HI [kJ/mm]	Weld Position	Polarity
Run 1	3.15	164	123	19-24	164	1G	DC EP
Run 2	3.15	210	126	21-23.5	210	1G	DC EP
Run 3	4	300	165	21-23.6	300	1G	DC EP
Run 4	4	224	165	21-23.7	224	1G	DC EP
Run 5	4	420	165	21-23.8	420	1G	DC EP
Run 6	4	288	165	21-23.9	288	1G	DC EP
Run 7	4	448	165	21-23.10	448	1G	DC EP
Run 8	4	384	165	21-23.11	384	1G	DC EP
Run 9	4	370	165	21-23.12	370	1G	DC EP
Back gouging, Run 1	3.15	140	123	19-24	140	1G	DC EP
Back gouging, Run 2	4	300	165	21-25	300	1G	DC EP

Appendix B

E7018 All Weld Sample

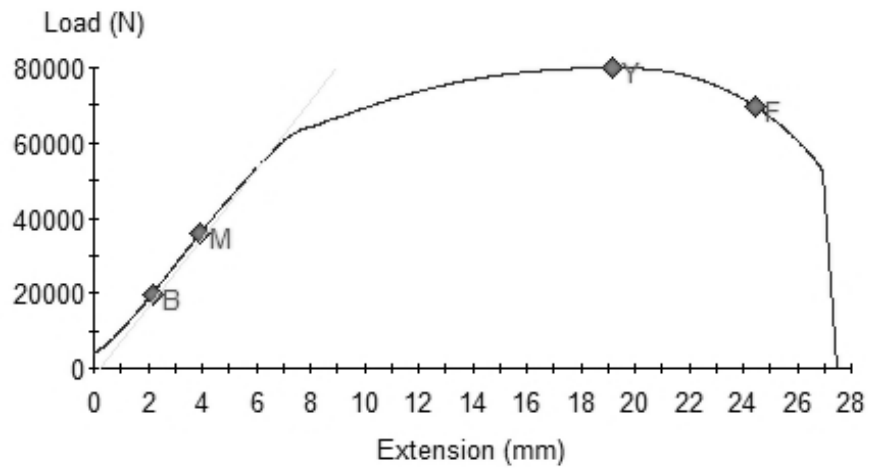


Specimen Results:

Specimen Number	Diameter mm	Peak Load kN	UTS MPa	Load At Yield kN	Stress At Yield MPa	Load At Offset Yield kN	Stress At Offset Yield MPa
1	12.740	74.8	587.1	64.1	503.205	54.5	427.2
Mean	12.740	74.8	587.1	64.1	503.205	54.5	427.2
Std. Dev.	****	****	****	****	****	****	****

Specimen Number	Break Load kN	Elongation At Break %
1	61.4	25.1
Mean	61.4	25.1
Std. Dev.	****	****

E8018 All Weld Sample

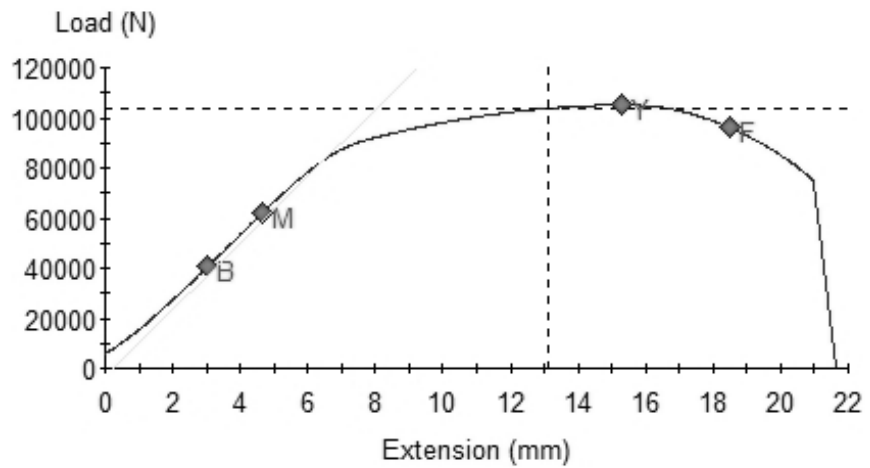


Specimen Results:

Specimen Number	Diameter mm	Peak Load kN	UTS MPa	Load At Yield kN	Stress At Yield MPa	Load At Offset Yield kN	Stress At Offset Yield MPa
1	12.770	80.0	624.5	80.0	624.515	55.4	432.3
Mean	12.770	80.0	624.5	80.0	624.515	55.4	432.3
Std. Dev.	****	****	****	****	****	****	****

Specimen Number	Break Load kN	Elongation At Break %
1	69.7	24.4
Mean	69.7	24.4
Std. Dev.	****	****

E9018 All Weld Sample

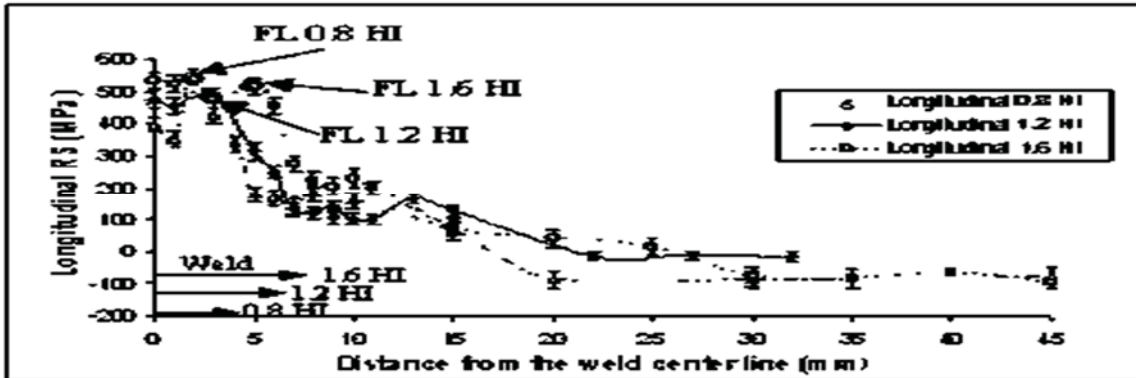


Specimen Results:

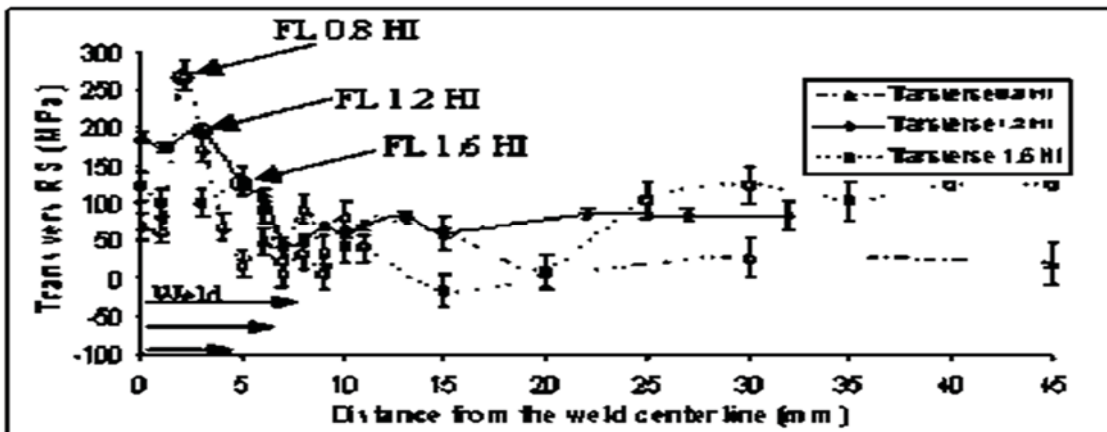
Specimen Number	Diameter mm	Peak Load kN	UTS MPa	Load At Yield kN	Stress At Yield MPa	Load At Offset Yield kN	Stress At Offset Yield MPa
1	12.700	105.1	829.6	105.1	829.650	83.6	659.9
Mean	12.700	105.1	829.6	105.1	829.650	83.6	659.9
Std. Dev.	****	****	****	****	****	****	****

Specimen Number	Break Load kN	Elongation At Break %
1	96.0	18.5
Mean	96.0	18.5
Std. Dev.	****	****

Appendix C



Influence of the HI on the longitudinal stress in a weld. The HI of 1.6 kJ/mm had the highest stress in the weld. The HI of 0.8 kJ/mm had the highest stress on the FL [19].



Transverse stress to the weld centreline for three separate HIs. As the HI increases, the stress decreases in the HAZ [19].